

STRUCTURAL EVOLUTION AND GROWTH MECHANISM OF HIERARCHIAL
HETEROSTRUCTURES COMPRISED OF CARBON NANOTUBES
DECORATED WITH NANOPARTICLES

by

WENWU SHI

NITIN CHOPRA, COMMITTEE CHAIR
RAMANA G. REDDY
MARTIN G. BAKKER

A THESIS

Submitted in partial fulfillment of the requirements
for the degree of Master of Science
in the Department of Metallurgical and Materials Engineering
in the Graduate School of
The University of Alabama

TUSCALOOSA, ALABAMA

2011

Copyright Wenwu Shi 2011

ALL RIGHTS RESERVED

ABSTRACT

Novel hybrid materials composed of hydrogels and heterostructured 1-D nanostructures such as carbon nanotubes (CNTs) coated with nanoparticles are critical for development of multi-functional analytical systems and biological applications. In this thesis, CNT-nickel/nickel oxide (Ni/NiO) core/shell nanoparticle (CNC) heterostructures were prepared in a simple and single step synthetic approach. The high surface-to-volume ratio and aspect ratio of chemical vapor deposition (CVD)-grown CNTs (average diameter $\sim 46 \pm 16.4$ nm) allowed to uniformly coat with Ni/NiO core/shell nanoparticles (average diameter $\sim 12 \pm 2$ nm). The crystal structure, morphology, and phases of CNC heterostructures were characterized using high-resolution transmission electron microscopy (TEM), scanning electron microscopy (SEM), Raman Spectroscopy, X-ray Photoelectron Spectroscopy (XPS) and X-ray diffraction (XRD). Single parameter controlled structural and morphological evolution of heterostructures was also evaluated. With the increase of reaction time, distribution density of nanoparticles on CNTs decreased and different shapes of nanoparticles also emerged. When reaction time was extended to 15 hrs due to the interaction between nickel and phosphine based stabilizers, phosphide nanoparticles on CNTs were synthesized.

Subsequently, as-produced CNC heterostructures were incorporated into poly vinyl alcohol (PVA) hydrogel. These CNC heterostructure-PVA hydrogels were rigorously characterized for their chemical functionality, morphology, and water absorbing capacity using spectroscopic (FTIR and UV-vis transmittance), SEM, and swelling/shrinking studies. CNC heterostructure-PVA hydrogel was utilized for separating and concentrating chemical species

from a mixture. The approach also demonstrated that these hybrid materials can also selectively concentrate L-histidine or histidine-tagged green fluorescent protein (GFP) in the solution. Finally, a cycled magnetic field was applied to control the releasing speed of molecules loaded in the PVA hydrogel. Such selective and multi-component hydrogels can be very useful for developing advanced chemical and biological sensors.

Thermal stability of prepared heterostructures was evaluated in a N₂-rich atmosphere. It was found that high temperature would result nanoparticles migration from CNTs to flat substrate. Meanwhile, decoration of nanoparticles effectively extended the stability range of CNTs from ~ 400 °C to temperatures greater than 600 °C.

DEDICATION

I dedicate this thesis to my family and friends.

LIST OF ABBREVIATIONS AND SYMBOLS

<i>CCD</i>	Charge Coupled Devices
<i>CVD</i>	Chemical Vapor Deposition
<i>CNTs</i>	Carbon Nanotubes
<i>CNC</i>	Carbon Nanotube-Nickel/Nickel Oxide Nanoparticles Heterostructures
<i>EDX</i>	Energy Dispersive X-ray Spectroscopy
<i>EWC</i>	Equilibrium Water Content
<i>HAADF</i>	High Angle Annular Dark Field
<i>KPS</i>	Potassium Persulfate
<i>MWCNTs</i>	Multi-Walled Carbon Nanotubes
<i>NIPAM</i>	N-isopropylacrylamide
<i>PBS</i>	Phosphate Buffered Saline
<i>PDADMAC</i>	Poly(diallyldimethylammonium)chloride
<i>PEG</i>	Polyethylene Glycol
<i>PVA</i>	Polyvinyl Alcohol

<i>SEED</i>	Substrate-Enhanced Electroless Deposition
<i>SEM</i>	Scanning Electron Microscopy
<i>SWCNTs</i>	Single-Walled Carbon Nanotube
<i>T</i>	Tesla
<i>TEM</i>	Transmission Electron Microscopy
<i>TEMED</i>	Tetramethylethylenediamine
<i>XPS</i>	X-ray Photoelectron Spectroscopy
<i>XRD</i>	X-ray Diffraction

ACKNOWLEDGMENTS

I would like to greatly thank my advisor, Dr. Nitin Chopra for his support and guidance, and thank Dr. Shweta Kapoor for proof reading of all my published manuscripts. I would also like to thank my group members who helped me at every step of my master's, with special thanks to Mr. Junchi Wu (Graduate Student), Ms. Kristy Crews (NSF-REU student), Mr. Anshuman Bansal (NSF-REH student), and Dr. Hylton G. McWhinney (NSF-HBCU visiting scientist from Prairie View A & M University). Thanks to the Central Analytical Facility (CAF) staff including Mr. Rich Martens, Mr. Johnny Goodwin, and Mr. Robert Holler for providing training and lessons. I would also like to thank staff from MTE department and MINT center including Ms. Jan Creitz, Mr. Bob Fanning, Ms. Lyndall Wilson, Ms. Kim Walker, Ms. Casey Mcdow, Ms. Jamie Crawford, and Mr. John Hawkins. I would also like to thank Dr Reddy and Dr Bakker for serving on my committee.

I would like to thank financial support from CAF in the University of Alabama, University of Alabama's Office of Sponsored Programs, Research Grant Committee Award, and NSF award (0925445) for my tuition, stipend, instrument time, supplies and infrastructure/resource.

Finally, I would like to thank my family and friends with all encouragement and support.

CONTENTS

ABSTRACT.....	ii
DEDICATION.....	iv
LIST OF ABBREVIATIONS AND SYMBOLS	v
ACKNOWLEDGMENTS	vii
LIST OF TABLES.....	xi
LIST OF FIGURES	xii
1. INTRODUCTION.....	1
1.1 Synthesis, Characterization, and Functionalization of Carbon Nanotubes	4
1.1.1 Synthesis of Carbon Nanotubes.....	4
1.1.2 Functionalization of Carbon Nanotubes.....	5
1.2 Synthesis and Applications of Carbon Nanotube-Nanoparticle Heterostructures	8
1.2.1 Chemical Linking of Carbon Nanotube and Nanoparticles.....	8
1.2.1.1 Covalent Linking of Carbon Nanotube and Nanoparticles	8
1.2.1.2 Non-Covalent Linking of Carbon Nanotubes and Nanoparticles.....	11
1.2.2 Direct Formation of Nanoparticles onto Carbon Nanotube Substrates	15
1.2.2.1 Spontaneous Formation of Nanoparticles on Carbon Nanotube Surface	15
1.2.2.2 Externally Stimulated Formation of Nanoparticles on Carbon Nanotubes	18
1.2.3 Applications of Carbon Nanotube-Nanoparticles Heterostructures	21
1.3 Encapsulation of Inorganic Nanomaterials into Hydrogel	23

1.3.1 Synthesis and Characterization of Hydrogel	23
1.3.2 Encapsulation of Inorganic Nanomaterials.....	26
1.3.3 Stimuli-Responsive Materials Based on Hydrogel and Nanomaterials.....	27
1.4 Motivation, Challenges, and Goals	29
1.4.1 Motivation and Challenges.....	29
1.4.2 Goals.....	30
2. EXPERIMENTAL PROCEDURES.....	33
2.1 Synthesis of Carbon Nanotubes	33
2.3 Synthesis of Composite Hydrogel Based on CNC Heterostructures	36
2.4 Absorption and Concentration Ability of Composite Hydrogel	38
2.5 Controlled Release of Dye Loaded Hydrogel	39
2.6 Thermal Stability of Carbon Nanotubes and CNC Heterostructures	40
2.7 Characterization	42
2.7.1 Scanning Electron Microscopy.....	42
2.7.2 Transmission Electron Microscopy	44
2.7.3 X-ray Diffraction	46
2.7.4 X-ray Photoelectron Spectroscopy	46
2.7.5 Raman Spectroscopic Characterization.....	49
2.7.6 UV-vis spectroscopy.....	51
2.7.7. Fourier Transform Infrared Spectroscopic Characterization.....	53
3. RESULTS AND DISCUSSION.....	54
3.1 Synthesis and Characterization of Carbon Nanotubes	54
3.2 Synthesis and Characterization of CNC Heterostructures	60

3.3 Structural Evolution of CNC Heterostructures Controlled by Single Parameter	75
3.4 Synthesis and Characterization of Composite Hydrogel.....	96
3.5 Absorption and Concentration Ability of Composite Hydrogel	101
3.6 Controlled Release with External Magnetic Field	105
3.7 Thermal Stability of CNC Heterostructures and Carbon Nanotubes	109
4. CONCLUSION AND FUTURE WORK	135
REFERENCES	138
APPENDIX.....	147

LIST OF TABLES

Table 1	Identification of XPS peaks	74
Table 2	Average diameter or size of Ni nanoparticles on the CNTs surface as a function of reaction duration.	81
Table 3	Lattice mismatch between the core Ni nanoparticle and the polycrystalline NiO shell as observed using TEM and XRD. Note: XRD shows all the crystal planes for the individual component.	89
Table 4	Binding energy (eV) chart derived from XPS study for as-produced CNTs, CNC heterostructures, and CNC heterostructures after annealing.	121
Table 5	Shell thickness and conversion percentage at different temperatures	128

LIST OF FIGURES

- Figure 1.1 (A) Proposed growth mechanisms of CNTs. (B) Digital picture of unsaturated CS₂ solution of s-SWCNTs and (C) Functionalization of CNTs with octadecylamine.7
- Figure 1.2 (A) Schematic representation of nanoparticles specifically attached CNTs through paired interaction. (B) Au nanoparticled decorated on CNTs through thiol group. Photographs of pristine SWCNTs (C) and of the dispersable SWCNTs-streptavidin-quantum dots supramolecular luminescent nanoassembly (D) in phosphate-buffered saline. (E) Schematic showing the interactions between CD3 receptors on the Jurkat T leukemia cell membrane and a SWCNTs-streptavidin-quantum dots nanoassembly.10
- Figure 1.3 (A) Illustration of noncovalent assembly of the CdS-SWCNTs hybrids with controllable nanoparticle density and dispersity. Characterization of the CdS-SWCNTs hybrids with controlled density and dispersity. TEM images of (B) the SWCNTs and (C, D) the CdSSWCNTs hybrids with 85.7 wt % CdS nanoparticle content. Inset in (D) corresponding SAED pattern. (E-G) TEM images of different composition hybrids containing 50, 83.3, and 90.9 wt% CdS nanoparticle content, respectively.13
- Figure 1.4 (A) Illustration of gold nanoparticles assembled on CNTs through 1-pyrenemethylamine interlinker. (B) High-density deposition of individual Au nanoparticles on CNTs. High-magnification TEM images of CNT-Au nanoparticlecomposites using (C) N-(1-naphthyl)ethylenediamine and (D) phenethylamine as interlinkers. (E) Schematic view of the process for anchoring gold nanoparticles to CN_x nanotubes.14
- Figure 1.5 (A) Schematic showing spontaneous deposition of nanoparticles on CNTs. (B) Diagram showing the Fermi energy of SWCNTs, and the reduction potentials of Au³⁺ and Pt²⁺ vs. SHE, respectively. (D) A schematic representation of Terpy coating on SWCNTs via a noncovalent interaction and the consequent formation of transition-metal nanoparticles. The sizes of the molecules are not to scale.17

Figure 1.6 (A) MWCNTs-Au. (B) Schematic of electrode. (C) AFM images. (D) MWCNTs-Ag through microwave. (E) MWCNTs-Ag from ball-milling. (F) MWCNTs-Ag formation from heating. (G) MWCNTs-Au.....	20
Figure 1.7 Schematic represents the formation and degradation (for dex-HEMA and dex-(lactate) -HEMA) of dextran hydrogels. Gels are formed by radical polymerization of the methacrylate groups using KPS and TEMED as initiator system. Degradation occurs by hydrolysis of the carbonate and lactate ester for dex-HEMA and dex-(lactate) -HEMA, respectively.	25
Figure 1.8 (A) Schematic showing (B) controlled releasing of drug from Au-nanocage NIPAM hydrogel. (C) Controlled release of drugs from Fe ₃ O ₄ -NIPAM hydrogel. (D) Schematic of the concept of remote controlled hydrogel nanocomposite valves with an alternating magnetic field. (E) pH triggered aggregation of Au nanoparticles.....	28
Figure 1.9 Schematic showing goals of this thesis.	32
Figure 2.1 Schematic (A) and temperature profile (B) of chemical vapor deposition furnace for CNTs growth.	34
Figure 2.2 Approach for the fabrication of CNC heterostructure-PVA hydrogel.	37
Figure 2.3 Experimental approach for the synthesis of CNC heterostructures (step 1), structural evolution of nanoparticles on CNTs surface (step 2), and thermal stability of CNC heterostructures (step 3) and as-produced CNTs (step 4). Note: 15 hrs of growth resulted in Ni ₁₂ P ₅ nanoparticles on the CNTs surface. The growth time indicates the duration for which the heterostructure synthesis was performed after the addition of TOPO and TOP into the reaction mixture and the temperature stabilized to ~ 250 °C.	41
Figure 2.4 (A) Schematic showing interaction between electron beam and sample. (B) image of JEOL 7000.....	43
Figure 2.5 Digital image of Tecnai F-20 Transmission Electron Microscopy.	45
Figure 2.6 (A) schematic showing Bragg's law. (B) Digital image of X-ray Diffractometer.	47
Figure 2.7 Schematic of X-ray photoelectron spectroscopy. (B) Digital picture of Kratos Axis 165.	48

Figure 2.8 (A) Schematic of Raman scattering. (B) Bruker Senterra Raman system.	50
Figure 2.9 Digital pictures of UV-vis spectrometer.....	52
Figure 3.1 (A) and (B) SEM images of CNTs, the arrow in (A) shows the alignment of as-produced CNTs. (C) Low resolution TEM image of CNTs. (D) and (E) High-resolution TEM images showing CNTs walls, inter-wall spacing of CNT, and negligible amount of amorphous carbon present on the CNTs surface (indicated by arrows in (E)). (F) Electron diffraction of as-produced CNTs. Note the CNTs core is ~ 6 nm in diameter.	56
Figure 3.2 HADDF image of as prepared CNTs and typical EDX spectra.	57
Figure 3.3 Diameter distribution of CNTs.....	58
Figure 3.4 Raman spectrum of as-prepared CNTs.....	59
Figure 3.5 (A) SEM image of CNC heterostructures after rigorous washing. (B) SEM image of CNC heterostructure after ultrasonication for 30 min. (C) EDX spectrum of as-prepared CNC heterostructures, (D) Percentages of different elements (silicon is from substrate).....	61
Figure 3.6 (A) Magnetic characteristics of the CNC heterostructures after drying, the growth duration for these heterostructures after addition of stabilizers (TOP and TOPO) was 15 min. (B) The as-produced CNTs are non-magnetic and do not show attraction towards a magnet.	62
Figure 3.7 (A) TEM image of CNC heterostructure (scale bar: 0.1 μm). (B) High-resolution TEM of CNTs showing the wall morphology and spacing between the walls (scale bar: 5 nm). (C) TEM image indicating attached Ni/NiO core/shell nanoparticles on CNTs (scale bar: 5 nm). White dotted line indicates the interface between the two. Note: There is certain extent of aggregation of nanoparticles on CNTs. (D) High-resolution TEM image of Ni/NiO core/shell nanoparticle showing the (111) interplanar spacing for core nickel nanoparticles (scale bar: 2 nm).....	64
Figure 3.8 Diameter distribution of nickel/nickel oxide core-shell nanoparticles.....	65
Figure 3.9 X-ray diffraction for CNC heterostructures indicates peaks corresponding to Ni, NiO, and CNTs present in these heterostructures.	66
Figure 3.10 Electron Diffraction of CNC heterostructures.....	67

Figure 3.11 Raman Spectrum of CNC heterostructures, a star in the inset picture indicates the place where spectrum was collected.....	69
Figure 3.12 SEM images of control sample made from acid-treated CNTs.....	71
Figure 3.13 XPS spectra subtracted by linear background and fitted with individual peaks as well as overlapped peaks (indicated in Fig.3.13B). (A) C 1s and (B) O 1s spectra for as-produced CNTs. (C) C 1s, (D) O 1s, (E) Ni 2p, (F) P 2p, and (G) N 1s spectra for CNC heterostructures.	73
Figure 3.14 SEM images showing CNC heterostructures after (A) 15 min, (B) 30 min, (C) and (D) 15 hrs of growth duration. The nanoparticle coating in (C) is not uniform and large-sized particles are formed that do not decorate CNTs.....	76
Figure 3.15 TEM images of CNC heterostructures synthesized for (A), (B) 15 min, (C), (D) 30 min, (E), (F) 2 hrs, (G), (H) 4 hrs, (I), (J) 6 hrs, and (K), (L) 10 hrs. Each pair of images and an inset correspond to low and high-resolution TEM images. The polycrystalline NiO shell is observed for the coated nanoparticles. Note: The high-resolution TEM images show the lattice spacing and corresponding planes of the coated nanoparticles. (M) Schematic indicating the morphological evolution of nanoparticles on the CNTs surface as a function of growth time.....	78
Figure 3.16 Detailed analysis of Ni/NiO core/shell nanoparticles formation on CNTs surface as a function of growth time. (A) Diameter distribution, (B) Spatial distribution (number of nanoparticles/ μm^2), (C) Inter-particle spacing, (D) 3-D plot showing morphological evolution as well as percentages of different shapes evolved, (E) Average nanoparticle projection area. Note: All the data analysis presented in this figure is for nanoparticles on the CNTs surface. More than 100 nanoparticles per sample were considered for nanoparticle area estimation and this includes all the shapes for the respective samples.....	80
Figure 3.17 (A) Plot of volume of nanoparticle to reaction time. (B) Linear fitting of volume of nanoparticles to reaction time at the first 6 hrs. (C), (D) (E), (F), and (G) Fitting of two stage Ostwald ripening at different exponent. (H) Plot of R^2 coefficient to different component.	86
Figure 3.18 High resolution TEM images of CNC heterostructures corresponding to the nanoparticle growth time of (A) and (B) 15 min, (C) 30 min, (D) 4 hrs, and (E) 6 hrs. The dotted lines indicate the bending of the graphene layers (or CNTs walls) between nanoparticles. (F) Lattice spacing of polycrystalline	

oxide shell. (G) Schematic showing bending of CNTs walls (radius of curvature is r) and increase in inter-wall spacing as a function of wall thickness between the adjacent nanoparticles.88

Figure 3.19 XRD of (a-f) CNC heterostructures showing the peaks of Ni ((JCPDS No.4-0850), NiO ((JCPDS No. 4-835) corresponding to the Ni/NiO core/shell nanoparticles, and (g) CNTs coated with $Ni_{12}P_5$ nanoparticles ((JCPDS No. 74-1381). Note: A low intensity peak (Δ or dotted line) is also observed around $\sim 26^\circ$ corresponding to c-axis spacing of graphene layers in CNTs. (*) indicates hcp Ni (JCPDS No. 45-1027) and the corresponding planes (left to right are (010), (002), (012), and (110))......91

Figure 3.20 Hollow and solid $Ni_{12}P_5$ nanoparticles formed on CNTs (Schematic in A) after 15 hrs. (B) and (C) High-resolution TEM images shows numerous nanoparticles that are hollow (indicated by arrows in C) and with different shapes. (D) High-resolution TEM image shows the lattice spacing and the corresponding plane. (E) TEM image shows large-sized irregular $Ni_{12}P_5$ particle observed for 15 hrs. These particles are isolated and do not form on the CNTs surface. (F) No bending of CNTs walls between adjacent nanoparticles is observed for these heterostructures. (G) Schematic shows proposed growth mechanism and formation of CNT-nickel phosphide nanoparticle heterostructures.94

Figure 3.21 (A) Size distribution of $Ni_{12}P_5$ nanoparticles on the CNTs surface. The average diameter of the nanoparticles was observed to be $\sim 11.1 \pm 1.8$ nm. The schematic in (A) shows the dimensions of nanoparticles that were hollow had a shell thickness of $\sim 2.85 \pm 0.42$ nm. Approximately $\sim 26.6\%$ of nanoparticles were hollow. (B) Shape distribution of $Ni_{12}P_5$ nanoparticles on the CNTs surface.95

Figure 3.22 (A) Digital image of PVA hydrogel (left, dotted rectangle) and CNC heterostructure-PVA hydrogel. Inset shows the transmittance spectrum in visible range for both hydrogels. (B) EWC graph of both PVA and PVA-CNT/Ni hydrogel. (C) SEM image of PVA hydrogel (scale bar: 1 μm). (D) SEM image of PVA-CNT/Ni hydrogel (scale bar: 1 μm) and inset shows high magnification of CNT/Ni inside hydrogel.99

Figure 3.23 (A) Full range ($500-4000\text{ cm}^{-1}$) FT-IR spectra of PVA hydrogel and CNC heterostructure-PVA hydrogel. (B) and (C) Magnified region of FTIR spectra showing different peaks for PVA hydrogel and CNC heterostructure-PVA hydrogel.100

Figure 3.24 Behavior of hydrogels in different chemical environments was indicated by concentration and amount of species in solution as a function of time. (A) Absorption of methyl orange in hydrogels. (B) and (C) Concentrating histidine-tagged GFP and L-histidine. (D) Selectively concentrating L-histidine from a mixture of methyl orange and L-histidine. (E), (F), (G) and (H) Changes of total amount plotted against time.	104
Figure 3.25 Actuation of composite hydrogel by magnet.....	107
Figure 3.26 Controlled releasing of molecules with (B) constant and (C) cycled magnetic field stimulation.....	108
Figure 3.27 SEM images of CNC heterostructures dispersed on silicon wafer after annealing for 1 hr at (A) 125 °C, (B) 200 °C, (C) 400 °C, (D) 600 °C, and (E) 750 °C. Note: The CNC heterostructures were synthesized for 30 min growth duration. Inset images are showing a detailed view of the annealed CNC heterostructures.	112
Figure 3.28 Schematic shows nanoparticle migration due to surface energy imbalance.	113
Figure 3.29 TEM images of CNC heterostructures after annealing for 1 hr at (A) 125 °C, (B) 200 °C (arrows indicate hollow nanoparticles), (C) 400 °C, (D) and (E) 600 °C, and (F) 750 °C. Note: CNC heterostructures were synthesized for 30 min reaction duration. These TEM images are taken for the samples observed in the SEM shown in Figure 3.26. The TEM samples were prepared by scratching the samples from the silicon wafer.	114
Figure 3.30 XPS spectra of CNTs and CNC heterostructures before and after annealing at different temperatures. Table 4 shows the precise peak locations for each constituent present. ‘CNT’ represents as-produced CNTs.....	119
Figure 3.31 XPS spectra of (a) C 1s, (b) Fe 2p, (c) O 1s, (d) Ni 2p for different annealing temperatures. The dotted lines in (d) for the spectra at 125 °C and 200 °C are shown as d1 and d2. Note: Spectra for as-prepared CNC heterostructures and those annealed at 125 °C are nearly overlapping. Thus, indicating minimal changes in chemical composition at low temperatures.	120
Figure 3.32 Phase change of Ni ⁰ (present in Ni/NiO core/shell nanoparticles) and Fe ⁰ (catalyst present in the CNTs inner core) observed as a function of annealing temperature for CNC heterostructures. (A) Conversion of Ni to Ni ²⁺ (NiO)	

and (B) conversion of Fe to Fe ^{x+} (various oxides of Fe such as FeO, Fe ₂ O ₃ , and Fe ₃ O ₄).	122
Figure 3.33 Raman spectra of CNC heterostructures showing D and G bands of CNTs after heat treatment at a) 400 °C, b) 600 °C, and c) 750 °C.....	123
Figure 3.34 (A) Volume of spherical cap. (B) Oxidation of Ni core into NiO shell, (C) Kinetic fitting of oxidation.	127
Figure 3.35 (A) Raman spectra of as-prepared CNTs and CNTs annealed at various temperatures (125 – 750 °C). (B) Breathing-like modes (BLMs) of MWCNTs up to 400 °C annealing temperature. (C) The I _G /I _D ratio for CNTs as a function of annealing temperature. (D)a-e The optical images of CNTs before and after annealing corresponding to the region considered for Raman spectra acquisition. Note: Since CNTs were dispersed on silicon wafer, two silicon peaks (518 cm ⁻¹ and 930 cm ⁻¹) were observed at higher annealing temperatures.	133
Figure 3.36 SEM and TEM (inset) images for the as-produced CNTs after annealing for 1 hr at (A) 125 °C, (B) 200 °C, (C) 400 °C, (D) 600 °C, and (F) 750 °C. The images demonstrate the various outcomes of the annealing process on the as-produced CNTs and show that these CNTs are damaged at as low as 125 °C.....	134

CHAPTER 1

INTRODUCTION

Over the past few decades, nanomaterials have been receiving significant attention due to their potential applications such as solutions for energy crisis, environment pollution as well as high efficiency, multifunctional, low energy cost, and portable devices.^{1,2,3} Nanomaterials have at least one dimension less than 100 nm and have been further categorized into 0-D (nanoparticles, quantum dots), 1-D nanomaterials (nanowires, nanobelt, and nanorod), and 2-D (thin films) depending on electron or charge carrier confinement. There are several reasons for the superior properties of nanomaterials compared with their bulk counterpart.¹ First of all, surface areas of nanomaterials are much larger than bulk materials.¹ Utilization of this aspect was widely shown in heterogeneous catalytic reactions where nanoparticles with fine size distribution were dispersed on mesoporous silica² and CNTs. This strategy has been proved with much better catalytic activities due to large reacting area as well as unexpected higher activity caused by change of electron affinity and ionization potential.¹ Secondly, properties of nanomaterials could be rationally altered due to the quantum mechanics effects associated with size.¹ It has been proven that band gap of semiconductor, wavelength of noble nanoparticles plasmonic excitation, and magnetic moment of elemental clusters are highly dependent on dimensions and morphologies of nanoparticles.¹ Thirdly, absence of defects inside nanomaterials could result in materials with theoretical mechanical strength, conductivity or other properties.³ Nanowires, nanosheets and nanotubes with great mechanical properties are widely used inside polymer matrix to enhance mechanical strength.³ Finally, these small objects could be directly

integrated into miniaturized electronic devices to form higher density storage media based on nanoparticles,⁴ logic gates build on nanowires,⁵ and optical modulator comprised of graphene.⁶

Unique properties and applications of single-component nanostructures^{7,8} are propelling the development of multi-component and hybrid nanostructures.^{9,10,11} The major advantages of such multi-component nanostructures (referred to as ‘heterostructures’) are their multi-functionality, structural stability, and purity of individual component comprising the heterostructure. Heterostructures having a one-dimensional (1-D) nanostructure component, such as nanotubes or nanowires, are termed as 1-D nanoscale heterostructures. Controlled synthesis and processing methods for these heterostructures are of particular interest and can give an opportunity to modulate their physico-chemical characteristics and properties. Such heterostructures can be categorized into two kinds: a) nanowire-based heterostructures (e.g., nanowire connected/decorated with nanoparticles, nanotubes, or nanowires) and b) nanotube-based heterostructures (e.g., nanotube connected/decorated with nanoparticles, nanotubes, or nanowires).¹² Among these, CNT-nanoparticle heterostructures are paid with great attention and are promising for energy technologies, catalysis, and chemical/biological sensors.^{13,14,15} There are several reasons accounting for the superiority of CNT-nanoparticle heterostructures. Firstly, CNTs are of great electron transportation ability and mechanical strength, which could effectively work as robust building blocks inside devices.⁸ Secondly, nanoparticles exhibit strong size dependant electrical, magnetic, and optical properties.¹ Anchoring of nanoparticles onto highly curved CNTs with large surface area or other substrates could successfully avoid the undesirable and detrimental aggregation of nanoparticles.² Thirdly, sharp interfaces/junctions between CNTs and nanoparticles will undoubtedly introduce either novel functionality or enhanced properties due to the strong interaction at nanometer scale.⁹ Various methods

developed to synthesize heterostructures.¹⁶ Chemical synthetic approaches, which commonly involve functionalizing CNTs and then linking them with nanoparticles or quantum dots, predominated.^{16,17,18} However, attachment of nanoparticles on CNTs without any use of covalent chemistry will lead to high purity heterostructure, which is desirable for numerous applications especially in biological field.

1.1 Synthesis, Characterization, and Functionalization of Carbon Nanotubes

Since their first discovery by Iijima *et al.* in 1991¹⁹, there is remarkable attention paid to CNTs because of their unique mechanical, electrical, optical, chemical characteristics.⁸ Applications in clean energy (solar cell,²⁰ hydrogen storage,²¹ and supercapacitor²²), micro- and nano-electromechanical system,²³ fast-response-low-detecting-limit sensor²⁴ have been developed. CNTs can be metallic or semiconducting depending on numbers of walls and their rolling vectors.⁸

1.1.1 Synthesis of Carbon Nanotubes

Various techniques such as arc-charge, laser-ablation, and chemical vapor deposition (CVD) were explored for synthesis of CNTs.⁸ CVD in the presence of transition metal catalysts (Ni, Co, Fe nanoparticles) has many merits compared with other methods.^{8,25} Usually, CVD technique progresses at relatively low temperature and does not require high voltage like arc-charge method. Moreover, for high voltage arc-charge method, a big problem is the existence of large amount of impurities (graphite, amorphous carbon).⁸ Although CVD process still brings transition metal nanoparticles as catalysts, which become impurities in CNTs. Considering their amount and consequent easy removal by post treatment, impurities of CNTs by CVD is negligible and acceptable. Another advantage, which is of great significance for future applications of CNTs, is its ability to fabricate well-aligned CNTs^{11,25} and site-selective CNTs.²³ These benefits are crucial for developing, fabricating, and assembling nanoscale architectures and devices using CNTs as blocks.^{23,26}

Even though the growth mechanism of CNTs is still a subject of controversy,⁸ and none of proposed mechanism can completely explain all CNTs formation. One of mechanisms, which

is widely used and recognized, is as following. Carbon atoms from cracking of organic carbon sources (aromatic hydrocarbon, alkenes, and alkynes)^{8,11,25} dissolve into pre-coated metal nanoparticles or in-situ synthesized nanoparticles during CVD process to form metal-carbon alloy. Extra carbon supplied by carbon source form CNTs. This mechanism can be divided into two sub-types: extrusion/root growth and tip growth depending on where nanoparticles are inside CNTs (Figure 1.1A).

One of the important parameters for CNTs growth in CVD process is metal nanoparticles catalyst.^{8,25} Metal-based nanoparticles not only assist the crack of hydrocarbon source but also facilitate the nucleation and growth of CNTs.^{8,25} Diameter, morphology, composition, and size distribution of nanoparticles can have great effects on the inner, outer diameters, length, and yield of CNTs.^{25,26} Although several special cases in which Au,²⁷ Cu,²⁸ and other nanoparticles served as catalysts or metal-catalyst-free techniques have been reported,^{29,30} transition metal (Fe, Co and Ni) currently predominated as CNTs catalysts.²⁵ Generally, catalyst is independently synthesized and then uniformly dispersed onto substrate or in-situ synthesized by decomposition of metal-organics. A good example of latter approach is the decomposition of ferrocene ($\text{Fe}(\text{C}_5\text{H}_5)_2$) into Fe nanoparticles.^{25,26}

1.1.2 Functionalization of Carbon Nanotubes

Beside the synthesis and characterization, chemical modification and functionalization of CNTs also possess great importance for tailoring of the solubility and surface functionality.^{31,32} This will require a detailed and through understanding of CNTs chemistry. In general, there could be two different approaches, which include direct binding of molecules onto graphitic surfaces or linking through carboxyl group formed on the surface of CNTs. A good example for

the first approach will be CNTs solubilization via π -stacking, which enables the introduction of various neutral and ionic functional groups onto CNTs surfaces.³¹ The second approach exploits rich carboxyl group chemistry, by which different molecules/functional groups on CNTs could be established through covalent bonding.³² Figure 1B demonstrated that solubility of CNTs in solvents increased by surface modification and figure 1C showed the steps for functionalization.

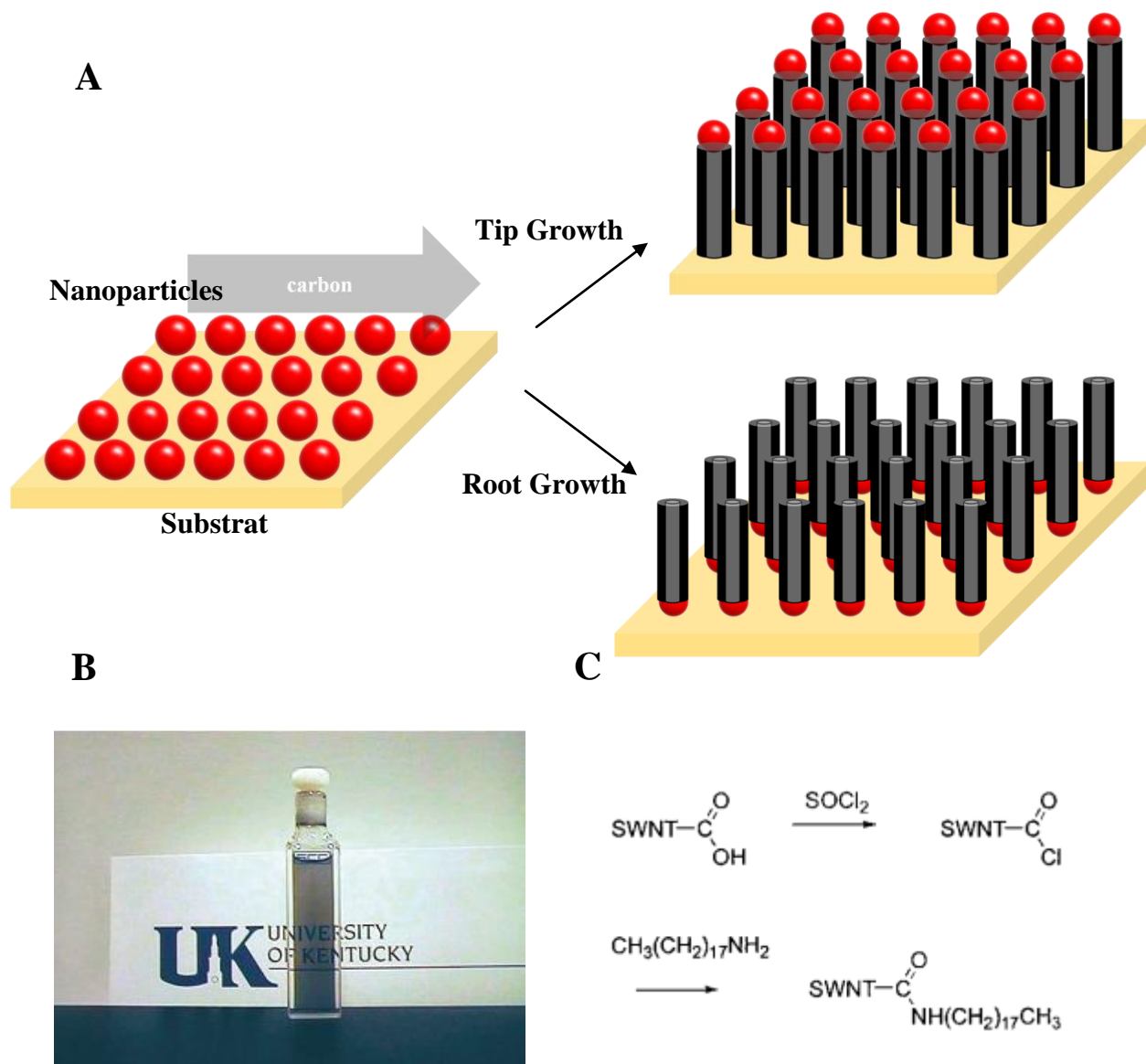


Figure 1.1 (A) Proposed growth mechanisms of CNTs. (B) Digital picture of unsaturated CS_2 solution of s-SWCNTs and (C) Functionalization of CNTs with octadecylamine (From 32, Reprinted with permission from AAAS).

1.2 Synthesis and Applications of Carbon Nanotube-Nanoparticle Heterostructures

Owing to excellent properties of CNT-nanoparticle heterostructures, various research efforts have been conducted to rationally tailor types of nanoparticles, distribution density, uniformity, size, and morphologies of nanoparticles onto CNTs.^{11,16,17} Two distinctive means could be utilized: (1) linking of separately formed CNTs and nanoparticles, (2) direct formation of nanoparticles onto CNTs substrates.

1.2.1 Chemical Linking of Carbon Nanotube and Nanoparticles

CNTs and nanoparticles were synthesized separately and then chemical/physical forces were utilized to link them together. This method usually involves in depth understanding of CNTs and nanoparticles surface chemistry and functionality.¹⁶ Since nanoparticles and nanotubes were formed before decoration, size and morphologies of nanoparticles could be easily tuned beforehand, while distribution density will be directly controlled by surface functional group density. However, the drawback for this will be the tedious, complex, and inefficient CNTs and nanoparticle surface modification. Depending on types of linking forces, this method could be further classified into covalent and non-covalent approaches.

1.2.1.1 Covalent Linking of Carbon Nanotube and Nanoparticles

Covalent linking of CNTs and nanoparticles (Figure 1.2A) is commonly based on the well-defined paired interactions of chemical functional groups or bio-molecules, such as Au nanoparticles-thiol group (Figure 1.2B),¹¹ biotin-streptavidin (Figure 1.2C, D, E),^{33,34} histidine-nickel nanoparticles,¹⁰ DNA hybridization³⁵ (Figure 1.2F), and EDC chemistry.¹¹ Through modification of each component with desired functional groups/molecules, subsequent mixing of both will result into precisely controlled heterostructures. In addition, depending on the size of

linking agents and nanoparticles, distribution density of nanoparticles could also be tailored. Another merit is the specific recognition affinity between CNTs and nanoparticles, which could facilitates site-seletive nanoparticles linking, or even multiple nanoparticles linking in a controllable manner.

The covalent method has been widely exploited and showed with great reliability and reproducibility. Smorodin *et al.* showd the linking of several biotin-conjugated CNTs onto strepdavidine loaded Au nanoparticles.³⁴ This method was also used to facilitate internalization of nanotubes into Jurkat T leukemia cells by multivalent CD3 receptor-mediated endocytosis as demonstrated in Figure 1.2E. Before nanoparticle loading, CNTs tend to settle down in phosphate-buffered saline (PBS) buffer because of the hydrophobic nature. However, a clear solution formed after loading CNTs with strepdavidin-quantum dots conjugated as showed in Figure 1.2D. Based on knowledge of interactions between metal nanoparticles and functional groups, loading of nickel nanoparticles and gold nanoparticle through histidine tags¹⁰ and thiol groups¹¹ were also performed. It is well known that DNA hybridization is also highly specific and selective,³⁵ this has also been used to connect CNTs with naoparticles.

With all above mentioned merits, drawbacks of this method should also be considered. In order to modify the surface of CNTs, strong acid treatment (HNO_3 and H_2SO_4) must be conducted, which generates defects inside and disrupts integrity of CNTs. Even when directly linking between graphite carbon atoms was used, covalent functionlization of CNTs unavoidably converts sp^2 hybridization into sp^3 hybridization, which could adversely affects the properties of CNTs due to the presence of defective sites.¹⁶

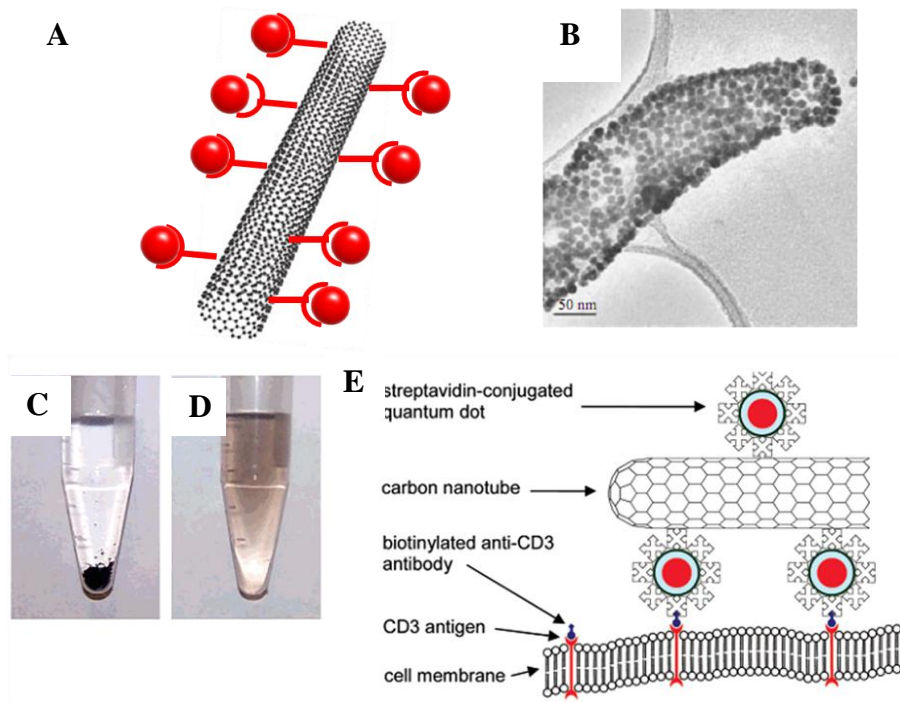


Figure 1.2 (A) Schematic representation of nanoparticles specifically attached CNTs through paired interaction. (B) Au nanoparticled decorated on CNTs through thiol group (Reprinted with permission from N. Chopra, M. Majumder, B. J. Hinds. *Advancedv. Functional. Material*, 15,(5), 2005, 858. Copyright 2005, John Wiley and Sons). Photographs of pristine SWCNTs (C) and of the dispersible SWCNTs-streptavidin-quantum dots supramolecular luminescent nanoassembly (D) in phosphate-buffered saline. (E) Schematic showing the interactions between CD3 receptors on the Jurkat T leukemia cell membrane and a SWCNTs-streptavidin-quantum dots nanoassembly (Reprinted with permission from Massimo Bottini, Fabio Cerignoli, Marcia I. Dawson, Andrea Magrini, Nicola Rosato, Tomas Mustelin. *Biomacromolecules* 2006, 7, 2259-2263, Copyright 2006, American Chemical Society).

1.2.1.2 Non-Covalent Linking of Carbon Nanotubes and Nanoparticles

Besides covalent linking, non-covalent linking based on hydrophobic interaction,²⁴ π - π stacking,³⁶ and electrostatic attraction³⁷ was also widely utilized to form CNT-nanoparticle heterostructures. Unlike specific recognition in covalent linking, interactions between CNTs and nanoparticles are generally non-specific. Thus, selective binding between CNTs and nanoparticles is difficult. However, this does not require acid treatment of CNTs and minimizes defects density in CNTs. Heterostructures formed in this method have good uniformity. Figure 1.3A showed an example where oleylamine was utilized to link CdS nanoparticles on CNTs. Due to the great affinity between CNTs and oleylamine, oleylamine could effectively adsorb onto CNTs to generate sites for anchoring of CdS nanoparticles. Figure 1.3D-G showed how decoration density of nanoparticles could be tuned by changing the weight ratio between CNTs and nanoparticles. Another interesting point is the reversible attachment and detachment of CdS nanoparticles on CNTs upon adding and removing of amine. This phenomenon could present as a chemical sensor for amine with proper I/V testing.²⁴ Another important mechanism is to link sp^2 hybridized CNTs with other molecules through π - π stacking. Huang *et al.* used this technique to assemble Au nanoparticles onto CNTs.³⁶ Au nanoparticles were modified with 1-pyrenemethylamine through the lone pair of electrons on the nitrogen atom. While the subsequent π - π stacking between CNTs and 1-pyrenemethylamine could result CNTs-Au nanoparticles structures.³⁶ It is plausible that molecules containing mono- and polycyclic aromatic structures and alkylamine groups can also link nanoparticles onto CNTs.³⁶ Similar heterostructures were synthesized based on N-(1-naphthyl)ethylenediamine and phenethylamine.³⁶ By tuning surface charge of CNTs and nanoparticles, electrostatic force could be utilized to synthesize CNT-nanoparticle heterostructures. Jiang *et al.* did acid treatment for

nitrogen-doped CNTs to form carboxyl groups on surface, then grafted poly(diallyldimethylammonium)chloride (PDADMAC) onto CNTs by electrostatic attraction between carboxyl groups and polyelectrolyte. The modified CNTs were mixed with Au nanoparticle solution while negatively charged gold nanoparticles anchored to the nanotubes surface through the electrostatic interaction between polyelectrolyte and nanoparticles³⁷. The detailed steps were presented in Figure 1.4E.

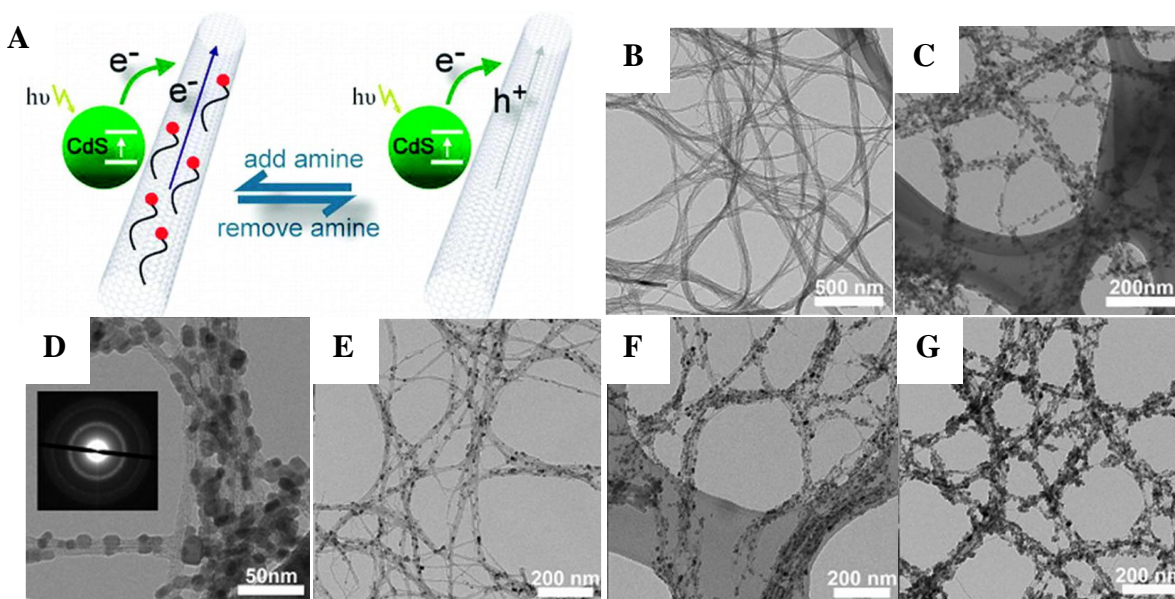


Figure 1.3 (A) Illustration of noncovalent assembly of the CdS-SWCNTs hybrids with controllable nanoparticle density and dispersity. Characterization of the CdS-SWCNTs hybrids with controlled density and dispersity. TEM images of (B) the SWCNTs and (C, D) the CdS-SWCNTs hybrids with 85.7 wt % CdS nanoparticle content. Inset in (D) corresponding SAED pattern. (E-G) TEM images of different composition hybrids containing 50, 83.3, and 90.9 wt% CdS nanoparticle content, respectively (Reprinted with permission from Xianglong Li, Yi Jia, Anyuan Cao. *ACS Nano*, 2009, 1(4), 506-512, Copyright 2009, American Chemical Society).

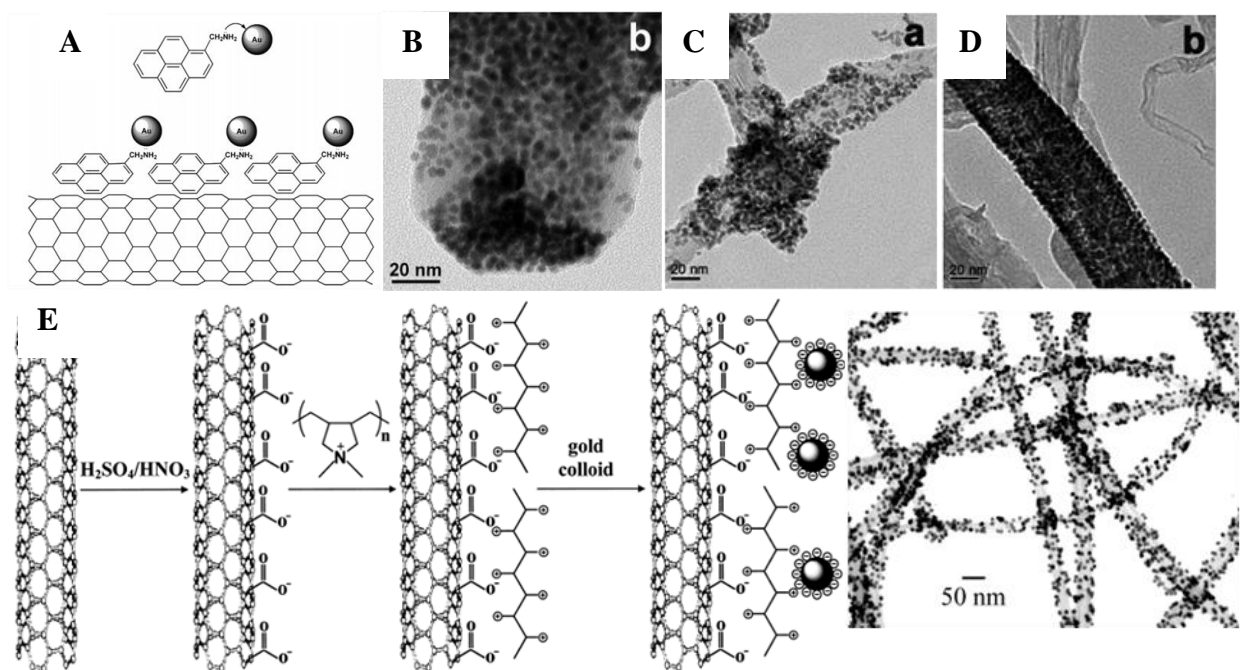


Figure 1.4 (A) Illustration of gold nanoparticles assembled on CNTs through 1-pyrenemethylamine interlinker. (B) High-density deposition of individual Au nanoparticles on CNTs. High-magnification TEM images of CNT-Au nanoparticlecomposites using (C) N-(1-naphthyl)ethylenediamine and (D) phenethylamine as interlinkers (Reprinted with permission from Yue-Yu Ou, Michael H. Huang. *Journal of Physical Chemistry B*. 2006, 110, 2031-2036. Copyright 2006, American Chemical Society). (E) Schematic view of the process for anchoring gold nanoparticles to CN_x nanotubes (Reprinted with permission from Kuiyang Jiang, Ami Eitan, Linda S. Schadler, Puickel M. Ajayan, Richard W. Siegel. *Nano Letters*, 2003, 3(3), 275-277 Copyright 2003, American Chemical Society).

1.2.2 Direct Formation of Nanoparticles onto Carbon Nanotube Substrates

Another strategy for the formation of heterostructure is to nucleate nanoparticles directly on CNTs avoiding linking agents. In this case, CNTs are indispensably involved in the formation of the nanoparticles. Compared with linking method, this ensures fully covering of nanoparticles and effectively eliminates unbound and isolated nanoparticles in the system. The mechanism of formation could be diverse from case to case. Nevertheless, depending on how nanoparticles are formed on CNTs, it could be divided into spontaneous and externally stimulated formation.

1.2.2.1 Spontaneous Formation of Nanoparticles on Carbon Nanotube Surface

It was observed that noble metal nanoparticles could spontaneously form on the surface of semiconductor or metal when reduction potential conditions were matched.³⁸ Dai *et al.* first reported the formation of Au and Pt nanoparticles on the sidewall of single walled carbon nanotubes (SWCNTs) based on direct redox reaction.³⁸ The major motive is the Fermi level of SWCNTs (~ 5 eV) is higher than reduction potentials of AuCl_4^- and PtCl_4^- ions, which enables spontaneous electron transfer from nanotubes to metal ions.³⁸ As seen from the potential diagram, only when reduction potentials of ions are well below the Fermi level of CNTs, spontaneous reduction on CNTs is possible. Later Qu *et al.* proposed “Substrate-Enhanced Electroless Deposition” (SEED) process,³⁹ by which species of nanoparticles could be further extended to Cu, Ag, and other metals. In this case, outstanding electron conductivity of CNTs was well utilized. A local galvanic cell was formed where CNTs worked as a cathode and the substrate served as an anode. Nanoparticles were then formed by the consumption and dissolution of metal substrates.³⁹ Besides on the pristine CNTs, CNTs conjugated with other organic molecules were also utilized for the direct formation of transitional metal nanoparticles. Terpy-modified CNTs

through interaction between nonbonding electrons of the three nitrogen atoms in Terpy and the π -electrons in CNTs were used as substrate for Ru, Cu, Zn, and Sn nanoparticles.⁴⁰ The main driving force is the electron transfer between Terpy-CNTs and metal ions.⁴⁰

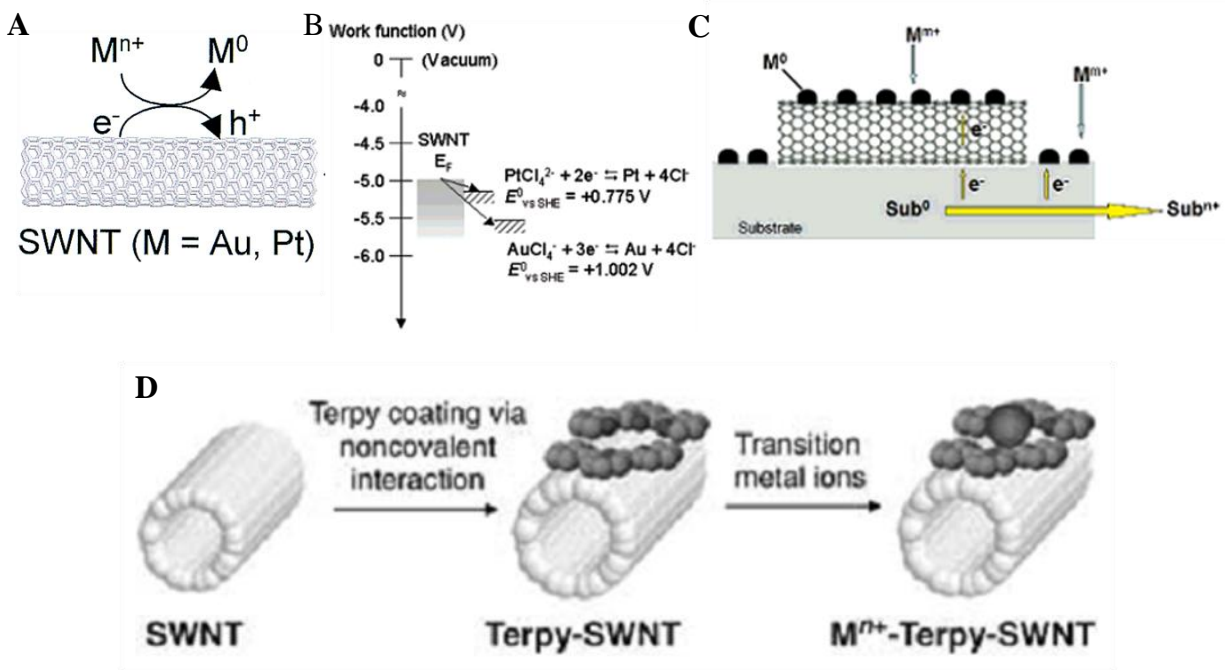


Figure 1.5 (A) Schematic showing spontaneous deposition of nanoparticles on CNTs. (B) Diagram showing the Fermi energy of SWCNTs, and the reduction potentials of Au^{3+} and Pt^{2+} vs. SHE, respectively (Reprinted with permission from Hee Cheul Choi, Moonsub Shim, Sarunya Bangsaruntip, Hongjie Dai, Journal of American Chemical Society 2002, 124, 9058-9059, Copyright 2002, American Chemical Society). (C) Schematic illustration of metal nanoparticles deposition on CNTs via the SEED process (Reprinted with permission from Liangti Qu, Liming Dai, Journal of American Chemical Society, 2005, 127, 10806-10807, Copyright 2005, American Chemical Society). (D) A schematic representation of Terpy coating on SWCNTs via a noncovalent interaction and the consequent formation of transition-metal nanoparticles. The sizes of the molecules are not to scale (Reprinted with permission from Yoonmi Lee, Hyun Jae Song, Hyeon Suk Shin, Hyun Joon Shin, Hee Cheul Choi, Small, 2005, 1(10), 975-979, Copyright 2005, John Wiley and Sons).

1.2.2.2 Externally Stimulated Formation of Nanoparticles on Carbon Nanotubes

Besides the spontaneous formation, other methods involved driving forces such as reducing agent,⁴¹ electric current,¹⁷ microwave,⁴² thermal treatment,⁴³ ball milling,⁴⁴ and UV light⁴⁵ were also performed. In this case, CNTs mainly worked as highly curved substrates, which offer sites for nucleation. In order to form site-specific deposition, modification of CNTs that provides preferred absorption of ions or nanoparticles was carried out constantly.⁴⁴

Figure 1.6A demonstrates the formation of Au nanoparticles on CNTs by reduction of AuCl_4^- with sodium citrate.⁴¹ The size of Au nanoparticles could be tuned by the amount of sodium citrate. The major merit is formation of nanoparticles requires no tedious surface functionalization and modification. Nevertheless, due to limited solubility of CNTs inside water, acid treatment is necessary and low concentrated CNTs (1mg/100 mL) was used. Thus, only small fraction of sample could be formed in this case.

Electrodeposition was also utilized for the deposition of nanoparticles on CNTs as demonstrated by Quinn *et al.*¹⁷ Electrode was produced by patterned CNTs growth following standard microfabrication techniques. Electrolyte solution was dropped onto surface of electrode and metal electrodeposition was performed potentiostatically. Size and distribution density of nanoparticles could be tuned by potential, deposition time, and metal salt concentration.¹⁷ However, drawback of this method is obvious. Because of complex procedures for electrode preparation, this process could be costly and inefficient.

Yin and Connel *et al.* applied microwave irradiation,⁴² thermal treatment,⁴³ and ball milling⁴⁴ to form CNT-nanoparticle heterostructures. The primary motive is based on the in-situ decomposition of acetate upon to microwave, thermal, and mechanic energy. Large quantity,

pristine samples could be prepared in this solventless method without organic surfactants. The loading density and size could be manipulated by ratio between CNTs and acetates, as well as degree of external energy. However, the robustness of this set of heterostructures could be an issue due to weak binding.

It is well known that some metal salts will decompose with the illumination of UV light. In this regard, CNTs-nanoparticle heterostructures could be formed by photoreduction.⁴⁵ In order for the site specific reduction, surface modification of nanoparticles could be performed as demonstrated in Figure 1.6G. AuCl_4^- ions were selectively absorbed on the surface of acid-treated CNTs. Light illumination caused deposition of Au nanoparticles.

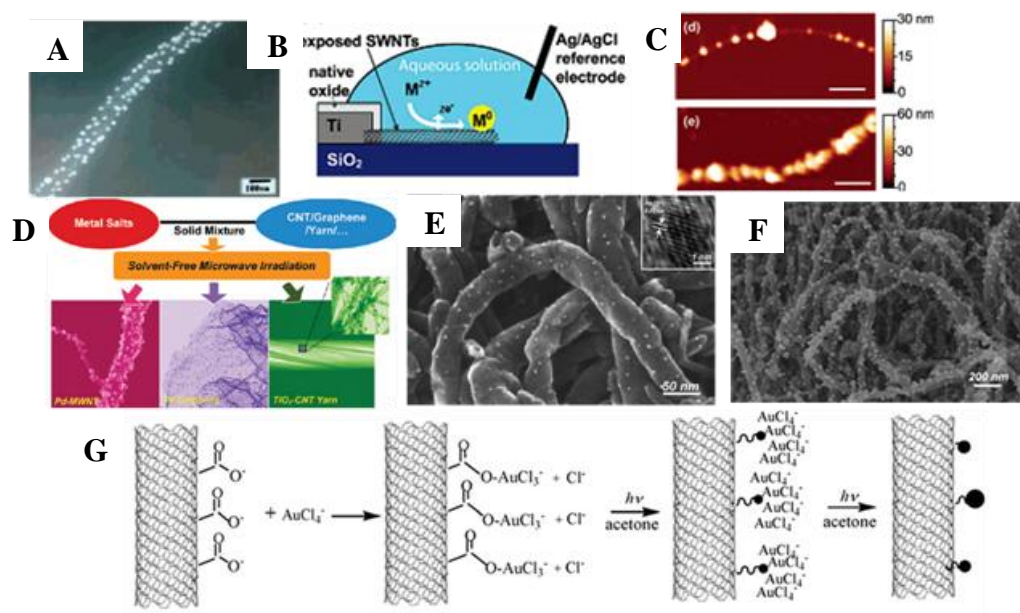


Figure 1.6 (A) MWCNTs-Au (Reprinted with permission from Renyun Zhang, Xuemei Wang, *Chemistry of Materials*, 2007, 19, 976-978. Copyright 2007, American Chemical Society). (B) Schematic of electrode. (C) AFM images (Reprinted with permission from Bernadette M. Quinn, Cees Dekker, Serge G. Lemay, *Journal of American Chemical Society*, 2005, 127, 6146-6147. Copyright 2005, American Chemical Society). (D) MWCNTs-Ag through microwave (Reprinted with permission from Yi Lin, David W. Baggett, Jae-Woo Kim, *et al.* *ACS Applied Materials and Interface*. 2011, 3, 1652–1664. Copyright 2011, American Chemical Society). (E) MWCNTs-Ag from ball-milling (Reprinted with permission from Yi Lin, Kent A. Watson, Sayata Ghose, *et al.* *Journal of Physical Chemistry C*. 2009, 33(113), 14858-14862. Copyright 2009, American Chemical Society). (F) MWCNTs-Ag formation from heating (Reprinted with permission from Yi Lin, Kent A. Watson, Michael J. Fallbach, *et al.* *ACS Nano*, 2009, 3(4), 871-884. Copyright 2009, American Chemical Society). (G) MWCNTs-Au (Reprinted from *Colloids and Surfaces A: Physicochemical and Engineering Aspects*, 312, Zhang *et al.*, The growth of uncoated gold nanoparticles on multiwalled carbon nanotubes, 136, Copyright (2008), with permission from Elsevier).

1.2.3 Applications of Carbon Nanotube-Nanoparticles Heterostructures

CNT-nanoparticle heterostructures can exhibit unique advantages from both sides. Numerous applications for catalysts, chemical and biological sensors, solar energy harvesting, and electric supercapacitor have been reported.

For catalytic reaction where activity is proportional to exposed active sites, CNT-nanoparticle heterostructure could of great importance. In the best scenario, highly active nanoparticles are uniformly loaded on robust and conductive CNTs without aggregation. It has been found that CNT-Pd nanocube heterostructures exhibited higher electrocatalytic activity toward reduction of O₂ from 0.5 M H₂SO₄ compared with commercial Pt/C catalyst due to better electric conductivity and higher electroactive surface area.⁴⁶ Recent work also demonstrated that hairy CNT-Pd heterostructures exhibited an efficient catalytic effect in the C–C Suzuki coupling reaction and were regenerated up to four times without loss of catalytic activity.⁴⁷ Thus, utilization of CNTs-nanoparticles heterostructures in heterogeneous catalytic reaction, organic synthesis, and fuel cell could be highly advantageous.

CNT-nanoparticle heterostructures have been used as chemical and biological sensors working at low detection level and fast response time. There are several reasons accounting for their better performance. Firstly, highly dispersed nanoparticles worked as receptors for targeted molecules. Secondly, highly conductive CNTs could allow for fast electron transfer from absorbed molecules on the surface of heterostructures and CNTs. Thirdly, simple manipulation and modification of surface functionality for both CNTs and nanoparticles could contribute to the selectivity of chemical sensing. Lastly, heterostructures in 1-D morphologies could be

integrated as field effect transistor where potential vibration from interaction between targeted molecules and heterostructures could work as gate.^{9,12,13,16}

1.3 Encapsulation of Inorganic Nanomaterials into Hydrogel

Hydrogel is another kind of important material, which consists of large amount of water inside hydrophilic, chemically or physically cross-linked, long chain molecules networks.^{48,49} Due to the large amount of water, hydrogels show superior flexibility and possess volumetric swelling/shrinking, or transparency/opaque transitions upon stimulation (temperature, water, pH, and ion strength) by absorbing or releasing water.^{48,49} Hydrogels show great potential in tissue engineering, drug delivery, contact lens, and smart materials.⁴⁹ By incorporating inorganic functional nanomaterials into hydrogels, a nanocomposite gel could be synthesized which couples benefits of both hydrogels and nanomaterials, while at the same time preserving the biocompatibility of the entire system.⁴⁸ Such inorganic/organic networks show superior mechanical, optical, and electric properties.^{3,48} It has also been reported that smart nanocomposite gel could perform different functions upon stimulation such as magnetic field, temperature, and pressure.

1.3.1 Synthesis and Characterization of Hydrogel

In order to organize long chain monomers into 3-D network structures, physical or chemical crosslink methods were commonly utilized. As for chemical methods, radical polymerization, high energy induced polymerization, chemical reaction between complementary groups were extensively utilized.⁴⁹ Figure 1.7 shows formation of chemically formed dextran hydrogel by radical polymerization of the methacrylate groups using potassium persulfate (KPS) and tetramethylethylenediamine (TEMED) as initiators. The as-prepared dextran hydrogel could also be degraded by hydrolysis of the carbonate and lactate ester for dex-HEMA and dex-(lactate)₂-HEMA, respectively. Chemical methods usually involve crosslinking agents, which

could affect the integrity of the hydrogel and are frequently hazardous for the consequent biomedical applications. Thus, cleaning steps must be performed to remove crosslinking agents afterwards. Another route for synthesis of hydrogel involves physical methods such as the freeze-thaw process, where chains were crosslinked through ionic interactions or from copolymers linking.

Equilibrium water content (EWC) is frequently used to characterize hydrogels. In this regard, percentage of water inside the entire hydrogel was recorded against external stimulus, such as duration inside water, pH, and temperature. EWC directly showed how external conditions could influence the absorbing and releasing of water from hydrogel.

$$\text{Equilibrium Water Content (EWC)} = 100\% \times \frac{W_{\text{swollen hydrogel}} - W_{\text{shrunken hydrogel}}}{W_{\text{swollen hydrogel}}}$$

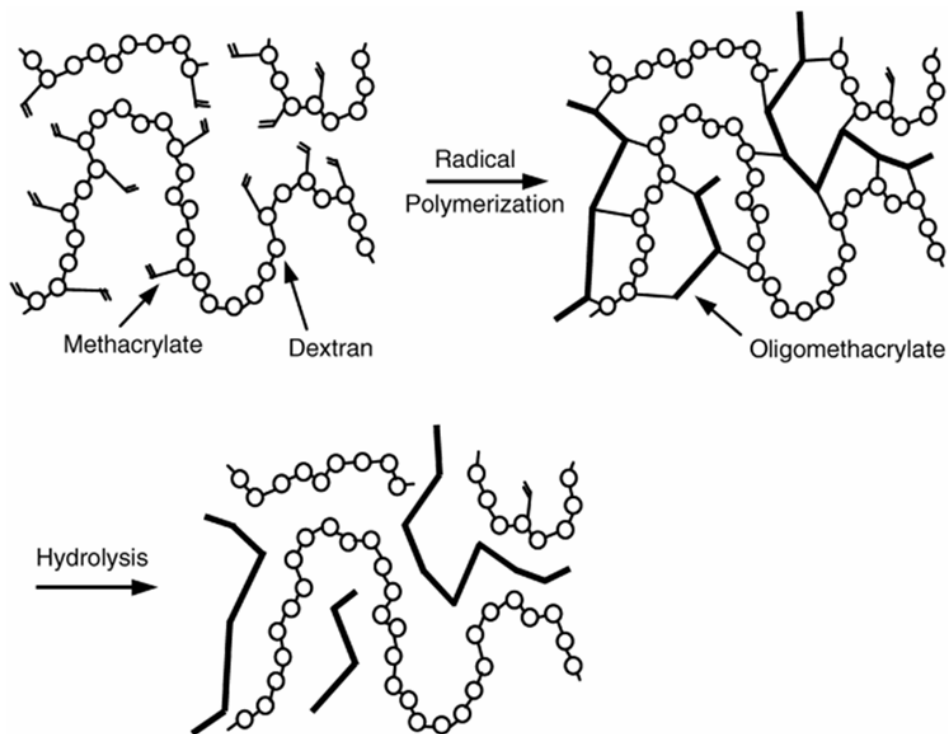


Figure 1.7 Schematic represents the formation and degradation (for dex-HEMA and dex-(lactate)-HEMA) of dextran hydrogels. Gels are formed by radical polymerization of the methacrylate groups using KPS and TEMED as initiator system. Degradation occurs by hydrolysis of the carbonate and lactate ester for dex-HEMA and dex-(lactate)-HEMA, respectively.

1.3.2 Encapsulation of Inorganic Nanomaterials

As mentioned earlier, rational encapsulation of nanomaterials in hydrogel could result in materials with novel and enhanced properties.⁴⁸ In order to combine two distinct and immiscible phases into one uniform composite, special procedure is usually conducted, such as surface functionality modification of nanomaterials, in-situ local polymerization of hydrogel on the surface of nanomaterials, and in-situ formation of nanomaterials inside hydrogel matrix.

In order to encapsulate Fe₃O₄ nanoparticles inside chitosan-grafted-copolymer, Quan *et al.* modified the surface of Fe₃O₄ nanoparticles with bifunctional methyl 3-mercaptopropionate (HSCH₂-CH₂COOCH₃), which was chemically bonded onto the surface of magnetite nanoparticles via Fe-S covalent bonds. This step not only facilitates the hydrophobic/hydrophilic transition, but also provides extra functionality for drug loading.⁵⁰ Zhao *et al.* also utilized thiol-Au nanoparticle chemistry for formation of Au/N-isopropylacryamide composite hydrogel.⁵¹

Local polymerization of hydrogel on the surface of nanomaterials was also widely used. In this case, either monomers or initiators were selectively absorbed on nanomaterials where polymerization only happens on the interface. Kim *et al.* immobilized polymerization initiator [BrC(CH₃)₂COO(CH)₁₁S]₂ onto Au nanoparticles and then did polymerization of N-isopropylacryamide solely on the surface of Au.⁵² There are several advantages for this local polymerization since polymer distribution density and thickness could be controlled by concentration of monomer and reaction time.⁵²

Due to its large water content, another approach is to synthesize nanomaterials inside hydrogel matrix. In this case, hydrogel worked as a mini-reactor. Wang *et al.* reported formation

of Au-NIPAM hydrogel by in-situ reduction of HAuCl_4 with NaBH_4 inside functionalized NIPAM hydrogel. Well-defined Au nanoparticles could be formed on the NIPAM side chains.⁵³

1.3.3 Stimuli-Responsive Materials Based on Hydrogel and Nanomaterials

Due to the selective absorbing and releasing of water, composites based on hydrogels and inorganic nanomaterials could become stimuli-responsive smart materials, whose properties could be tuned by external stimulation. In this regard, controlled drug delivery system, microfluidic valve, and highly sensitive sensor have been developed recently. Xia *et al.* encapsulated drug loaded, hollow Au nanocages with temperature sensitive NIPAM hydrogel. Upon near-infrared light illumination, temperature of Au nanocages increased while drug could be slowly released. When illumination discontinued, NIPAM restored to its original shape and drug delivery ceased. It was also found that delivery rate could be tuned by light density and illumination time.⁵⁴ Hilt *et al.* applied nanocomposite based on Fe_3O_4 nanoparticles and NIPAM hydrogel to form a magnetic field sensitive hydrogel. When Fe_3O_4 nanoparticles were exposed to alternating magnetic fields, increase of temperature was sufficient to trigger the transition of the hydrogel. It has been demonstrated that remote controlled release of molecules (drug delivery)⁵⁵ and flow control (microfluidic valves)⁵⁶ are possible. Besides temperature sensitive hydrogel, other stimulated hydrogels (pH, ion strength) were also coupled with inorganic nanomaterials. Tsukruk *et al.* designed a composite where pH sensitive hydrogel were covered on Ag nanowire-Au nanoparticles.⁵⁷ The change of pH could manipulate the density of Au nanoparticles on Ag nanowires and affect the surface enhanced Raman scattering ability, which could effectively works as a pH sensor.

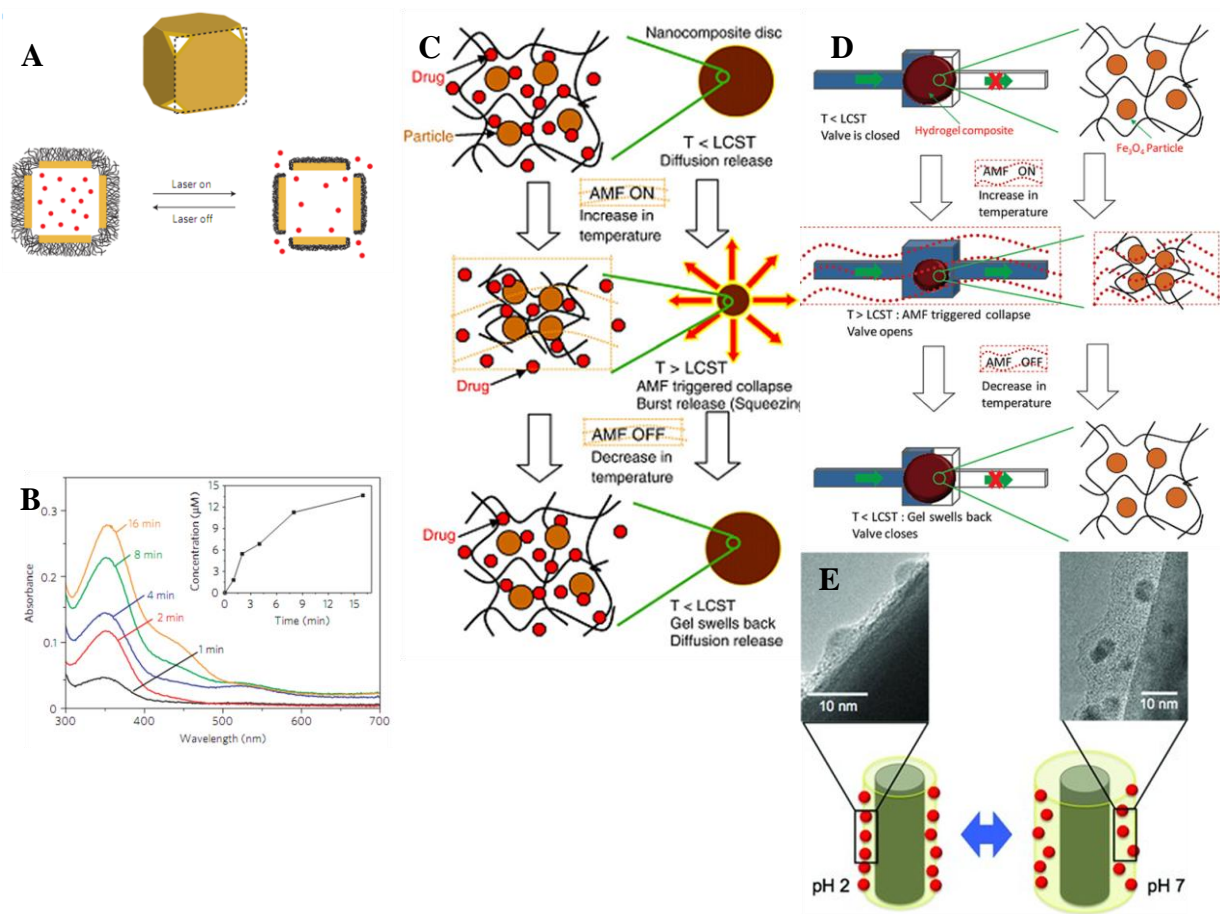


Figure 1.8 (A) Schematic showing (B) controlled releasing of drug from Au-nanocage NIPAM hydrogel (Reprinted by permission from Macmillan Publishers Ltd: Nature Materials (54), copyright 2009). (C) Controlled release of drugs from Fe_3O_4 -NIPAM hydrogel (Reprinted from Journal of Controlled Release, 130, Nitin S. Satarkar, J. Zach Hilt. Magnetic hydrogel nanocomposites for remote controlled pulsatile drug release, 246-251, Copyright (2008), with permission from Elsevier). (D) Schematic of the concept of remote controlled hydrogel nanocomposite valves with an alternating magnetic field. (E) pH triggered aggregation of Au nanoparticles (Reprinted with permission from Maneesh K. Gupta, Sehoon Chang, Srikanth Singamaneni, Lawrence F. Drummy, Ray Gunawidjaja, Rajesh R. Naik, Vladimir V. Tsukruk. Small, 2011, 7(9), 1192-1198, Copyright 2011, John Wiley and Sons).

1.4 Motivation, Challenges, and Goals

1.4.1 Motivation and Challenges

Stimulated by potential applications of CNT-nanoparticle heterostructures, significant advances on synthesis, characterization, and applications have been achieved. However, several challenges and issues still need to be overcome and addressed for wide application of heterostructures. (1) Rational design. Advantages of heterostructures could be fully explored only when different components are rationally organized, where type, size, morphology, location, and density of nanoparticles, diameter, length, and defect site of CNTs are well manipulated. Incorporation of second or even third type of nanoparticles with extra functionality in controlled manner will also be desirable. (2) Large scale, inexpensive, and uniform synthetic approach. Although diverse approaches have been developed, experiments usually were conducted in small scale with low productivity. Moreover, uniformity of synthesized heterostructure was usually not satisfying due to inconsistency and deviation from nanotube to nanotube and batch to batch. Not to mention the linking process through covalent approach involved expensive biomolecules and tedious procedures. Thus, a highly efficient, low cost synthetic approach with decent tolerance will be greatly desirable. (3) Evaluation of the robustness of heterostructures. Various heterostructures were formed under different conditions. Characterization was conducted by electron microscopes and preferred morphologies or linking were confirmed. However, detailed evaluation in the robustness of heterostructures upon perturbation by high temperature and ultrasonication will be critical for the reliability of devices assembled from heterostructures. (4) Fundamental understanding of interaction between CNTs and nanoparticles. Despite extensive research on synthesis and application of heterostructures, formation mechanism, and

explanations for enhanced properties usually based on empirical speculation. Comprehensive and fundamental understanding of how nanoparticles are linked or nucleated on the surface of CNTs, how the introduction of nanoparticles affects the properties of CNTs, what exactly is happening in the nanoscale interfacial junctions are urgently need. This will require understanding of nanoscale CNTs and nanoparticle chemistry as well as in-depth modeling and high resolution, in-situ characterization of nanoparticles, carbon tubes, and their interaction.

As for composite hydrogels, several issues and challenges need to be paid with attention. (1) tuning the composition, dispersity, uniformity of composite hydrogel by surface modification and novel synthetic approaches; (2) in vivo testing of the biocompatibility of composite hydrogels; (3) determination of the long term stability and reliability; (4) exploration of hydrogel types for more stimulus such as moiety, light, sound, physical motion; (5) encapsulation of multiple inorganic nanomaterials for multiple functions.

1.4.2 Goals

The major goal of this thesis is to develop a simple approach for the fabrication of CNT-nanoparticle heterostructures, understand morphological evolution of nanoparticles on CNTs surface, and evaluate such heterostructures for soft nanocomposites or high temperature applications. Due to the unique magnetic, electrical, and catalytic properties, nickel nanoparticles have been widely studied. In this thesis, nickel nanoparticles were selected to decorate the surface of CNTs. Several tasks need to be achieved in this thesis: (1) To develop a simple and highly efficient approach to synthesize CNT-nickel nanoparticle heterostructures; (2) To fundamentally understand the influence of various parameters on size, density, phase, and crystallinity of nickel nanoparticles; (3) To understand the damage of CNTs due to the

introduction of nanoparticles; (4) To understand the effect of CNTs surface modification on decoration density; (5) To evaluate the strength of this heterostructure and understand the disruption of structural integrity and change of chemical states due to high temperature.

In this thesis, poly-vinyl alcohol (PVA) hydrogel was used to encapsulate as-prepared heterostructures because of its good biocompatibility, simple preparation, and unique water absorption ability. Several tasks need to be achieved in this thesis. (1) To prepare composite hydrogel comprised of uniform dispersed heterostructure inside PVA matrix; (2) To understand the effect of heterostructure on the properties of the hydrogel; (3) To study the effect of hydrogel inside mixture solution; (3) To load molecules into hydrogel; (4) To release molecules from hydrogel and study the effect of external magnetic field.

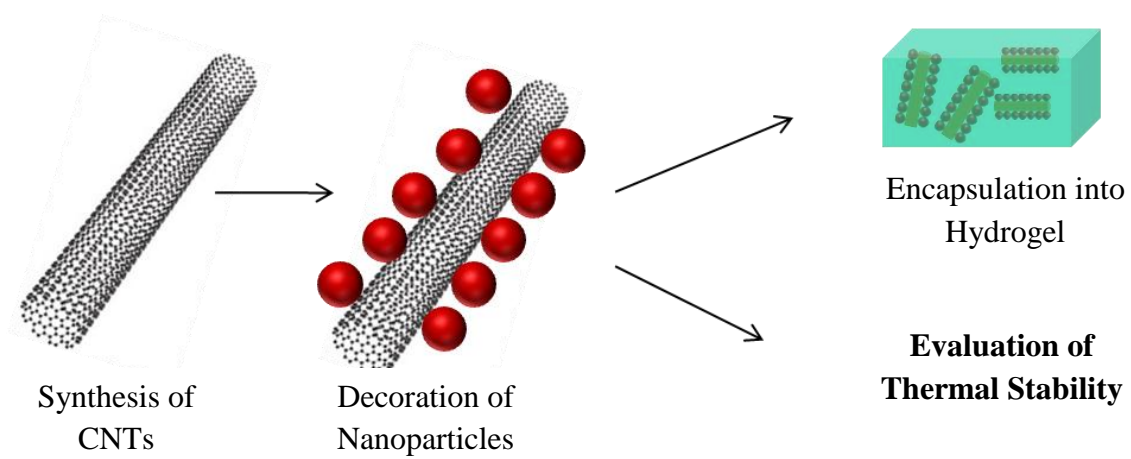


Figure 1.9 Schematic showing goals of this thesis.

CHAPTER 2

EXPERIMENTAL PROCEDURES

2.1 Synthesis of Carbon Nanotubes

CNTs were grown by pyrolysis of xylene and ferrocene mixture under Ar/H₂ atmosphere in a tubular furnace.^{25,26} A schematic of CNTs furnace is shown in Figure 2.1. The ferrocene (catalyst, 0.75% mol, Sigma-Aldrich, St. Louis, MO) was dissolved in xylene (hydrocarbon source, Fisher Scientific, Pittsburgh, PA) to form a dark yellow solution. Furnace was heated to 675 °C with Ar protection (0.5 SLM). Before actual reaction, ~ 2 mL xylene/ferrocene mixture was pumped into the system to fill the gap between gas line and carbon source feed line. The mixture was then injected at 1 mL/h and preheated to 175-200 °C prior to its introduction into the furnace. The CNTs growth occurred in the reaction zone of the furnace at 675 °C under the flow of argon and 10% (v/v) hydrogen for 2 hrs. The as-produced CNTs were collected from the tube wall.

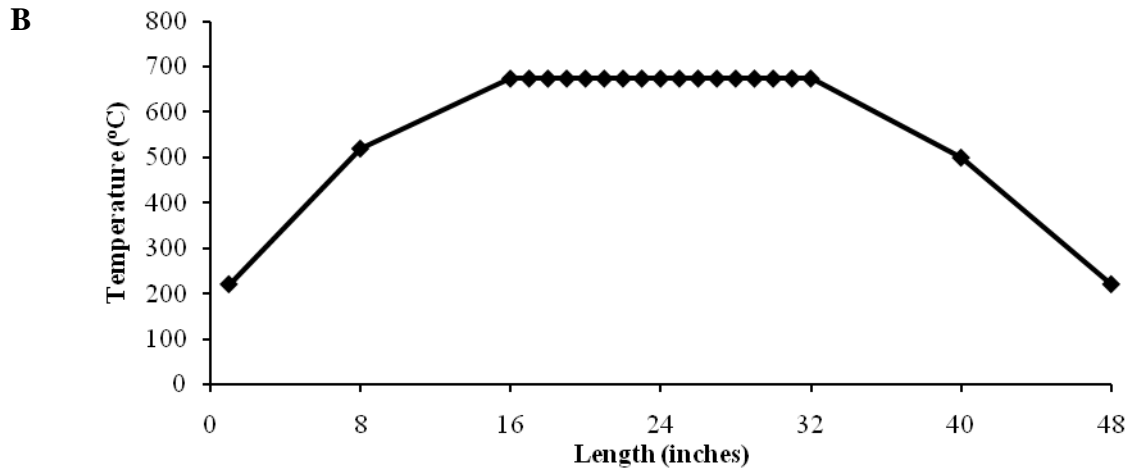
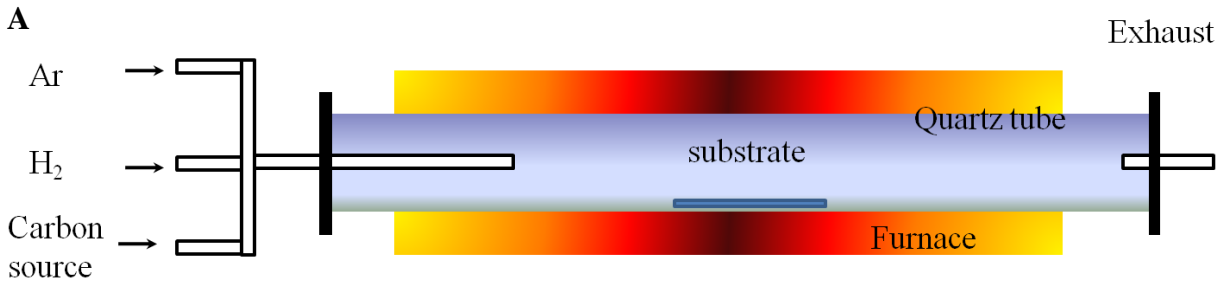


Figure 2.1 Schematic (A) and temperature profile (B) of chemical vapor deposition furnace for CNTs growth.

2.2 Single Parameter Controlled Synthesis of CNC Heterostructures

Ni nanoparticles were nucleated directly on CNTs in a simple and single step wet-chemical process. Products were exposed to air to form NiO shell around Ni core leading to the formation of CNC heterostructures.⁵⁸ Briefly, 1.00 g nickel acetate tetrahydrate, 7 mL oleylamine, and 0.01g CNTs were mixed in a beaker and magnetically stirred for 10 min followed by 30 min ultrasonication. The black mixture was transferred into a three-neck round bottom flask kept in a silicone oil bath. The mixture was held at 90 – 95 °C under N₂ atmosphere for 40 min. Subsequently, 1.50 g TOPO and 1 mL TOP were added into the hot solution. The temperature was gradually increased from 90 °C to 250 °C at ~ 10 °C/min and then held at 250 °C for a certain amount of time (15 min-15 hrs). After the reaction, the flask was cooled in air and ethanol was used to precipitate heterostructures by centrifugation at 6000 rpm for 10 min. Finally, the precipitate was washed several times with a mixture of hexane and acetone. Obtained powders were dried in a vacuum oven at 80 °C overnight and stored in a glass vial in air for further experimentation and characterization.

2.3 Synthesis of Composite Hydrogel Based on CNC Heterostructures

The detailed approach was showed schematically in Figure 2.2. A sample of ~ 0.03 g washed and dried CNC heterostructure was dispersed in water by ultrasonication for 1 min and shaking for 120 min in a vial. Subsequently, PVA (99+% hydrolyzed, M.W=89000-98000, Aldrich, St. Louis, MO) solution in water (ratio PVA:water = 15:85, w/w) was added to the CNC heterostructure solution. The mixture was stirred at room temperature for 60 min and then in hot oil bath (95 °C) and refluxed for 6 hrs. The temperature was decreased to 60 °C and the black-colored sticky mixture was degassed for 10 min and cast in a 4-inch Petri dish. Finally, crystallization of the PVA hydrogel with heterostructures was carried out by repeatedly freezing (-20 °C, 12 hrs) and thawing (room temperature, ~ 22 °C, 12 hrs) for two cycles.⁵⁹ Control samples of pure PVA hydrogel without any heterostructures were also prepared in a similar freezing and thawing cycles.

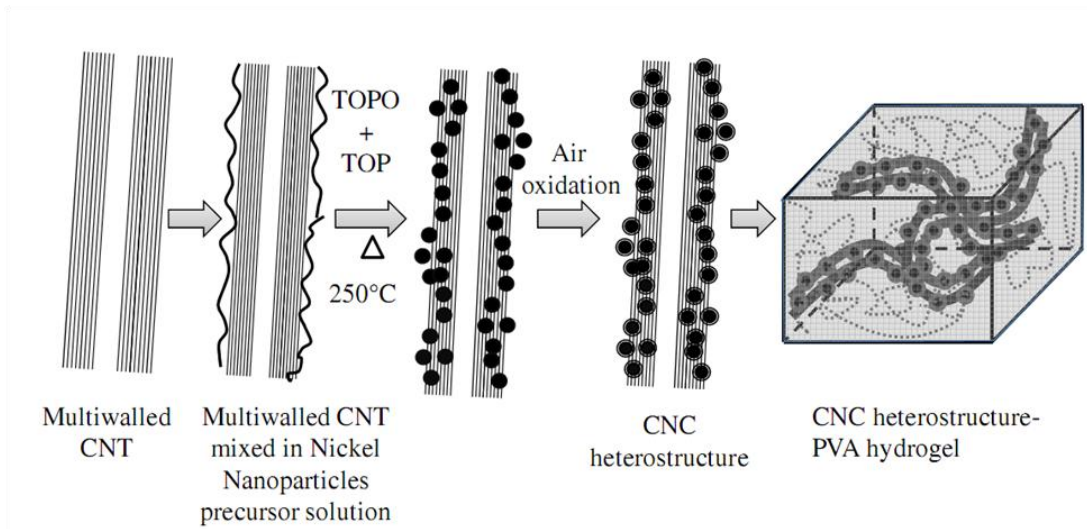


Figure 2.2 Approach for the fabrication of CNC heterostructure-PVA hydrogel.

2.4 Absorption and Concentration Ability of Composite Hydrogel

Air dried CNC heterostructure-PVA hydrogel film (four samples, $\sim 0.5 \text{ cm} \times 0.5 \text{ cm}$) or PVA hydrogel film (control sample, $\sim 0.5 \text{ cm} \times 0.5 \text{ cm}$) weighing $\sim 0.10 \text{ g}$ was immersed in different vials containing a) 5 mL of green fluorescent protein (GFP, N-terminal his-tagged fusion protein corresponding to full-length GFP, expressed in *E. coli.*, Millipore, Temecula CA) solution. This solution was obtained from a solution of 10 μL GFP in 50 mL PBS buffer, b) 5 mL methyl orange solution (0.05 mM in DI water), c) 5 mL L-histidine solution (0.05 mM in DI water), d) 5 mL solution composed of L-histidine mixed with methyl orange solution (2.5 mL 0.05 mM L-histidine mixed with 2.5 mL 0.05 mM methyl orange). All reactions were conducted in capped vials at 4 $^{\circ}\text{C}$ in refrigerator and in dark (covered with an aluminum foil). Characteristic absorption peaks of GFP (263 nm), methyl orange (465 nm), and L-histidine (210 nm) were collected by UV-vis spectrometer as a function of time (0 – 120 min) and swelling for each of the two hydrogel samples. According to Beer-Lambert equation,⁶⁰ concentration is proportional to the absorbance peak. Concentrations were normalized by the equation (2-1), where C_t , I_t , C_0 , and I_0 are concentration of solution and intensity of characteristic peak at time t and $t=0$, respectively. In order to demonstrate the absorption of molecules, ratio of mole numbers was also calculated by multiplication with volume of solution. For absorption, the volume of solution was estimated from EWC data. For concentration experiments, volume of solution was derived by assuming that the highest concentration is due to full absorption of water.

$$\frac{C_x}{C_0} = \frac{I_x}{I_0} \quad (2-1)$$

$$\frac{C_x V_x}{C_0 V_0} = \frac{n_x}{n_0} \quad (2-2)$$

2.5 Controlled Release of Dye Loaded Hydrogel

Around 0.08 g of cleaned and dried CNC heterostructures were physically adsorbed with L-histidine in DI water and incubated for 1 hr. Simultaneously a PVA solution (in DI water) was prepared by mixing PVA and Polyethylene Glycol (PEG-600) and refluxed at 95 °C with stirring for 1 hr. In the next step, the prepared CNC heterostructures loaded with L-histidine were mixed in the polymer solution. The resulting sticky solution was then poured into a 2-inch Petri dish and frozen at -20 °C for 24 hrs. The hydrogel was thawed and dried inside the hood at ambient temperature. This process lead to the formation of CNC heterostructure-PVA hydrogel loaded with L-histidine. The magnetic character of these hydrogels was tested by actuating them under a 0.2 T permanent magnet.

Multifunctional CNC heterostructure-PVA hydrogel loaded with L-histidine was observed for its release behavior with and without external magnetic field. For all the experiments, 50 mg dried hydrogel was immersed in 50 mL DI water at room temperature and gently shaken. Every 5 minutes, a 3 mL solution was tested for UV absorbance peak of L-histidine (213 nm). This release was also studied by keeping a 0.2 T permanent magnet outside the beaker containing the CNC heterostructure-PVA hydrogel and measuring the UV absorbance of the released L-histidine.

2.6 Thermal Stability of Carbon Nanotubes and CNC Heterostructures

In order to determine high temperature stability, CNC heterostructures in acetone were drop-cast on an n-type, (100) pre-cleaned silicon wafer. Silicon wafers with heterostructures were dried in air at room temperature and then placed in a box furnace purged with ~ 1.5 psi N₂-rich atmosphere at different temperatures (125 °C, 200 °C, 400 °C, 600 °C, and 750 °C) for 1 hr each. Control samples comprising as-produced CNTs were heated similarly. The samples were characterized by microscopy, XPS, and Raman spectroscopy. The XPS for the annealed heterostructures was gathered by Kratos Axis 165 with Al mono-gun (10 mA, 12 kV, $h\nu = 1486.7$ eV). Silicon wafer with annealed heterostructures was cut into ~ 5 mm × 20 mm strips and directly mounted onto a conductive sample holder secured with a grounded copper bolt. Before data collection, XPS chamber was pumped down to below 10⁻⁸ Pa. Pass energy of the detector was set at 160 eV. The analysis spot was set as “Slot” with > 20 μm aperture size and 19.05 mm iris setting. For survey spectra, step energy (eV), dwell time, and number of sweep number were set at 1 eV, 100 ms, and 1, respectively. For individual elemental spectra (C 1s and O 1s), step eV, dwell time, and sweep number were set as 0.1 eV, 100 ms, and 2, respectively. For Ni 2p and Fe 2p spectra, number of sweeps were increased to 6 while the other two parameters were 0.1 eV and 100 ms, respectively. In order to eliminate the effect of charging of the semiconducting silicon wafer, all spectra were calibrated using C 1s (284.8 eV) as a standard line. For data processing, all spectra were fitted by XPS peak 4.0 software⁶¹ using linear background subtraction. The atomic ratios of different chemical species were derived by calculation of peak area. Detailed synthetic method and experimental steps were demonstrated in Figure 2.3.

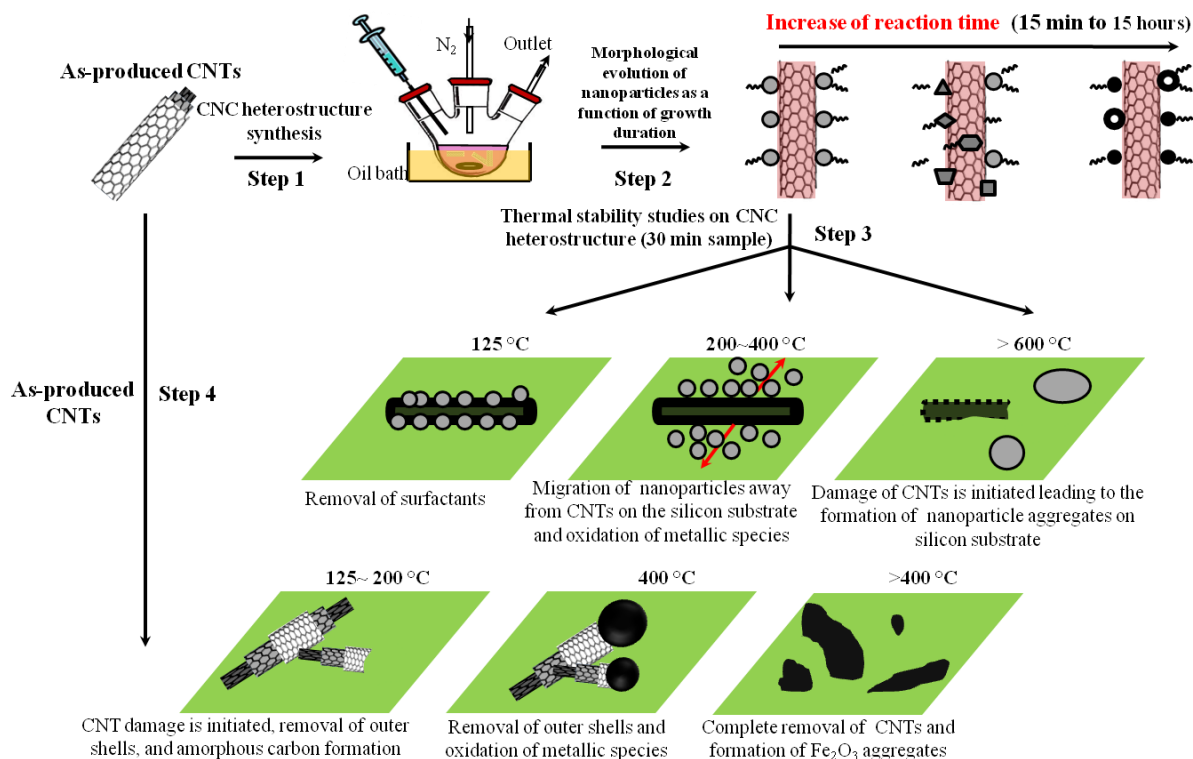
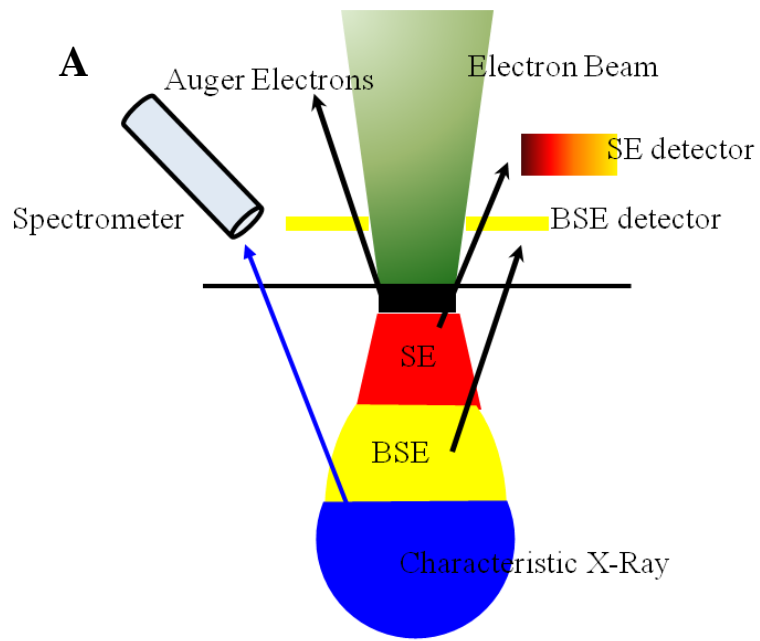


Figure 2.3 Experimental approach for the synthesis of CNC heterostructures (step 1), structural evolution of nanoparticles on CNTs surface (step 2), and thermal stability of CNC heterostructures (step 3) and as-produced CNTs (step 4). Note: 15 hrs of growth resulted in Ni₁₂P₅ nanoparticles on the CNTs surface. The growth time indicates the duration for which the heterostructure synthesis was performed after the addition of TOPO and TOP into the reaction mixture and the temperature stabilized to ~ 250 °C.

2.7 Characterization

2.7.1 Scanning Electron Microscopy

Scanning Electron Microscopy (SEM) is a power technique to observe morphology of materials at high magnification. It has many advantages such as simple sample preparation, great depth of field, ability for both qualitative and quantitative analysis using an EDX detector. High energy focused electron beam bombards the sample surface. The interaction between electron beam and sample will generate secondary electrons (SE), backscattered electrons (BSE), characteristic X-rays and Auger electrons. A typical illustrative image of interaction between electron beam and sample was demonstrated in Figure 2.4. SEM images were generated by recording intensities of electrons at different locations. SEM could be categorized into SE and BSE modes, which are based on detection of either secondary electrons or backscattered electrons. In this thesis, SEM images were collected using a JEOL 7000 and only SE mode was used. Energy Dispersive X-ray Spectroscopy (EDX) spectrum was collected using an Oxford detector. For insulating hydrogel samples, samples were coated with a thin layer of Au to generate electron travel path before SEM images collection.



B



Figure 2.4 (A) Schematic showing interaction between electron beam and sample. (B) image of JEOL 7000.

2.7.2 Transmission Electron Microscopy

Transmission Electron Microscopy (TEM) was utilized in this thesis for high magnification, high resolution morphology characterization. Compared with SEM, where the detector is positioned on the top of the sample, higher energy electrons are used to penetrate samples. TEM images are recorded under the sample using a CCD (charge-coupled device) camera. In general, a certain amount of sample is initially dispersed into either ethanol or acetone to form uniform dispersion. A TEM sample is prepared by dropping one drop of solution onto a lacey carbon coated TEM copper grid. Before inserting into the TEM chamber, the grid is dried in a vacuum oven for at least 2 hrs. All TEM images were collected at 200 kV accelerating voltage. A high-angle annular dark field (HAADF) detector was used to collect scanning transmission electron microscopy (STEM) images. EDX spectra were collected (spot size 9, tilt angle 15 °). Electron diffraction patterns were recorded onto photosensitive films. Figure 2.5 shows a photograph of Tecnai F-20 TEM used in this thesis.

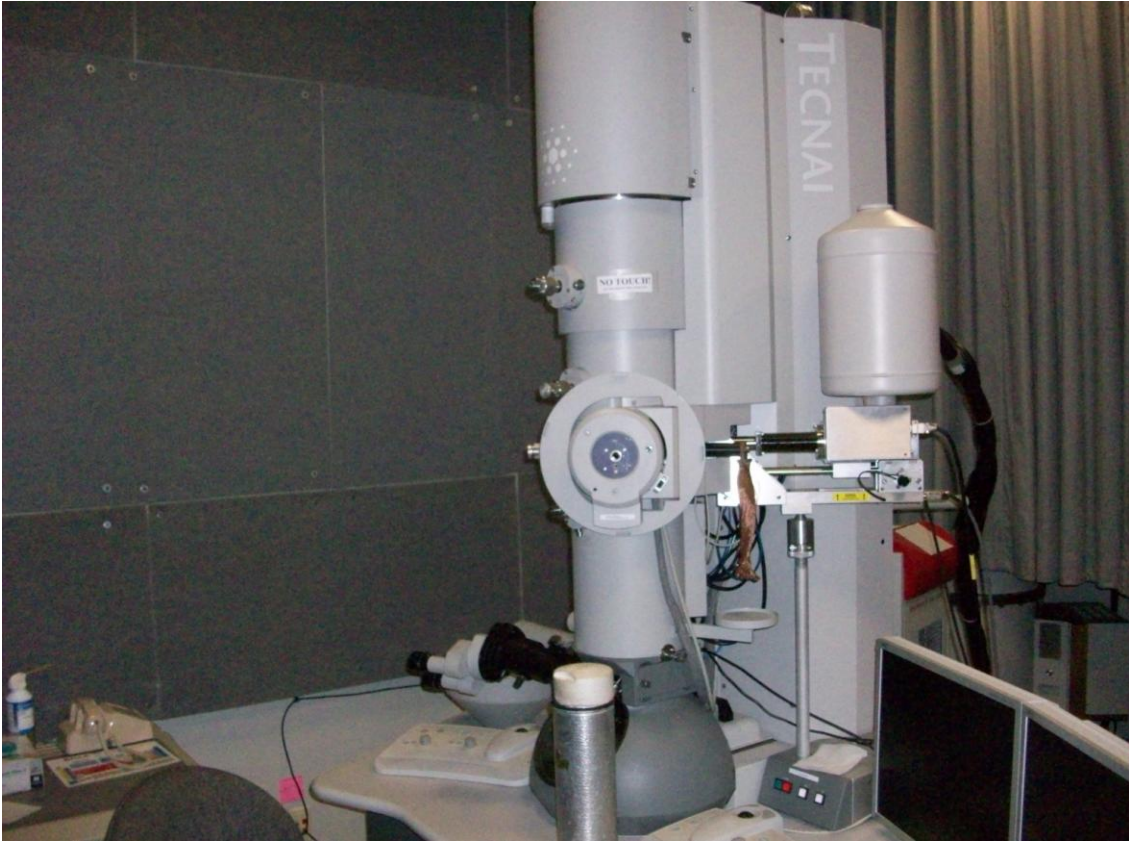


Figure 2.5 Digital image of Tecnai F-20 Transmission Electron Microscopy.

2.7.3 X-ray Diffraction

X-ray diffraction (XRD) was utilized to identify the phase and crystallinity of as-prepared samples. It is well known that when X-ray bombard onto crystallized sample at certain incident angles, strong reflection of X-rays is generated if Bragg's law is meet. Detailed illustration is demonstrated in Figure 2.6.

2.7.4 X-ray Photoelectron Spectroscopy

A detailed schematic showing the operation fundamentals and image of X-ray Photoelectron Spectroscopy (XPS) utilized in this thesis (Kratos Axis 165) is presented in Figure 2.7. X-ray Photoelectron Spectroscopy was utilized to determine the chemical states and quantitatively analyze the atomic percentage of each element. Generally, high energy X-rays interacted with the surface of a sample, where core electrons were knocked out with certain kinetic energy. Kinetic energies of electrons were determined. Since the energy of incident X-ray is fixed, binding energy of core electron could be derived according to the following equation.

$$h\nu = E_{\text{binding}} + E_{\text{kinetic}} + \phi \quad (2-3)$$

$h\nu$ is the energy of incident X-rays and ϕ is the working function of the detector.

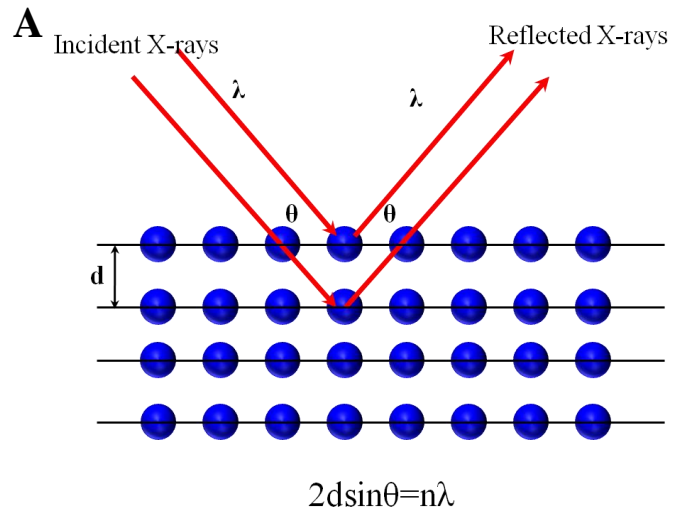


Figure 2.6 (A) schematic showing Bragg's law. (B) Digital image of X-ray Diffractometer.

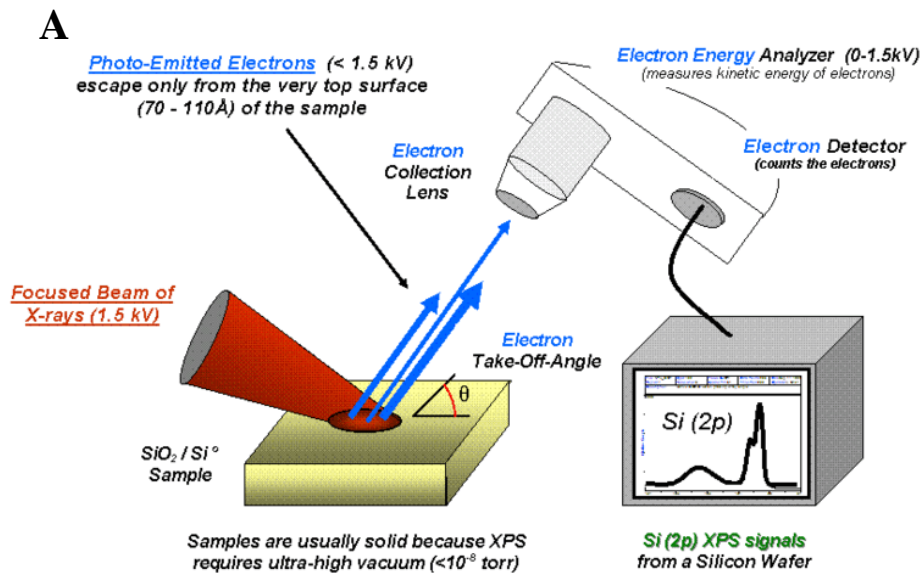


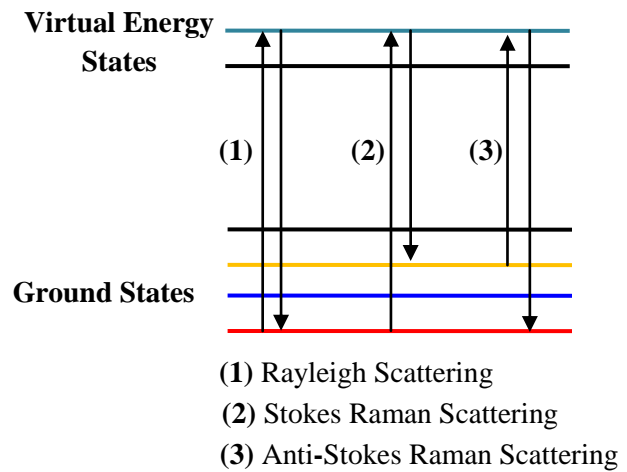
Figure 2.7 Schematic of X-ray photoelectron spectroscopy (Reprinted with Permission from Wikipedia). (B) Digital picture of Kratos Axis 165.

2.7.5 Raman Spectroscopic Characterization

Raman spectroscopy is used to study vibrational, rotational and other low-frequency modes in molecules or crystals. When materials interact with light, most photons are elastically scattered with the same frequency and wavelength (Rayleigh scattering). However, there are small percentage of scattered photons possessing higher energy or low energy than the incident light, which are well known as Stokes Raman scattering (lower energy, positive chemical shift) or Anti-stokes Raman scattering (higher energy, negative chemical shift). When photons excite molecules from ground states to virtual energy states, molecules relax and emit photons, and then return to different rotational or vibrational states. Frequency of emitted photon shifts away from original excitation wavelength. Detailed energy transition was demonstrated in Figure 2.8.

Bruker Senterra system equipped with 785 nm laser was utilized in this thesis. Overview images of samples were collected at 100X magnification using a CCD camera. Raman spectra were collected at 10 mW, 20 s integral time and 2 co-additions. For some experiments where strong fluorescence emerged, auto-fluorescence rejection function equipped in the OPUS software was utilized. Figure 2.8B shows a digital picture of Senterra system.

A



B



Figure 2.8 (A) Schematic of Raman scattering. (B) Bruker Senterra Raman system.

2.7.6 UV-vis spectroscopy

UV-vis spectroscopy is based on the absorption of molecules in UV or visible light regions. In this thesis, UV-vis spectra were used to determine the concentration of molecules of interest released from hydrogel based on Beer's law, where the concentration of chemicals is directly proportional to intensity of absorption peaks.

$$A=\epsilon bc \quad (2-4)$$

Where A is absorbance (no units), ϵ is the molar absorptivity with units of $L \text{ mol}^{-1} \text{ cm}^{-1}$ b is the path length of the sample, which is the path length of the cuvette in which the sample is contained, c is the concentration of the compound in solution, expressed in mol L^{-1} .

Ocean optics USB-4000 spectrometer equipped with DH-2000 UV-vis-NIR light source was used to collect UV-vis spectra (Figure 2.9). All collections were conducted inside quartz cuvette.

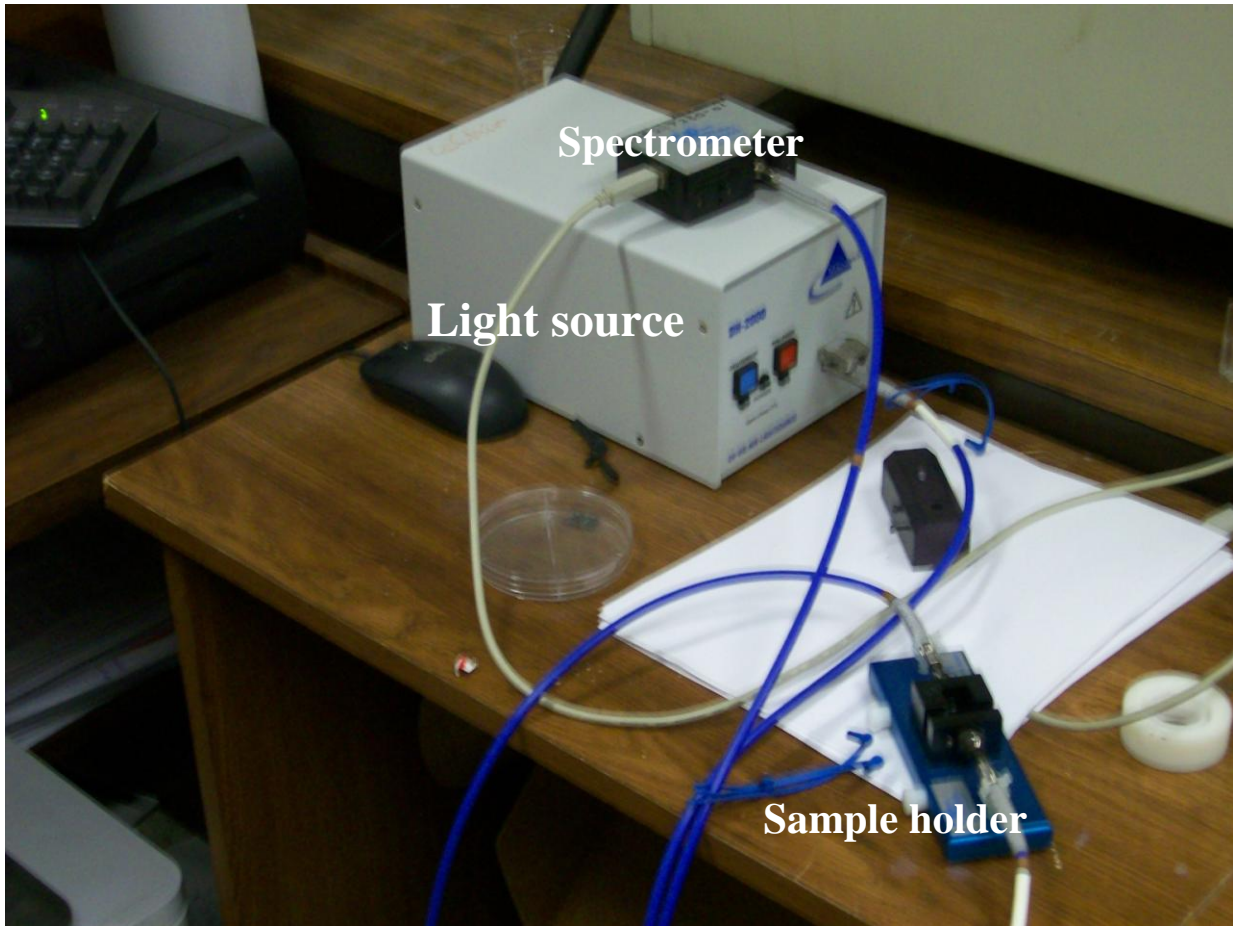


Figure 2.9 Digital pictures of UV-vis spectrometer.

2.7.7. Fourier Transform Infrared Spectroscopic Characterization

Fourier Transform Infrared Spectroscopy (FT-IR) was widely utilized to identify structure of organic molecules. When infrared radiation passes through a sample, some portion of light is absorbed by the sample while other part passes through the sample. By plotting the intensity of absorption or transmission with wavelength of light, the resulting spectrum could represent the molecular absorption and transmission, which provide with information about functional groups and molecular structures of the sample.

FT-IR spectra of PVA hydrogel as well as composite hydrogel were collected using JASCO 4100 FT-IR spectrometer at 1.0 cm^{-1} resolution with KBr pellet as background. FT-IR samples were prepared by mixing knife scratched hydrogels into pre-dried KBr (1%, w/w).

CHAPTER 3

RESULTS AND DISCUSSION

3.1 Synthesis and Characterization of Carbon Nanotubes

Since the first discovery by Iijima back to 1991, CNTs have been attracting enormous attention due to its excellent electronic, mechanical, and optical properties. CNTs could be considered as concentric rolling of graphene sheets. Depending on layers of graphene sheets, CNTs can be categorized as single-walled carbon nanotubes (SWCNTs) and multi-walled carbon nanotubes (MWCNTs). SWCNTs can be further classified based on its rolling vector. Different methods have been developed to fabricate CNTs include chemical vapor deposition, laser ablation, and electric arc.

CVD process is one of the most scalable and high-throughput growth approaches for CNTs production.^{8,25,26} Our CVD approach utilized floating catalyst method, where xylene and ferrocene mixture was used as the carbon source and catalyst precursor, respectively. This was fed into a quartz tube CVD reactor along with H₂/Ar gas mixture. The injector tip temperature allowed for the decomposition of ferrocene and xylene as the feed entered the reactor tube.²⁵ The carrier gas (Ar) swept away the precursors to high temperature zone resulting in the formation of CNTs. Figure 3.1 shows the SEM and TEM images of the as-produced CNTs. These CNTs were also aligned on the quartz substrate as well as quartz tube inner walls as shown in Figure 3.1A (arrow). The high-resolution TEM images (Figure 3.1D and E) show the inter-planer or wall

spacing ($\sim 0.35 \pm 0.01$ nm) of the graphene layers comprising the MWCNTs, consistent with c-axis spacing of graphene sheets in graphite.^{8,25} This was further confirmed by electron diffraction results showing in Figure 3.1F. Electron diffraction showed Fe catalytic nanoparticles as body-centered cubic (002), (112) (103), and (222) with lattice constants at around 0.287 nm.^{62,63} Additionally, (10-10), (0004), and (11-20) planes of MWCNTs were labeled as hexagonal with $a = 0.246$ nm and $c = 0.680$ nm.^{64,65} As observed, our growth process left behind a few Fe catalyst nanoparticles inside the core of CNTs (shining dots in Figure 3.1B and black dots in Figure 3.1C). In addition, TEM images did not show Fe nanoparticles outside CNTs but encapsulated inside the latter. This Fe content was estimated from EDX to be between 0.19 to 4.42% (Fe/C molar %, Figure 3.2). Since numerous CNTs were observed with nanoparticles at their tips (32%, counting from SEM images) as well as at their bases, it is concluded here that our growth approach simultaneously involved tip and root growth mechanism.⁸ In addition, there was a significantly lower amount of amorphous carbon on the surfaces of CNTs as observed in TEM (Figure 3.1E, arrows). This aspect of the as-produced CNTs made them readily available for the next step of direct nucleation of the nanoparticles on their surface without any cleaning or purification steps. In Figure 3.3, the diameter distribution of CNTs is demonstrated and it turns out that as-produced CNTs exhibited an average diameter of $\sim 45.8 \pm 16.4$ nm and length of ~ 26.5 μm . Furthermore, Raman spectroscopy was utilized to characterize as-prepared CNTs. Two distinctive peaks showed at 1304 cm^{-1} and 1577 cm^{-1} , which are well known as D band and G band from defected carbon and graphitized carbon, respectively.⁶⁶ There is a shoulder located at 1598 cm^{-1} which is from end planes of graphene layers called D' band.

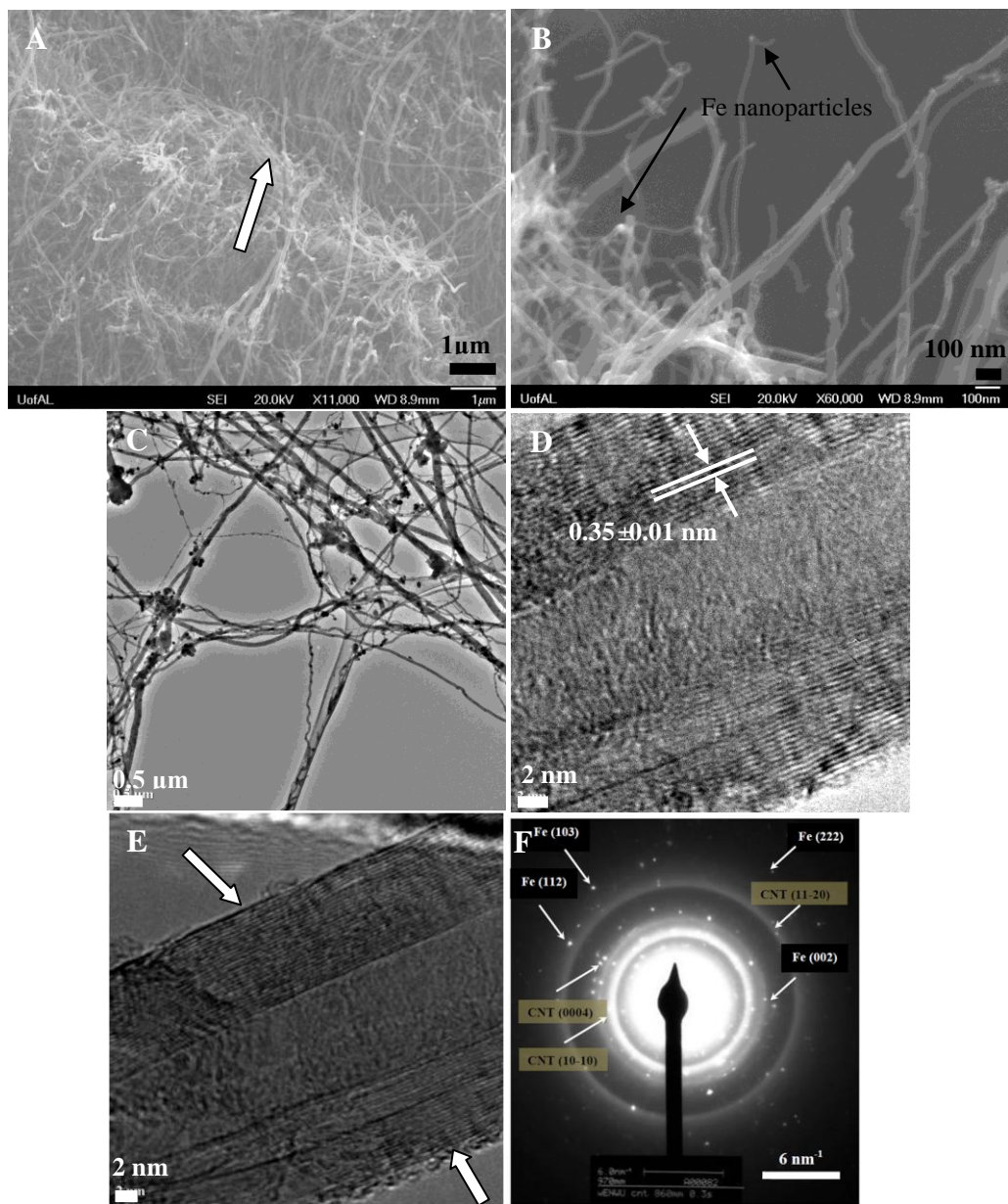


Figure 3.1 (A) and (B) SEM images of CNTs, the arrow in (A) shows the alignment of as-produced CNTs. (C) Low resolution TEM image of CNTs. (D) and (E) High-resolution TEM images showing CNTs walls, inter-wall spacing of CNT, and negligible amount of amorphous carbon present on the CNTs surface (indicated by arrows in (E)). (F) Electron diffraction of as-produced CNTs. Note the CNTs core is ~ 6 nm in diameter.

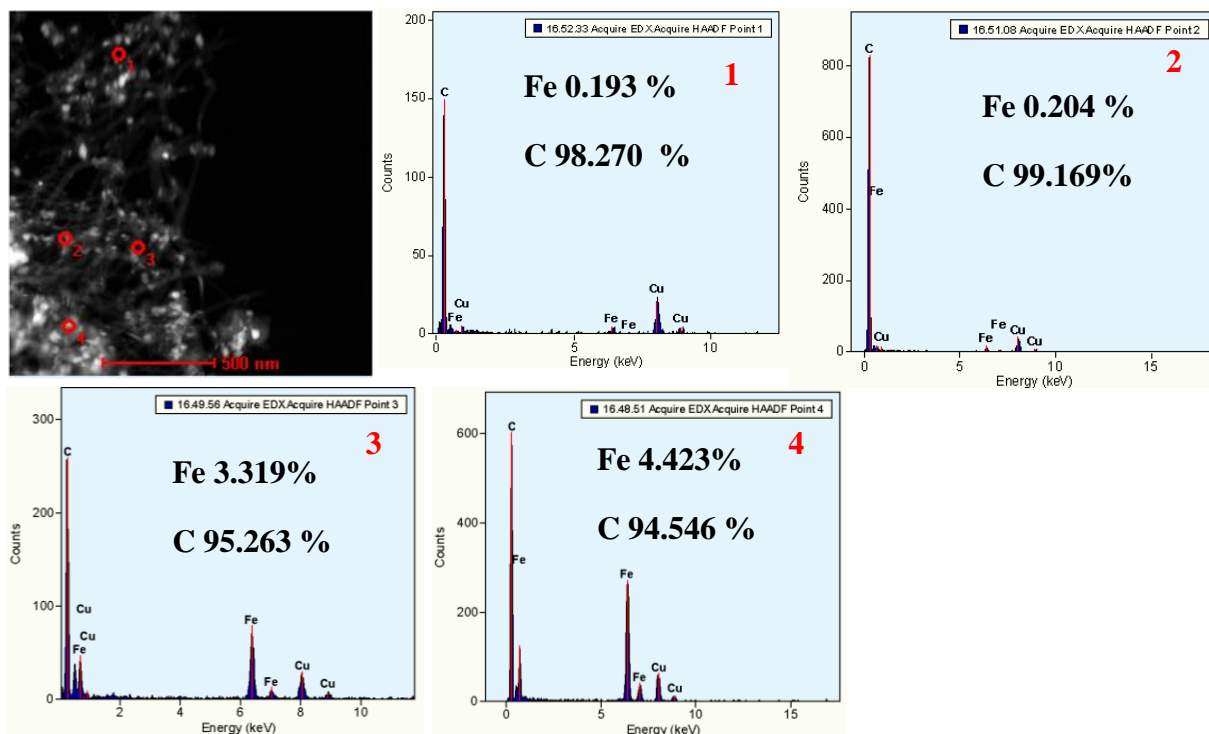


Figure 3.2 HADDF image of as prepared CNTs and typical EDX spectra.

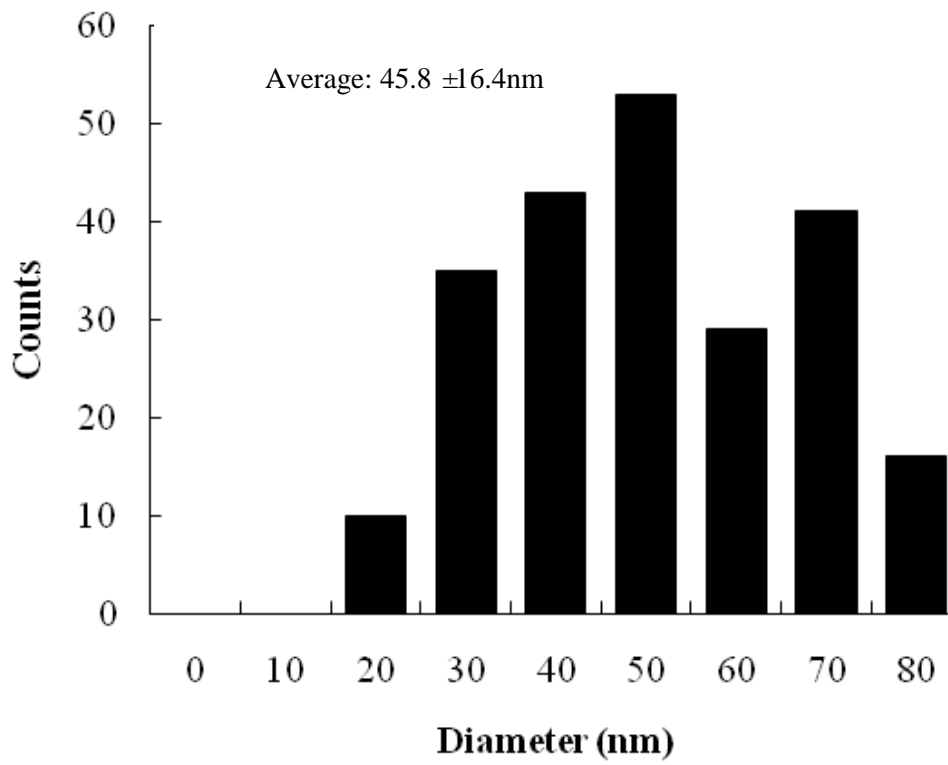


Figure 3.3 Diameter distribution of CNTs.

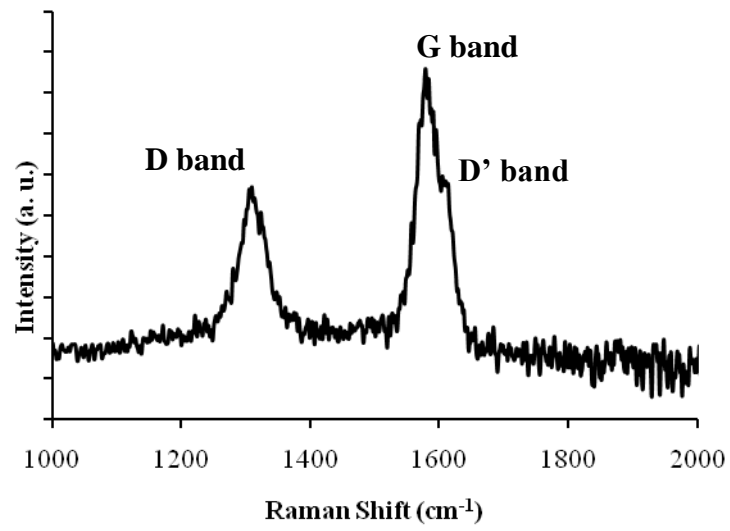


Figure 3.4 Raman spectrum of as-prepared CNTs.

3.2 Synthesis and Characterization of CNC Heterostructures

CNT-metal nanoparticle heterostructures have been prepared by a variety of methods that involve covalent chemistry, spontaneous reduction, and electrodeposition.¹⁶ In this thesis, nickel nanoparticles were heterostructured with CNTs in a single step synthetic approach without involving covalent bonding. It is known that CNTs disperse well in oleylamine.²⁴ Thus, CNTs were mixed with oleylamine and nickel acetate, and heated in an inert (N₂) atmosphere. This facilitated the formation of nickel complex with oleylamine^{10,67} on the surface of CNTs. In the next step, strong stabilizers such as TOPO and TOP were injected into the solution at higher temperatures resulting in the nucleation and growth of nickel nanoparticles directly on the surface of CNTs.^{10,68} Finally, rigorously washed and dried powder was exposed to air to surface oxidize nickel nanoparticles and result in CNC heterostructures. This synthetic approach resulted in non-contaminated heterostructures. SEM shows (Figure 3.5A) Ni/NiO core/shell nanoparticles uniformly decorating CNTs. Figure 3.5B shows that nanoparticle adhered strongly to the CNTs even after ultrasonication treatment (Branson 2510, 100 Watts, 40 kHz) for 30 min. This indicates the robustness of the heterostructure without any chemical bonding between CNTs and nanoparticles. EDX spectrum was also collected and detailed percentage of each element was presented in Figure 3.5C and D. Carbon, nickel, oxygen, and silicon are reasonable since we have CNTs and nickel/nickel oxide core shell nanoparticles dispersed on silicon wafer. Phosphorus was also detected due to the utilization of TOPO and TOP stabilizers. Before loading of nickel nanoparticles, CNTs show no magnetic behavior even though a small amount of iron is present. After loading, CNC heterostructures have a good magnetic response as indicated in Figure 3.6.

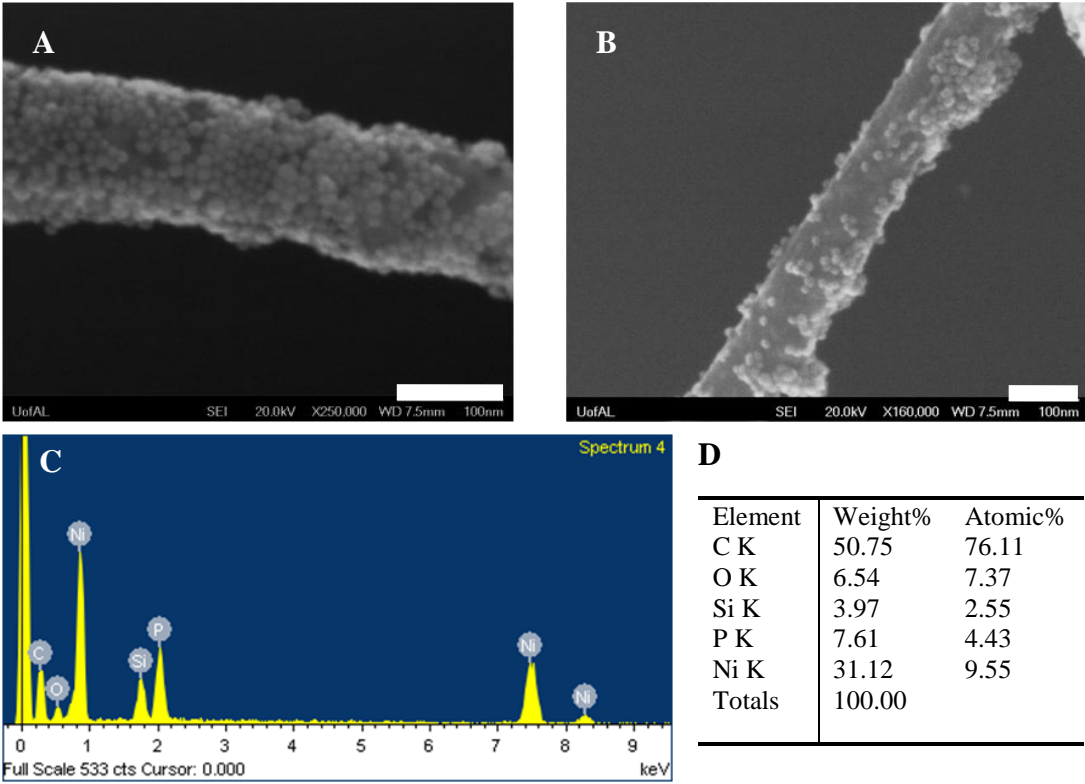


Figure 3.5 (A) SEM image of CNC heterostructures after rigorous washing. (B) SEM image of CNC heterostructure after ultrasonication for 30 min. (C) EDX spectrum of as-prepared CNC heterostructures, (D) Percentages of different elements (silicon is from substrate).

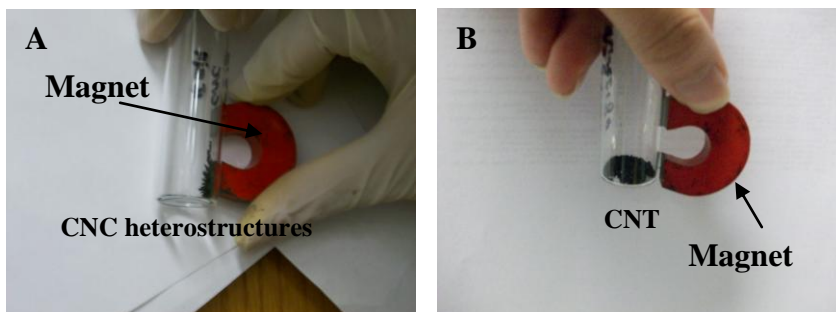


Figure 3.6 (A) Magnetic characteristics of the CNC heterostructures after drying, the growth duration for these heterostructures after addition of stabilizers (TOP and TOPO) was 15 min. (B) The as-produced CNTs are non-magnetic and do not show attraction towards a magnet.

TEM characterization of CNC heterostructures could explain their crystal structure, morphology, and interfacial characteristics. Figure 3.7 shows the TEM images of CNC heterostructures and the uniformity of the nanoparticle coating on CNTs can be clearly seen. CNTs with smaller diameters (< 30 nm) resulted in negligible nucleation of nanoparticles as compared to larger diameters (> 30 nm). In addition, the process of nucleation of nanoparticles on CNTs was found to be 80% efficient. Thus, the curvature of the substrate affects the nucleation of nanoparticles and can be an important parameter in controlling density of nanoparticles on CNTs. These CNTs were multi-walled with a wall spacing (~ 0.35 nm) that corresponds to c-axis spacing of graphene sheets in graphite.⁸ TEM image at higher resolution shows the Ni/NiO core/shell nanoparticles (average diameter $\sim 11.9 \pm 1.8$ nm, Figure 3.8) attached onto a CNT. The interface is indicated by white dotted line in Figure 3.7C. The interplanar spacing (0.21 ± 0.01 nm, Figure 3.7F) of the core nickel nanoparticles corresponds to (111) plane in face centered cubic (fcc) nickel.⁶⁹ As observed, the NiO shell was polycrystalline with a thickness of $\sim 2.1 \pm 0.4$ nm. XRD confirmed the presence of different component in the CNC heterostructures (Figure 3.9). Reflections of cubic NiO (JCPDS card No. 47-1049) were confirmed by the presence of peaks corresponding to (111) and (220) planes. Similarly, fcc Ni peaks (JCPDS card No. 4-0850) were assigned to (111), (200), and (220) planes. A peak at $\sim 26^\circ$ corresponds to (002) planes of CNTs with an interplanar spacing (~ 0.35 nm).⁷⁰ Electron diffraction was also collected to determine phases of CNC heterostructures. Peaks of (111), (200), and (220) nickel were identified (JCPDS 4-850). Since nickel is easily oxidized in air, (111) and (220) of NiO were also found (JCPDS 4-835). (10-10) and (11-20) of CNTs were also labeled.^{64,65}

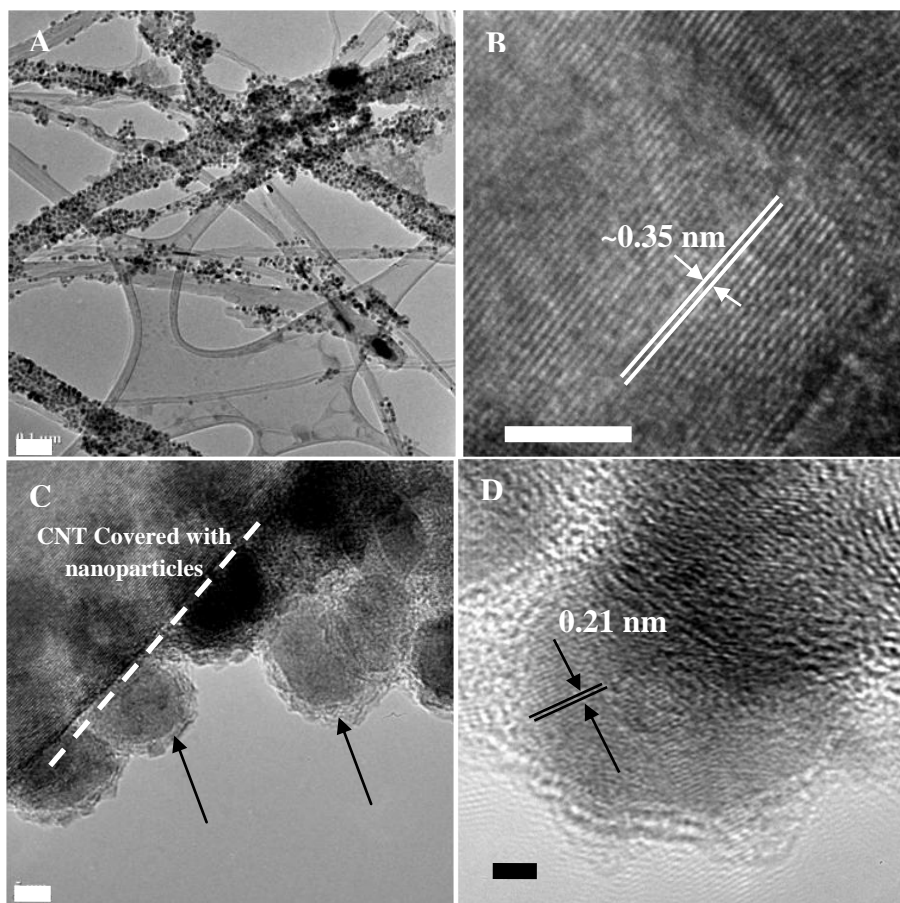


Figure 3.7 (A) TEM image of CNC heterostructure (scale bar: 0.1 μm). (B) High-resolution TEM of CNTs showing the wall morphology and spacing between the walls (scale bar: 5 nm). (C) TEM image indicating attached Ni/NiO core/shell nanoparticles on CNTs (scale bar: 5 nm). White dotted line indicates the interface between the two. Note: There is certain extent of aggregation of nanoparticles on CNTs. (D) High-resolution TEM image of Ni/NiO core/shell nanoparticle showing the (111) interplanar spacing for core nickel nanoparticles (scale bar: 2 nm).

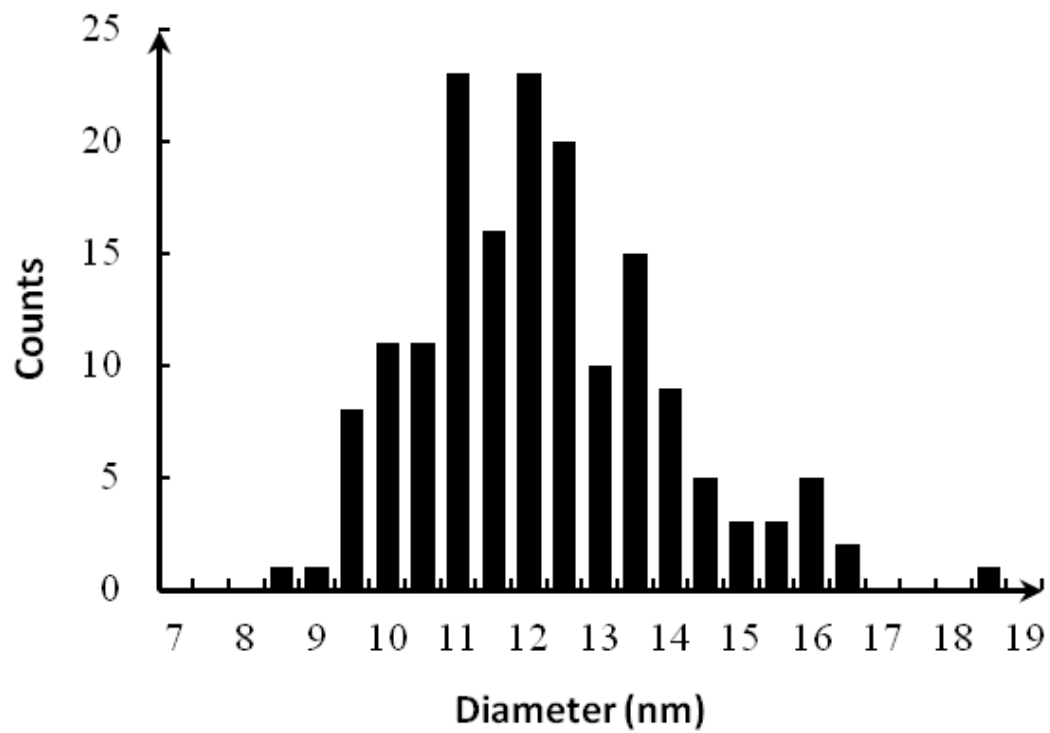


Figure 3.8 Diameter distribution of nickel/nickel oxide core-shell nanoparticles.

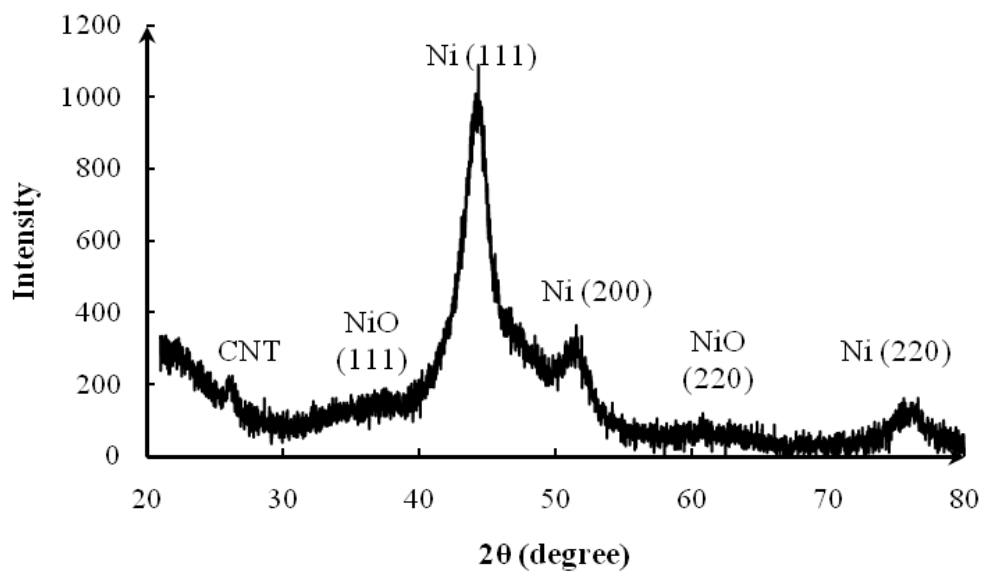


Figure 3.9 X-ray diffraction for CNC heterostructures indicates peaks corresponding to Ni, NiO, and CNTs present in these heterostructures.

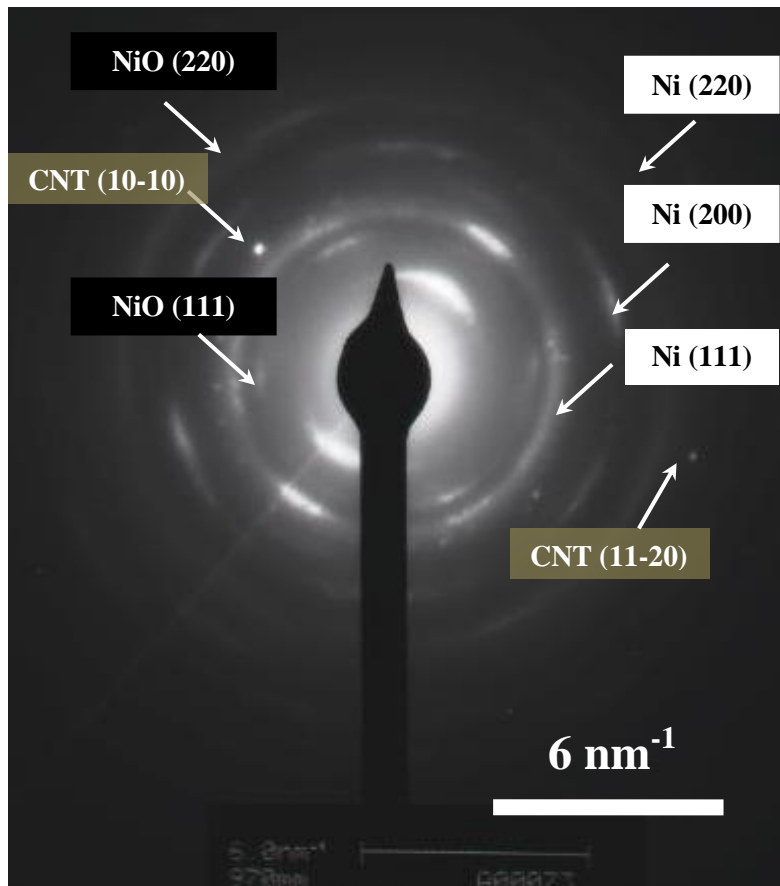


Figure 3.10 Electron Diffraction of CNC heterostructures.

Although NiO shell can be clearly observed in the high-resolution TEM image (shown by arrows in Figure 3.7C), this is further confirmed by Raman spectroscopy (Figure 3.11). Raman spectrum showed two peaks at 1313 cm^{-1} and 1591 cm^{-1} , which were labeled as D and G bands for CNTs in CNC heterostructures.⁶⁶ Spectrum region between 100 cm^{-1} and 1200 cm^{-1} showed peaks located at 418 cm^{-1} , 513 cm^{-1} , 723 cm^{-1} , and 1049 cm^{-1} . These peaks were identified as transverse optical (TO), longitudinal optical (LO), 2TO, and 2LO phonon modes of NiO, respectively.^{71,72} All peaks were shifted down in frequency about $\sim 20\text{ cm}^{-1}$ as compared with NiO single crystal. This could be attributed to laser excitation wavelength ($\sim 785\text{ nm}$) and polycrystalline NiO shell.⁷⁷

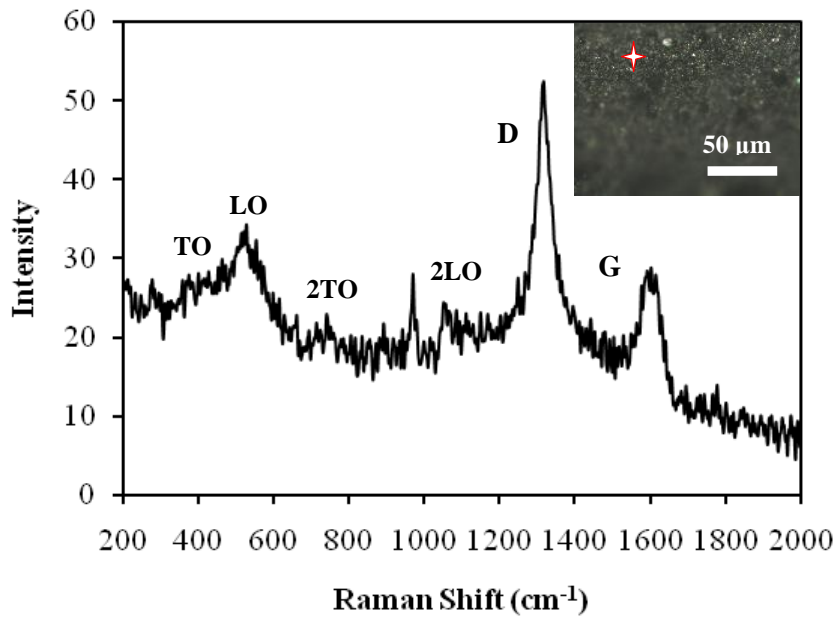


Figure 3.11 Raman Spectrum of CNC heterostructures, a star in the inset picture indicates the place where spectrum was collected.

To understand the effect of CNTs surface functionality on the formation of CNC heterostructures, carboxylic (-COOH) derivatized CNTs⁷³ were obtained after treatment with strong acids. Compared with the as-prepared CNTs, nanoparticles had poor coverage on -COOH derivatized CNTs (Figure 3.12A, 3.12B, and 3.12C). Such derivatization gave hydrophilic character to the CNTs and adversely affected the wetting of CNTs with alkyl-terminated and hydrophobic oleylamine. Oleylamine is a critical stabilizer in CNC heterostructure formation and assists in the formation of nickel complex, which is necessary for Ni nanoparticles nucleation and growth. Thus, poor oleylamine wetting of -COOH derivatized CNTs led to a non-uniform and poor nanoparticle coating. Moreover, aggregated nanoparticles were formed on the CNTs (dotted circles in Figure 3.12A) and clearly observed in Figure 3.12B and C.

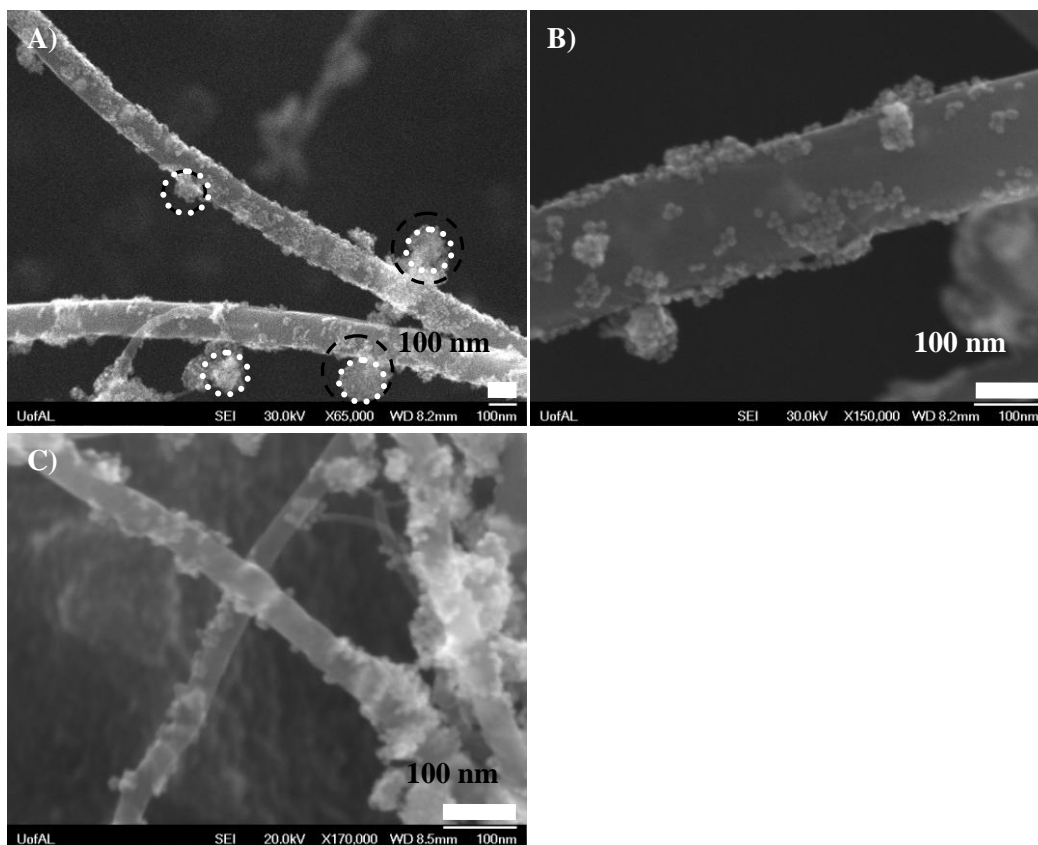


Figure 3.12 SEM images of control sample made from acid-treated CNTs.

In order to determine the surface bond states and composition, X-ray photoelectron spectrums (XPS) were collected for both CNTs and CNC samples (Figure 3.13). All spectra were fitted by XPS peak 4.0 software.⁶¹ For CNT, C 1s peaks indicated existence of C-C bond (284.48 eV), defects (285.43 eV, carbon atoms are not at tubular structure), small amount of C=O (288.78eV), C-O (286.78 eV), and carbonates (291.2 eV).⁷⁴ For O 1s in CNT, two peaks, 531.92 eV (-OH, C=O) and 533.2 eV (C-O) were obtained.⁷⁴ Since in these experiments, raw CNTs without acid treatment or oxidation were used, the O 1s peak for CNTs has low intensity and signal-noise ratio. For CNC heterostructures, only strong C 1s and weak C-H, C-O peaks were observed. The primary reason is that the CNTs in CNC heterostructures were uniformly covered with nickel nanoparticles and carbon source came from stabilizers (TOPO and TOP). P 2p peaks were collected to confirm the presence of phosphorus. Besides P 2p_{3/2} (130.08 eV) and 2p_{1/2} (131.35 eV) peaks,⁷⁴ another strong signal was also observed. This peak was identified as P-O peak from TOPO, which agrees well with other literature.⁷⁴ For CNC heterostructure, O 1s spectrum consisted of two peaks, 533.64 eV and 533.10 eV, which are tagged as O 1s and -OH bond hanging on the surface of NiO, respectively.⁷⁴ For Ni 2p, six main peaks were detected. Fitting showed there are 2p_{3/2} (853 eV), 2p_{1/2} (870.37 eV) for metallic Ni⁰ (Ni core), 2p_{3/2} (855.8 eV), 2p_{1/2} (874.03 eV) for Ni²⁺ (NiO shell) and two other satellite peaks.⁷⁴ Both the locations of peaks and distance between Ni 2p_{3/2} and 2p_{1/2} matched well with other's result. Moreover, N 1s peak for CNC heterostructure was also collected and the absence of a peak confirms that the oleylamine was completely washed away.

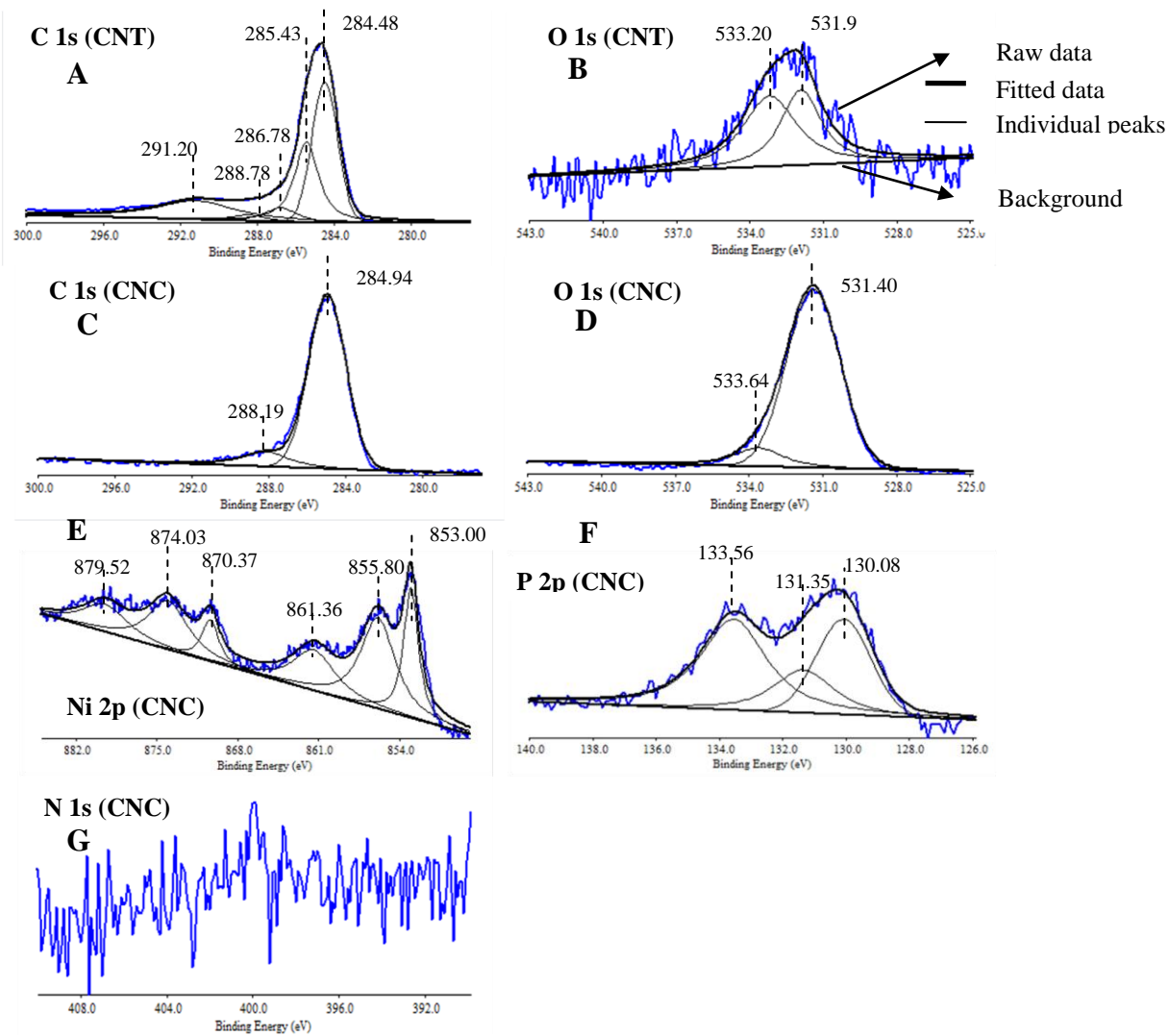


Figure 3.13 XPS spectra subtracted by linear background and fitted with individual peaks as well as overlapped peaks (indicated in Fig.3.13B). (A) C 1s and (B) O 1s spectra for as-produced CNTs. (C) C 1s, (D) O 1s, (E) Ni 2p, (F) P 2p, and (G) N 1s spectra for CNC heterostructures.

Table 1 Identification of XPS peaks

sample name	Element	binding energy ¹	bond	sample name	Element	binding energy	bond
CNT	C	284.48	C-C	CNC	Ni	853	Ni ⁰ 2p _{3/2}
		285.43	Defect ²			855.8	Ni ²⁺ 2p _{3/2}
		286.78	C-O			861.36	satellite
		288.78	-O-C=O			870.37	Ni ⁰ 2p _{3/2}
		291.2	carbonates			874.03	Ni ²⁺ 2p _{1/2}
	O	531.92	-OH, C=O			879.52	satellite
		533.2	C-O			O	531.4
					533.64		O-H ³
C	284.94	C 1s	P		130.08	P 2p _{3/2}	
					288.19	C-H	131.35
						133.56	P-O

1. Unit of binding energy is eV
2. C atoms are not at tubular structure
3. Oxygen containing species localized on NiO surface.(-OH, O²⁻)

3.3 Structural Evolution of CNC Heterostructures Controlled by Single Parameter

To eliminate the need for covalent linking of nanoparticles on the surface of CNTs, we utilized a novel single-step direct nucleation method to coat CNTs with uniform Ni nanoparticles in a chemical synthetic route as outlined in (Figure 2.3, step 1). Oleylamine served two main functions: 1) oleylamine easily wet the surface of CNTs; 2) oleylamine helped the formation of nickel complex directly on the surface of CNTs.⁷⁵ Once the CNTs were mixed with oleylamine and nickel acetate precursor salt, the mixture was heated in an inert (N_2) atmosphere for a fixed duration (40 min). Phosphine-based stabilizers (TOPO and TOP) were then added into the heated mixture and the temperature was stabilized at ~ 250 °C. In order to understand the morphological evolution of the nanoparticles on the surface of CNTs, this reaction was carried out for different durations (Figure 2.3, step 2) ranging from 15 min to 15 hrs and the resulting black precipitate (heterostructure) was washed and dried. Figure 3.14 shows SEM images of heterostructures grown for 15 min and 30 min (Figure 3.14A and B) and 15 hrs (Figure 3.14C and D). There was a big difference in the morphologies of the nucleated nanoparticles for these two growth durations. The nanoparticle coating for 15 or 30 min growth was uniform as compared to 15 hrs. The 15 hrs growth duration also resulted in several micron scale particles and aggregated nanoparticles that were not on CNTs (Figure 3.14B). Further details of morphological evolution of nanoparticles in these heterostructures are discussed next.

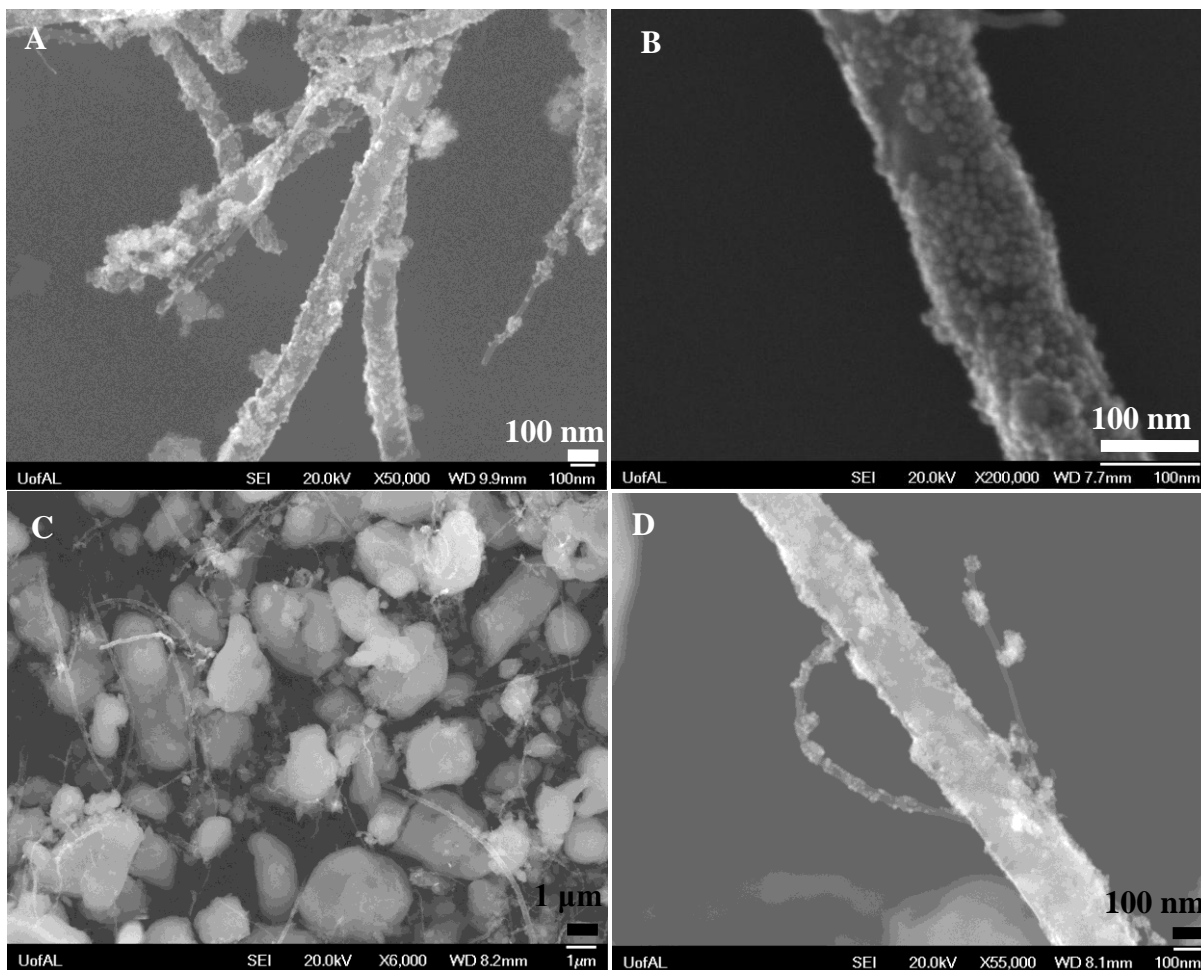


Figure 3.14 SEM images showing CNC heterostructures after (A) 15 min, (B) 30 min, (C) and (D) 15 hrs of growth duration. The nanoparticle coating in (C) is not uniform and large-sized particles are formed that do not decorate CNTs.

Morphological control of nanoparticles on the CNTs surface is very critical for applications of such heterostructures. For example, kinked corners in the nanoparticles⁷⁶ on CNTs can lead to greater charge accumulation or chemical reactivity, excellent for their role as catalysts.⁴⁷ In this regard, single-parameter control of morphology of nanoparticles on the surface of CNTs is highly desired. Thus, as a next step, we performed an in-depth study on the effect of only the reaction duration (after the stabilizer addition) on the growth, crystal structure, chemical composition, and morphology of the nanoparticles nucleated on the CNTs surface. Furthermore, we also analyzed the defects introduced in the CNTs during this process.

Ni nanoparticles were directly nucleated on CNTs and allowed to grow after stabilizer addition for 15 min, 30 min, 2 hrs, 4 hrs, 6 hrs, 10 hrs, and 15 hrs. Further exposure of these heterostructures to air resulted in a thin ($< 2 - 3$ nm), polycrystalline oxide (NiO) shell around the Ni core. The synthesized samples were characterized using TEM (Figure 3.15). TEM images show that as the growth duration was increased, the morphology, size, and nanoparticle spatial density as well as spacing between them changed. Optimal nanoparticle characteristics (spherical), uniformity of the coating, and packing density were observed for 30 min growth duration (Figure 3.15C and D). Beyond 2 hrs growth duration, different shapes of the nanoparticles started evolving on the CNTs surface. It was observed that the lattice spacing of the coated nanoparticles matched predominantly with (111) planes of fcc Ni (~ 0.203 nm Figure 3.15B, F, J, and L, JCPDS No. 4-850). A few hcp Ni lattices were observed corresponding to (002) and (010) planes with lattice spacing of ~ 0.217 nm and 0.230 nm (Figure 3.15B, D, and H, JCPDS No. 45-1027). The schematic shown in Figure 3.15M is derived from the TEM observations, and indicates the morphological evolution of the nanoparticles on CNTs surface as a function of reaction time.

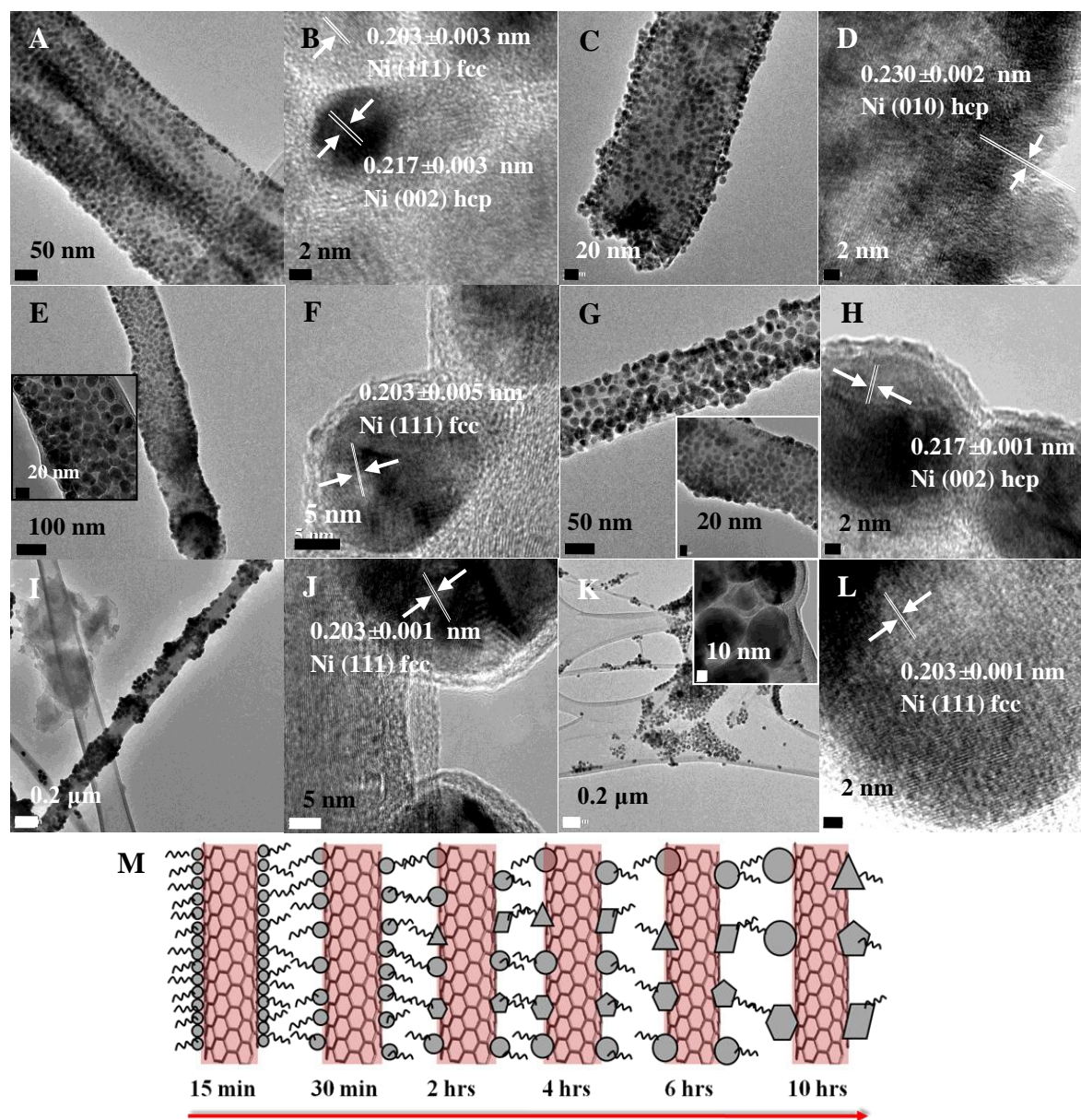


Figure 3.15 TEM images of CNC heterostructures synthesized for (A), (B) 15 min, (C), (D) 30 min, (E), (F) 2 hrs, (G), (H) 4 hrs, (I), (J) 6 hrs, and (K), (L) 10 hrs. Each pair of images and an inset correspond to low and high-resolution TEM images. The polycrystalline NiO shell is observed for the coated nanoparticles. Note: The high-resolution TEM images show the lattice spacing and corresponding planes of the coated nanoparticles. (M) Schematic indicating the morphological evolution of nanoparticles on the CNTs surface as a function of growth time.

Figure 3.16 shows the detailed analysis of the effect of growth duration on the morphological evolution of the nanoparticles on CNTs using TEM characterization studies (Figure 3.15). The diameter distribution histogram (Figure 3.16A) shows that as the growth duration was increased, the size of the nanoparticles also increased. Table 2 indicates that the average size of the nanoparticles increased from $\sim 12.5 \pm 2.1$ nm (15 min of growth duration) to $\sim 51.8 \pm 9.8$ nm (10 hrs of growth duration). Based on TEM observations, it was possible to estimate the spatial density of nanoparticles (Figure 3.16B) and inter-particle spacing (Figure 3.16C) on the surface of the CNTs. The spatial density or distribution of nanoparticles on the surface of CNTs was estimated to have decreased by 97.1% as the reaction duration was increased from 15 min to 10 hrs. In addition, as the size of nanoparticles increased and the spatial distribution decreased, inter-particle spacing increased by ~ 9 folds for 10 hrs as compared to 15 min growth duration. Figure 3.16D shows that almost 95% of nanoparticles on the surface of CNTs were spherical (or circular, if a planar projection is considered) for 15 min reaction duration as compared to different shapes observed for higher reaction duration (> 2 hrs). The percentage of spherical nanoparticles reduced to 24% for 10 hrs of growth duration and various shapes (planar projections) of nanoparticles were observed such as 21% pentagonal, 35% quadrilateral, and 6% triangular. Furthermore, the average area of a nanoparticle (Figure 3.16E) on the CNTs surface increased by ~ 17 fold from 15 min growth duration to 10 hrs growth duration. This average area estimation is also a better indicator of size increase of nanoparticles with increasing growth duration because of the evolution of different nanoparticle shapes.

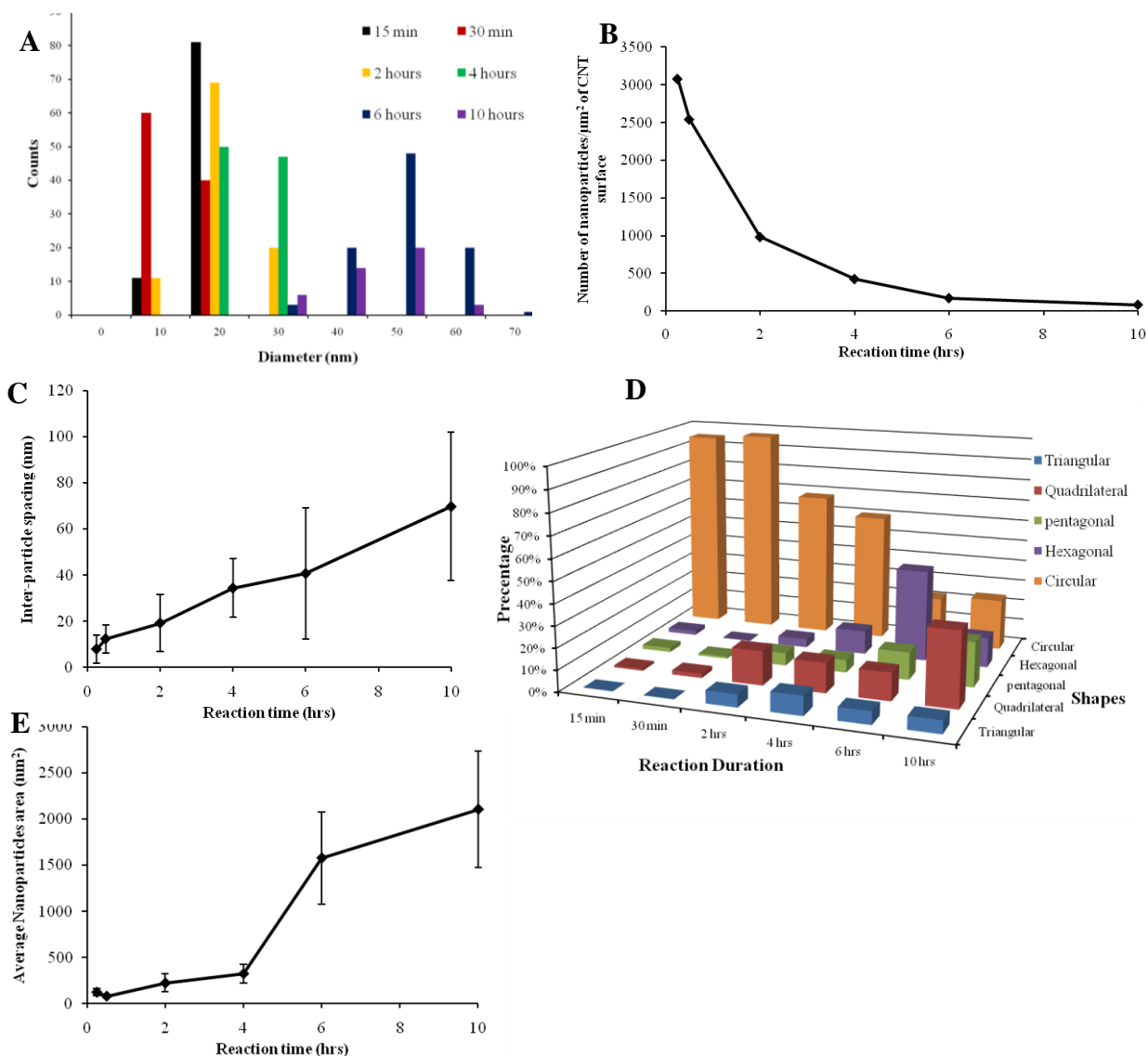


Figure 3.16 Detailed analysis of Ni/NiO core/shell nanoparticles formation on CNTs surface as a function of growth time. (A) Diameter distribution, (B) Spatial distribution (number of nanoparticles/ μm^2), (C) Inter-particle spacing, (D) 3-D plot showing morphological evolution as well as percentages of different shapes evolved, (E) Average nanoparticle projection area. Note: All the data analysis presented in this figure is for nanoparticles on the CNTs surface. More than 100 nanoparticles per sample were considered for nanoparticle area estimation and this includes all the shapes for the respective samples.

Table 2 Average diameter or size of Ni nanoparticles on the CNTs surface as a function of reaction duration.

Growth duration for heterostructures	Average size (or diameter in case of spherical nanoparticles)
15 min	12.5±2.1 nm
30 min	10.1±0.5 nm
2 hour	16.9±2.7 nm
4 hour	20.3±1.0 nm
6 hour	44.8±4.2 nm
10 hour	51.8±9.8 nm

All the observations (Figure 3.16) indicate the role of several competing mechanisms and factors involved during the formation of CNC heterostructures and these include surface tension forces, nickel content on CNTs, and decomposition of stabilizers as a function of reaction time. The observation of shape evolution of Ni nanoparticles as a function of reaction time is attributed to the rupture of stabilizer (TOPO and TOP) micelles as the reaction continued above the flash point of the stabilizers.⁷⁵ Thus, a similar mechanism for the shape evolution of Ni nanoparticles on the CNTs surface was observed here. For solution-based growth without CNTs, the shape evolution of Ni nanoparticles was also initiated beyond 2 hrs as reported here for CNC heterostructures.⁷⁵ This further proves that the shape evolution duration was independent of the type of nucleation site (i.e., with or without CNTs) and depended entirely on the rupture of the stabilizer micelle as the reaction continued with time. However, having high surface-to-volume ratio CNTs as nucleating substrate/site allowed for greater loading of Ni-oleylamine complex (Ni content).⁷⁵ Thus as the stabilizer micelle ruptured, the growing nanoparticles encountered greater local concentration of Ni and grew in size (Figure 3.16A). However, this was not observed in the case when there were no CNTs present in the synthesizing solution.⁷⁵ Another effect of the longer reaction time proposed here is based on the surface tension forces on CNTs. The rupturing of stabilizer micelle⁷⁵ with increased growth duration led to the elimination of stabilizer not only from the growing nanoparticles but also from the CNTs surface exposed to the solution. However, the bulk concentration of the stabilizers in the surrounding solution was still relatively high but slightly lower in density due to the surfactant loss. This led to high surface tension forces with increasing reaction time and thus separated the growing particles (minimizing their contact with the CNTs surface) and ultimately increasing the inter-particle spacing and lowering the spatial density of the nanoparticles on CNTs surface.

In order to explain the growth kinetics of nickel nanoparticles on CNTs, different theories were applied to fit experimental data. It has been reported that nanoparticles growth capped with stabilizers is governed by diffusion-limited growth, Lifshitz-Slyozov-Wagner (LSW) theory. Assume that the average radius of nanoparticles is r and diffusion coefficient is D , the flux of reactants, J could be written as:

$$J=4\pi r^2 D \frac{dC}{dx} \quad (3-1)$$

$$Jx^2 dx=4\pi D dC \quad (3-2)$$

Integrate on both sides and assume the bulk concentration of reactants, concentration of reactants at interface, and solubility of a nanoparticle with a radius of r are C_b , C_i , and C_r , respectively.

$$J=4\pi D r(r+\delta)(C_b-C_i)/\delta \quad (3-3)$$

where δ is the thickness of the diffusion layer.

This flux is equal to the consumption rate at the surface of nanoparticles.

$$J=4\pi r^2 k_d(C_i-C_r) \quad (3-4)$$

k_d is the rate constant of a simple first order deposition reaction.

Now consider

$$dr/dt=JV_m/4\pi r^2 \quad (3-5)$$

Thus

$$\frac{dr}{dt} = \frac{\frac{D}{r} \left(1 + \frac{r}{\delta}\right) V_m (C_b - C_r)}{1 + \frac{D}{k_d r \left(1 + \frac{r}{\delta}\right)}} \quad (3-6)$$

The terms C_b and C_r are related to the particle radius. According to Gibbs-Thompson equation:

$$C_r = C_\infty \exp\left(\frac{2\sigma V_m}{rRT}\right) \approx C_\infty \left(1 + \frac{2\sigma V_m}{rRT}\right) \quad (3-7)$$

$$C_b = C_\infty \exp\left(\frac{2\sigma V_m}{r_b RT}\right) \approx C_\infty \left(1 + \frac{2\sigma V_m}{r_b RT}\right) \quad (3-8)$$

Since the diffusion layer thickness is much greater than the size of nanoparticles, $r \ll \delta$

$$\frac{dr}{dt} = \frac{2\sigma V_m^2 C_\infty}{RT \left(\frac{1}{D} + \frac{1}{k_d r}\right)} \left(\frac{r}{r_b} - 1/r^2\right) \quad (3-9)$$

For diffusion controlled growth, $D \ll k_d r$

$$\frac{dr}{dt} = \frac{2\sigma D V_m^2 C_\infty}{RT} \left(\frac{r}{r_b} - 1/r^2\right) \quad (3-10)$$

$$\frac{dr}{dt} = \frac{K}{r^2} \quad (3-11)$$

After integration, it was found that volume of nanoparticles is proportional to growth time.⁷⁷

$$r^3 - r_0^3 = Kt \quad (3-12)$$

where r_0 is the average radius of the particle at time $t = 0$. K is given by the expression

$$K = \frac{8\sigma D V_m^2 C_\infty}{9RT} \quad (3-13)$$

where σ is the interfacial energy, V_m is the molar volume, C_∞ is the concentration of a flat particles, D is the diffusion constant of the system, R is the gas constant and T is the temperature.

It was found that for nanoparticles synthesized at 10 hrs, it could not be fitted into LSW theory. Only nanoparticles grown at less than 4 hrs will be fitted as shown in figure 1B, where the R^2 coefficient is around 0.97 and K is 3.9282. Compared with nanoparticles synthesized without CNTs, where size of nanoparticles remained the same after several hours, it could be

conclude that after 4 hrs, the increase of nanoparticles size could be resulted from Ostwald ripening.

The remaining data was then fitted according to two stages Ostwald ripening:⁷⁸

$$D-D_1=k(t-t_1)^{1/n} \quad (3-14)$$

where t is reaction time, t_1 is the starting time, k is a temperature-dependent material constant appropriate to the value of the exponent n , and D_1 is the average particle diameter at $t=t_1$. When the exponent n is equal to 2, it is inferred that crystal growth is controlled by the diffusion of ions along the solution-particle boundary; when $n=3$, the growth is controlled by the volume diffusion of ions in the solution; and when $n=4$, it is deduced that growth is controlled by dissolution kinetics at the solution-matrix interface. From LSW theory, it is reasonable to assume that Ostwald ripening start at around 4 hrs and D_1 is 20.3 nm. In order to determine the controlled step, different exponent n (from 2 to 4) were selected. The R^2 coefficient was plotted against exponent n . It clearly demonstrated that $n=3.8$ is the best fitting. Thus, Ostwald ripening at this stage controlled by both the volume diffusion of ions and dissolution kinetics at the solution-nanoparticles interface.

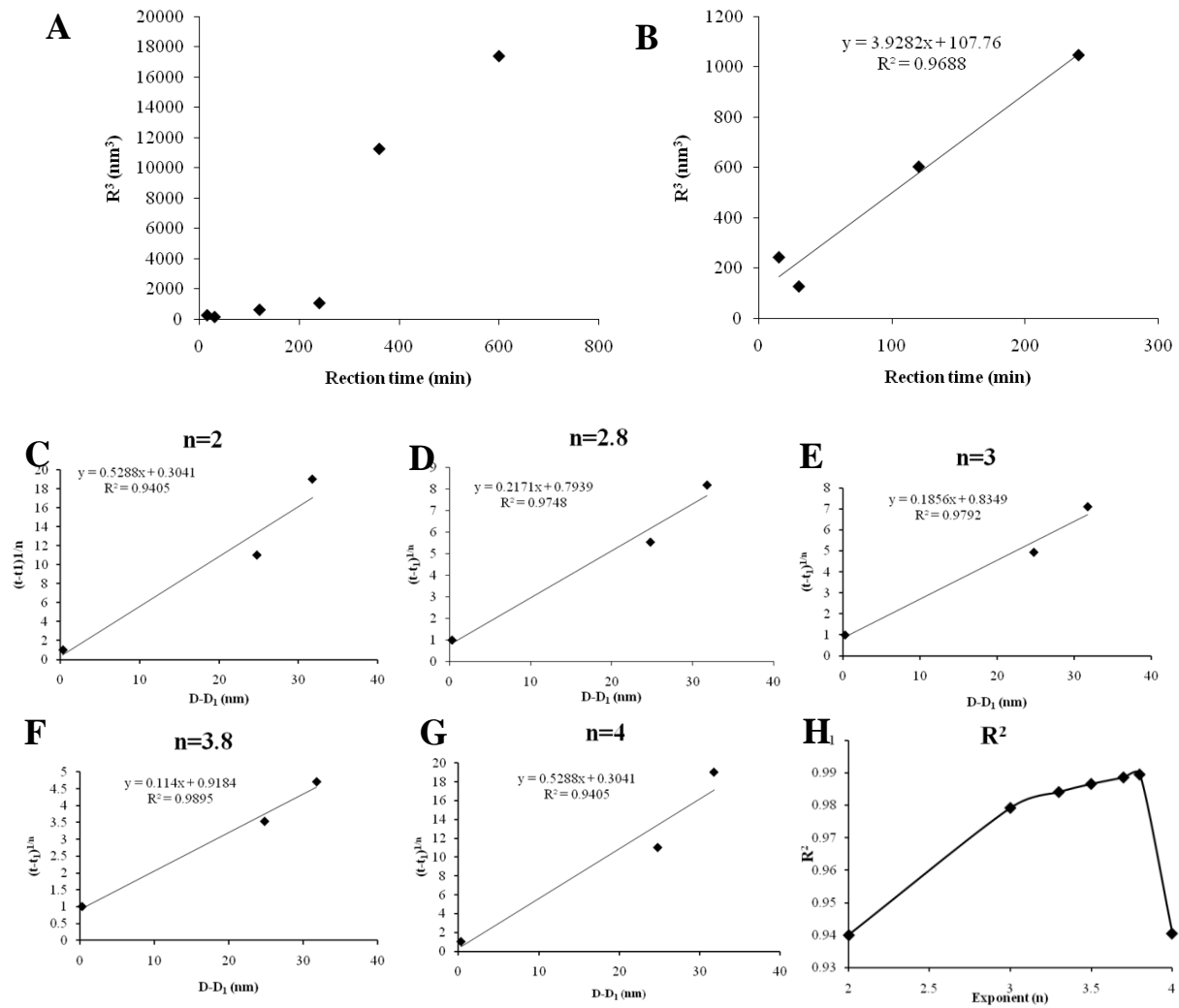


Figure 3.17 (A) Plot of volume of nanoparticle to reaction time. (B) Linear fitting of volume of nanoparticles to reaction time at the first 6 hrs. (C), (D) (E), (F), and (G) Fitting of two stage Ostwald ripening at different exponent. (H) Plot of R^2 coefficient to different component.

Another interesting observation for CNC heterostructures, irrespective of the growth duration, was the bending of graphene layers or defective CNTs walls in the space between two adjacent nanoparticles (Figure 3.18). As shown in Figure 3.18G, the average inter-wall spacing changed from ~ 0.35 nm to ~ 0.38 nm in these regions. Radius of curvature of approximately ~ 4.22 nm developed for the bent sections of the graphene layers. However, this was only observed when the adjacent nanoparticles were nucleated with perfect packing or less than 2 – 3 nm apart as shown on the edges of the CNTs walls (Figure 3.18). Thus, nanoparticles with significant spacing between them (Figure 3.15J) did not result in bending of CNTs walls. Such an observation has not been reported before and the authors propose that this could be due to the oxide shell formation, lattice incompatibility between nanoparticles and the CNTs, and the flexibility of graphene layers in the CNTs walls.⁷⁹ The former is indeed the dominating mechanism of CNTs wall bending because the polycrystalline NiO shell and the core Ni nanoparticle had a very large lattice mismatch ($>15\%$) as shown in Table 3. This lattice mismatch could have led to compressive strains in the NiO shell and as this polycrystalline shell tends to relax, it pinched or bent the contacting graphene layers in the CNTs walls. Such stress relaxation mechanism has been reported⁸⁰ for Ni/NiO core/shell nanoparticles and resulted in hillock formation in the oxide shell that has also been observed in our study (Figure 3.18F). In addition, the inner section of the bent portion of the flexible CNTs wall is in a state of compression and as the lattice spacing increased on the outer side, it resulted in a state of tension. Another theory for the bending is due to the interaction between nanoparticles and CNTs. As shown from XPS that after decoration of nanoparticles, π - π^* transition disappeared, which tells us the strong interaction between CNTs and nanoparticles. This strong interaction could result in charge polarization and Van der Waals force, which causes the bending of graphene shell.

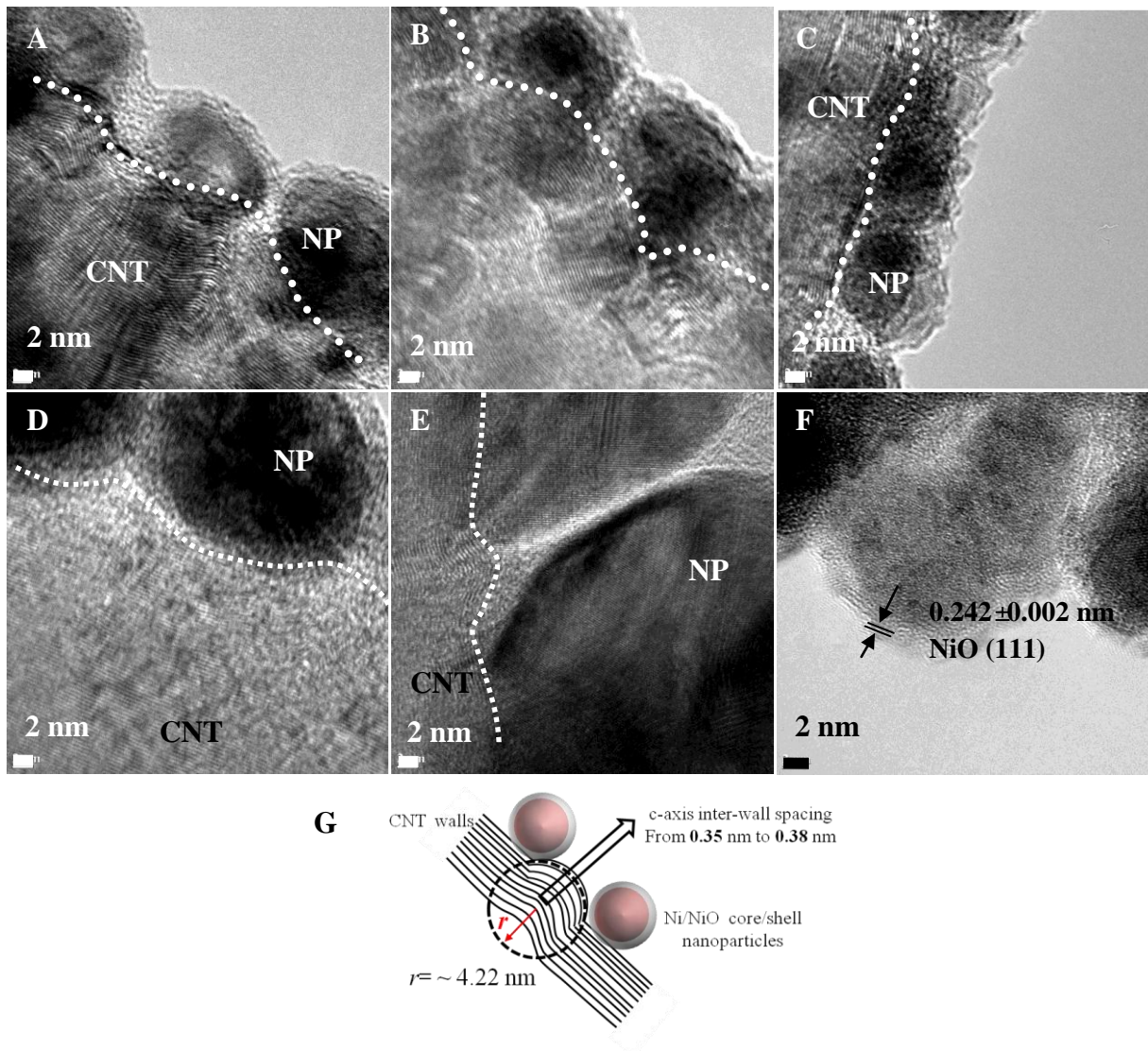


Figure 3.18 High resolution TEM images of CNC heterostructures corresponding to the nanoparticle growth time of (A) and (B) 15 min, (C) 30 min, (D) 4 hrs, and (E) 6 hrs. The dotted lines indicate the bending of the graphene layers (or CNTs walls) between nanoparticles. (F) Lattice spacing of polycrystalline oxide shell. (G) Schematic showing bending of CNTs walls (radius of curvature is r) and increase in inter-wall spacing as a function of wall thickness between the adjacent nanoparticles.

Table 3 Lattice mismatch between the core Ni nanoparticle and the polycrystalline NiO shell as observed using TEM and XRD. Note: XRD shows all the crystal planes for the individual component.

Nickel	Spacing	Nickel Oxide	Spacing	Lattice mismatch (%)
(111)	0.203	(111)	0.241	15.77
		(220)	0.148	37.16
(200)	0.176	(111)	0.241	26.97
		(220)	0.148	18.92
(220)	0.124	(111)	0.241	48.55
		(220)	0.148	16.22

To confirm the presence of individual phases and materials in the multi-component CNC heterostructures, XRD analysis (Figure 3.19) was performed for samples grown for different durations. It was observed that for growth durations ranging from 15 min to 10 hrs (Figure 3.19 a-f), Ni, NiO, and CNTs peaks were observed. Very low intensity XRD peaks for CNTs in samples could be attributed to the limitations of the XRD instrument, less amount of sample dispersed on the substrate, larger size or tight packing of the coated nanoparticles, and the presence of remaining oleylamine and stabilizers. It is known that the washing process after the synthesis of heterostructures does not completely eliminate the stabilizers from the surface of these heterostructures. On the other hand, TEM and SEM results (Figure 3.14 and Figure 3.15) clearly prove that CNTs were always present in all the samples and were coated with nanoparticles with respective spatial densities and morphologies (Figure 3.15). Furthermore, high resolution TEM (Figure 3.15D) and XRD (Figure 3.19e) shows the presence of a few nanoparticles with hcp Ni core. However, fcc Ni was the dominant crystal structure of the core nanoparticles present in these heterostructures.

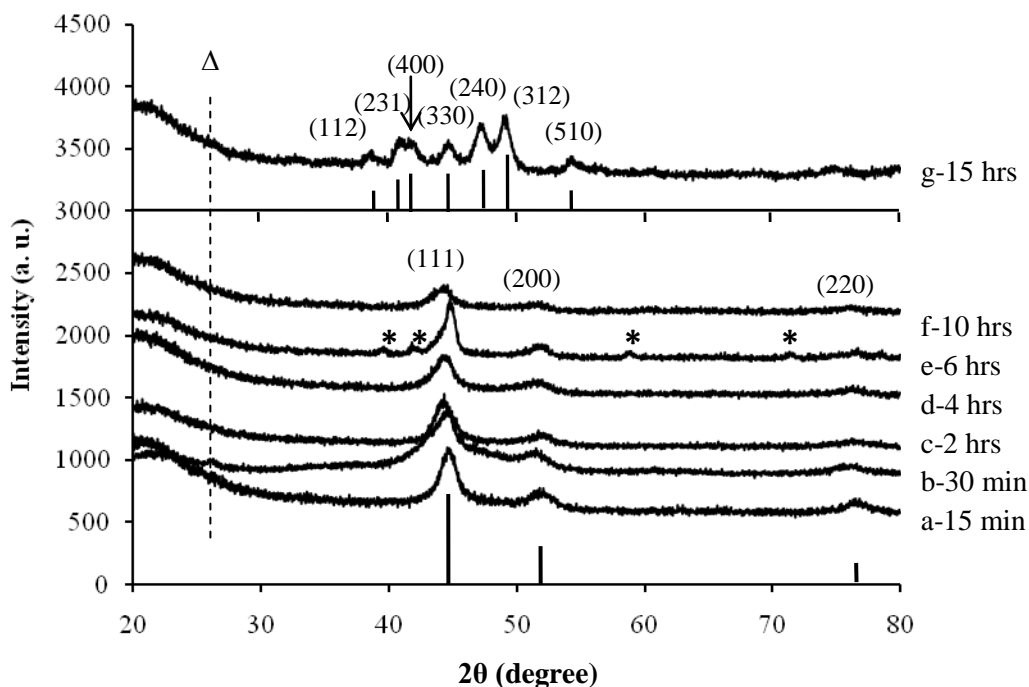


Figure 3.19 XRD of (a-f) CNC heterostructures showing the peaks of Ni (JCPDS No.4-0850), NiO (JCPDS No. 4-835) corresponding to the Ni/NiO core/shell nanoparticles, and (g) CNTs coated with Ni₁₂P₅ nanoparticles (JCPDS No. 74-1381). Note: A low intensity peak (Δ or dotted line) is also observed around $\sim 26^\circ$ corresponding to c-axis spacing of graphene layers in CNTs. (*) indicates hcp Ni (JCPDS No. 45-1027) and the corresponding planes (left to right are (010), (002), (012), and (110)).

Interestingly, a new set of XRD peaks emerged for 15 hrs growth duration (Figure 3.18g), where none of the peaks corresponded to Ni and NiO but only to Ni₁₂P₅. Thus, the growth duration of 15 hrs led to phosphide nanoparticle formation or CNT-nickel phosphide nanoparticle heterostructures. This motivated us to do a detailed microscopic characterization of samples grown for 15 hrs (Figure 3.20). The average diameter (Figure 3.21A) of the nanoparticles on the CNTs surface was observed to be $\sim 11.1 \pm 1.8$ nm and $\sim 26.6\%$ of the nanoparticles exhibited hollow cores (Figure 3.20A and arrows in Figure 3.20C) with average shell thickness of $\sim 2.9 \pm 0.4$ nm. These nanoparticles were nearly uniformly coated (spatial density $\sim 2170 / \mu\text{m}^2$ and inter-particle spacing ~ 13.08 nm) on the CNT surface (Figure 3.20A-D) and several micrometer-sized irregular nanoparticles were also observed in SEM (Figure 3.14B) and TEM (Figure 3.20E). In addition, high-resolution TEM image (Figure 3.20D) clearly shows the lattice spacing of ~ 0.207 nm corresponding to (330) planes of Ni₁₂P₅ (JCPDS No. 74-1381). In regard to the shape distribution (Figure 3.21B) of the nanoparticles on CNTs surface, it was observed that $\sim 77.2\%$ of nanoparticles were spherical (or circular projection area) and the remaining were other shapes such as hexagonal ($\sim 7.5\%$), pentagonal ($\sim 8.8\%$), quadrilateral ($\sim 2.5\%$), and triangular ($\sim 3.7\%$).

Based on the above characterization studies and analysis, the following mechanism for the formation of phosphide nanoparticles on CNTs has been proposed here. As the stabilizer micelle already ruptured in the 15 hrs growth duration, the phosphide nanoparticle formation could be attributed to the reaction between phosphine-based stabilizers (TOPO and TOP) that are in the bulk of the surrounding solution and the growing Ni nanoparticles.^{81,82} The difference between the sizes of phosphide nanoparticles nucleated on the CNTs surface as compared to micrometer-sized particles dispersed in the same solution can be attributed to the Ostwald's

ripening effect for 15 hrs growth duration, that became the dominant nanoparticle growth mechanism as most of the stabilizer micelle ruptured.⁸³ Due to this effect, as soon as the phosphide nanoparticle formation took place, the larger particles started growing at the expense of smaller ones and thus reduced the size of nanoparticles on the CNTs surface. These micrometer-sized particles must have grown independently in the synthesis solution or maybe initially nucleated on the CNTs surface but eventually (in 15 hrs) detached themselves from the CNTs and dispersed in the solution due to their bulky size. Finally, it was also observed that there is no bending of graphene layers in CNTs walls (Figure 3.20F), in spite of several locations having closely packed phosphide nanoparticles. This further confirms that oxide shell formation on Ni nanoparticles (for growth duration ≤ 10 hrs) was the key in bending of graphene layers in the CNTs walls as stated earlier in this report.

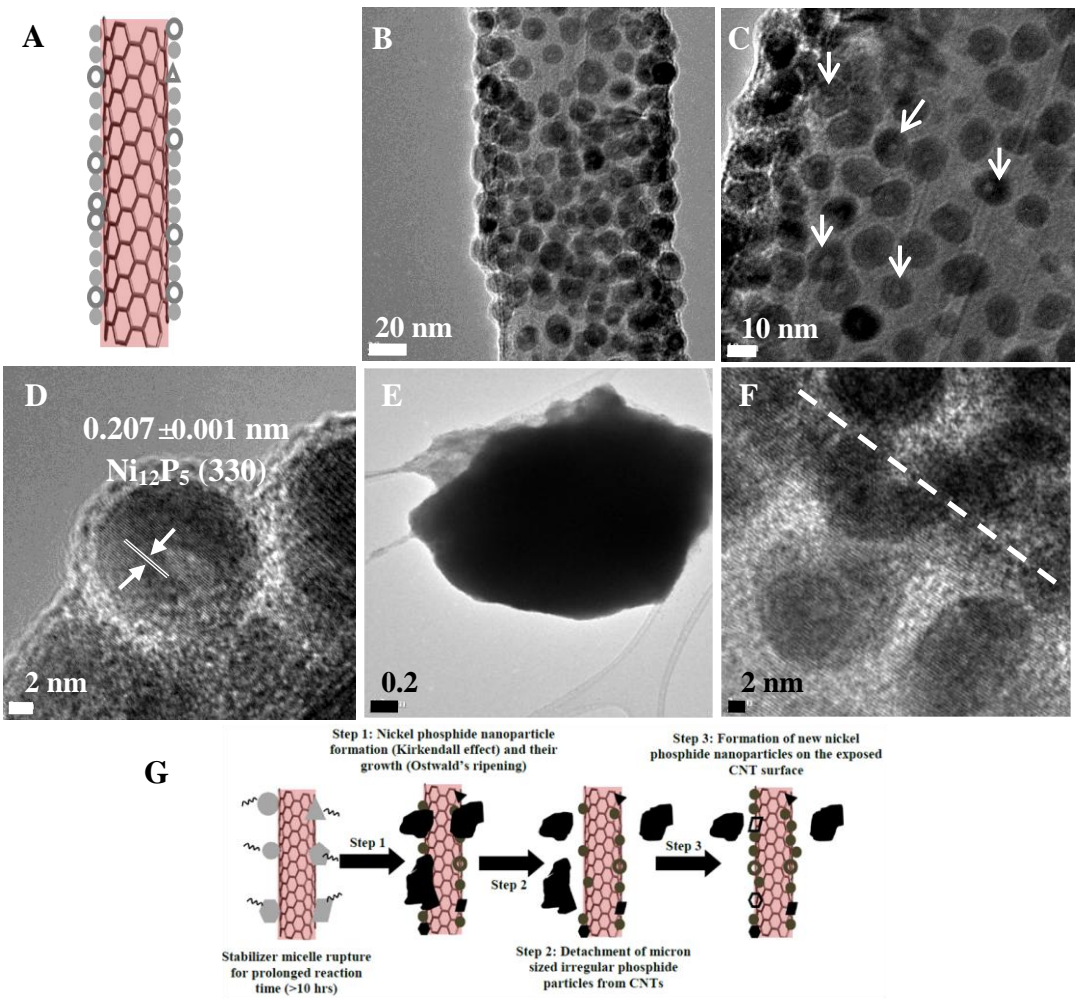


Figure 3.20 Hollow and solid Ni_{12}P_5 nanoparticles formed on CNTs (Schematic in A) after 15 hrs. (B) and (C) High-resolution TEM images shows numerous nanoparticles that are hollow (indicated by arrows in C) and with different shapes. (D) High-resolution TEM image shows the lattice spacing and the corresponding plane. (E) TEM image shows large-sized irregular Ni_{12}P_5 particle observed for 15 hrs. These particles are isolated and do not form on the CNTs surface. (F) No bending of CNTs walls between adjacent nanoparticles is observed for these heterostructures. (G) Schematic shows proposed growth mechanism and formation of CNT-nickel phosphide nanoparticle heterostructures.

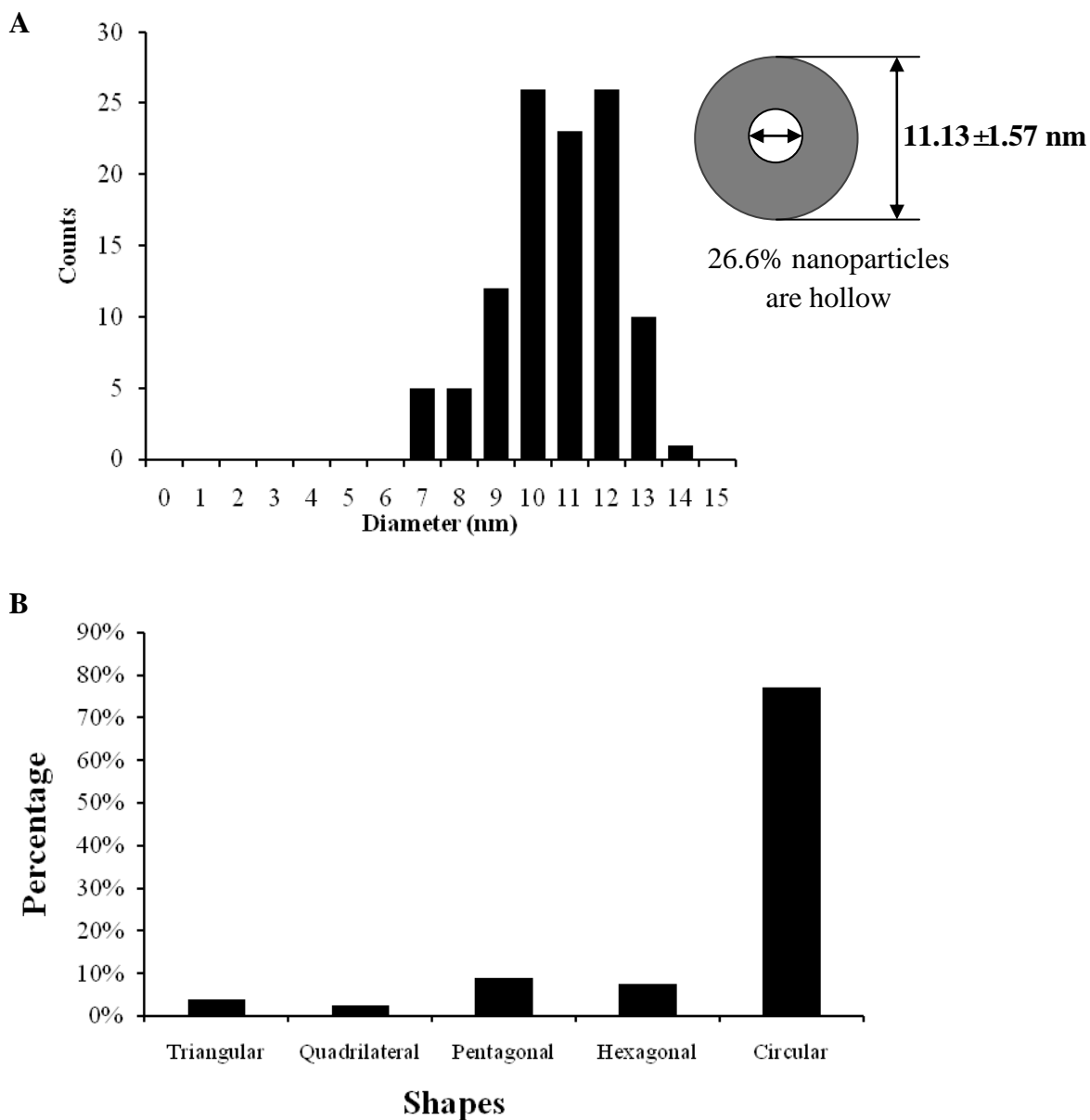


Figure 3.21 (A) Size distribution of Ni_{12}P_5 nanoparticles on the CNTs surface. The average diameter of the nanoparticles was observed to be $\sim 11.1 \pm 1.8$ nm. The schematic in (A) shows the dimensions of nanoparticles that were hollow had a shell thickness of $\sim 2.85 \pm 0.42$ nm. Approximately $\sim 26.6\%$ of nanoparticles were hollow. (B) Shape distribution of Ni_{12}P_5 nanoparticles on the CNTs surface.

3.4 Synthesis and Characterization of Composite Hydrogel

Freeze-thawing approach was utilized to synthesize PVA hydrogel without chemical cross-linking (Figure 3.22A, dotted rectangle in left). This resulted in crystalline domains in the polymer network that makes PVA hydrogel insoluble in water. Using similar approach, CNC heterostructures were mixed in the PVA solution and then freeze-thawed for two cycles resulting in CNC heterostructure-PVA hydrogel (Figure 3.22A, right). Transparency of the pure PVA hydrogel is significantly lost by adding CNC heterostructures to it. The dark color of the CNC heterostructure-PVA hydrogel also indicates the uniformity of dispersion of the heterostructures inside the hydrogel. The transmittance spectra showed $\sim 30\%$ transmittance in the visible region for CNC heterostructure-PVA hydrogel and $\sim 90\%$ transmittance for PVA hydrogel (inset, Figure 3.22A). Figure 3.22B and C shows SEM images for both the hydrogels in shrunken state. Inset in Figure 3.22C indicates CNTs emanating out of ruptured CNC heterostructure-PVA hydrogel. TEM characterization of these hydrogels was not possible due to the high electron beam intensity and temperature leading to burning of the polymer film.

The synthesized hydrogels with and without CNC heterostructures showed good swelling and shrinking characteristics indicated by EWC in DI water (Figure 3.22D). Irrespective of whether the CNC heterostructures were or were not incorporated in the PVA hydrogel, swelling of the hydrogel in the presence of water reached saturation within 1 hr (Figure 3.22D). Compared to pure PVA hydrogel (EWC $\sim 75\%$), the CNC heterostructure-PVA hydrogel exhibited slightly lower EWC after saturation ($\sim 73\%$). Although the transmittance of the hydrogel was significantly reduced, the slightly lower EWC indicates minimal effect on the porosity/pore volume of the PVA hydrogel after incorporating CNC heterostructures.

The PVA used in this study is 99+% degree of hydrolysis with a few acetate groups. In order to understand the functional groups of PVA hydrogel and CNC heterostructure-PVA hydrogel, FTIR spectra (Figure 3.23) were recorded. Figure 3.23A(a) shows the FTIR spectrum of pure PVA with C–H alkyl stretching band ($\nu = 2850\text{-}3000\text{ cm}^{-1}$) as well as weak hydroxyl (-OH) for free alcohol (non-bonded –OH stretching) and hydrogen bonded band ($\nu = 3100\text{-}3650\text{ cm}^{-1}$). Due to the hydrophilic nature of PVA hydrogel, intramolecular and intermolecular hydrogen bonding were expected to occur among PVA chains. The peaks observed between $1650\text{-}1750\text{ cm}^{-1}$ corresponded to C=O stretching due to the small amount of acetate groups. The peaks between $1085\text{ and }1150\text{ cm}^{-1}$ corresponded to C-O-C stretches in PVA and CH₂ groups are showed by peaks at $1410\text{-}1465\text{ cm}^{-1}$. The former region also indicates the presence of crystalline domains in the PVA (indicated by a shoulder around 1140 cm^{-1}).

Incorporating CNC heterostructures in PVA hydrogel resulted in multi-component system and thus FTIR study was critical. As shown in Figure 3.23A(b), peaks corresponding to PVA could be easily identified. The peaks around $2929\text{ and }2876\text{ cm}^{-1}$ corresponded to CH₂ stretching of TOP (adsorbed stabilizer) that was used during CNC heterostructure preparation (Figure 3.23B(b)). In addition, C–P stretching peaks (Figure 3.23C(b)) of TOP were also observed at $1170, 1076, \text{ and }1032\text{ cm}^{-1}$. The peak at 728 cm^{-1} related with (–CH₂) stretches of TOP was also observed (Figure 3.23C(b)). Moreover, peaks at $1494, 1456, \text{ and }1381\text{ cm}^{-1}$ originated from the asymmetric in-plane and symmetric rocking mode of terminal methyl group of TOP (Figure 3.23C(b)). Oleylamine is also involved in the synthesis of CNC heterostructures and thus, weak NH₂ bending modes at $909, 964, \text{ and }993\text{ cm}^{-1}$ and NH₂ scissor mode at 1568 cm^{-1} (Figure 3.23C(b)). The peak at 1042 cm^{-1} could also be due to the C–N stretch due to the C–N bonds in amine groups indicating unwashed oleylamine on CNC heterostructures. The

peak at 1468 cm^{-1} is associated with the C–H bending mode and the two peaks at 2865 and 2921 cm^{-1} represented C–H stretching modes of the oleylamine carbon chain (Figure 3.23B and C(b)). The presence of various N–H peaks suggests that amines are adsorbed on the surface of the nickel nanoparticles. The FTIR spectra also showed the stretching modes of alkyl chains and P–O at $2800\text{--}3000$ and 1085 cm^{-1} , respectively, revealing that the TOPO was also adsorbed (Figure 3.23B and C, (b)) on the surface of NiO shell in CNC heterostructure.

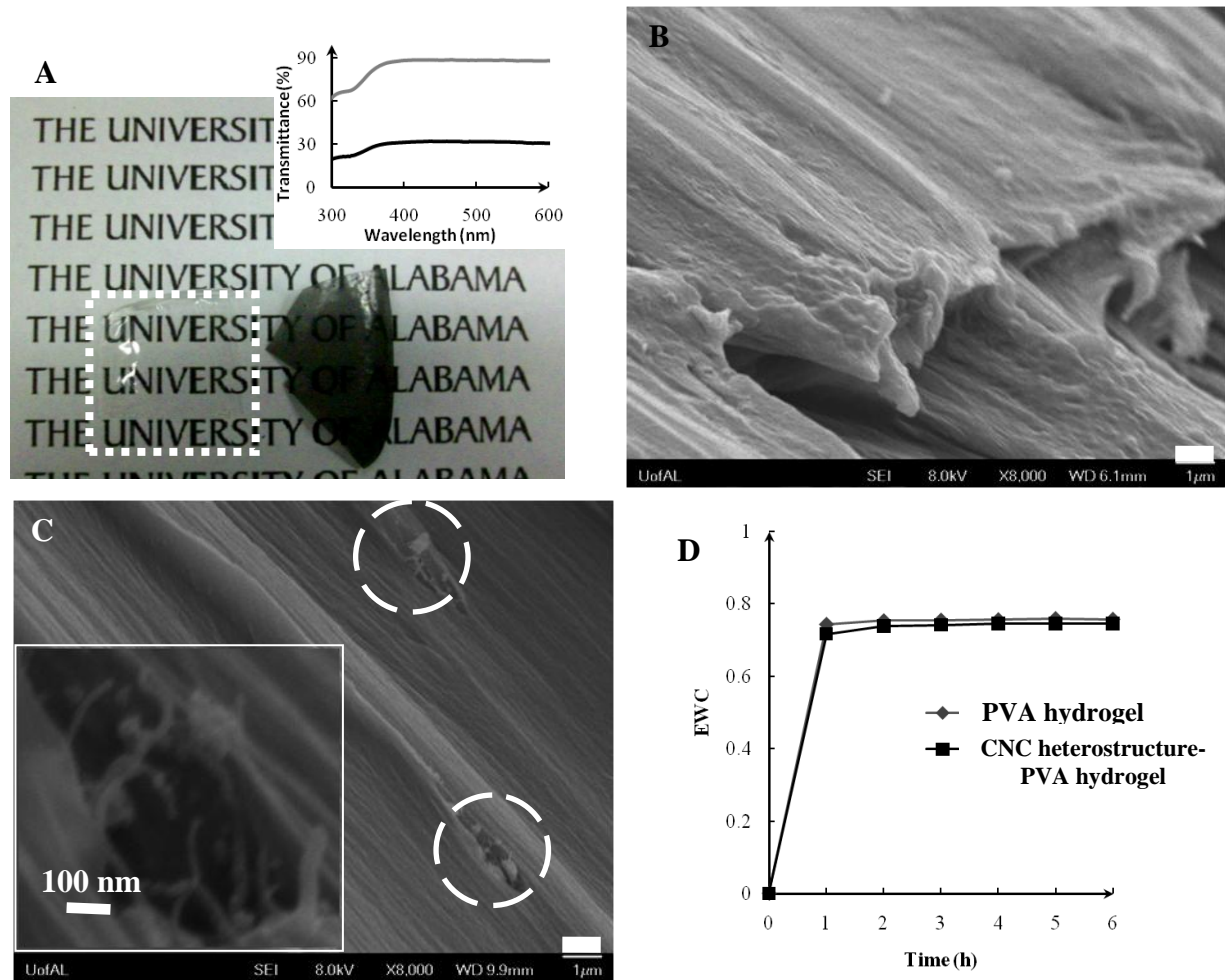


Figure 3.22 (A) Digital image of PVA hydrogel (left, dotted rectangle) and CNC heterostructure-PVA hydrogel. Inset shows the transmittance spectrum in visible range for both hydrogels. (B) EWC graph of both PVA and PVA-CNT/Ni hydrogel. (C) SEM image of PVA hydrogel (scale bar: 1 μm). (D) SEM image of PVA-CNT/Ni hydrogel (scale bar: 1 μm) and inset shows high magnification of CNT/Ni inside hydrogel.

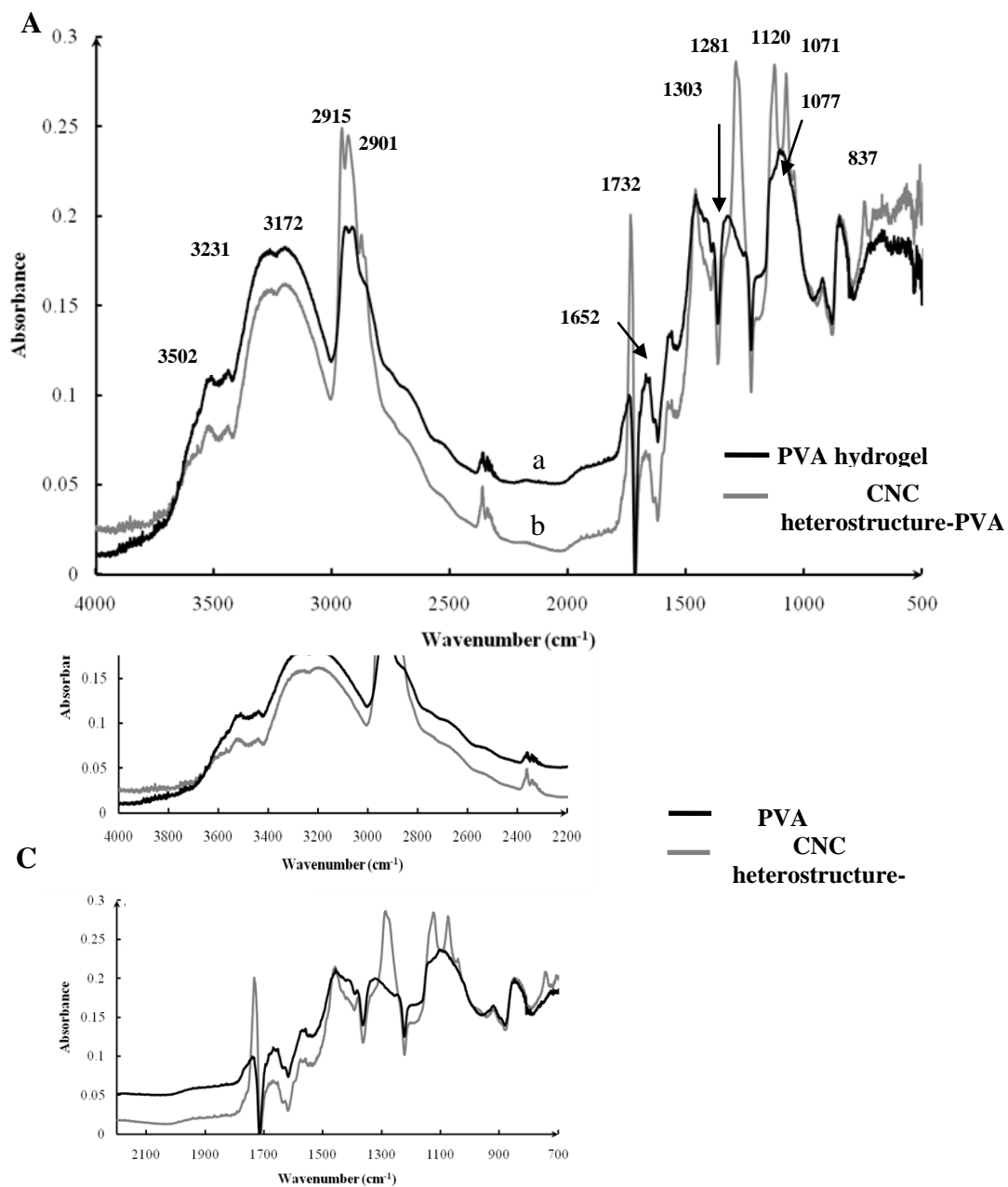


Figure 3.23 (A) Full range ($500\text{-}4000\text{ cm}^{-1}$) FT-IR spectra of PVA hydrogel and CNC heterostructure-PVA hydrogel. (B) and (C) Magnified region of FTIR spectra showing different peaks for PVA hydrogel and CNC heterostructure-PVA hydrogel.

3.5 Absorption and Concentration Ability of Composite Hydrogel

PVA hydrogels have been of significant interest for biomedical devices.^{84,85} However, multi-functionality of the hydrogel remains a big challenge. The integration of nanostructures within PVA hydrogels can influence the functionality as well as the selectivity of the individual components in such a hybrid materials.⁸⁶ In this regard, each of the two hydrogels (PVA and CNC heterostructure-PVA) in this study was immersed in different solutions containing one or more chemical species. This caused sudden swelling of hydrogel in the solution resulting in entrapment or rejection of molecules present in the solutions. Unique to this study is the reversal of the functionality of the Ni/NiO core/shell nanoparticles in the CNC heterostructure-PVA hydrogel. Ni/NiO core/shell nanoparticles have strong affinity for histidine-tagged molecules.⁶⁸ Even though these nanoparticles have small amount of adsorbed stabilizers after rigorous washing, still they have shown significant affinity for histidine. However, instead of entrapment of such molecules, it was observed that CNC heterostructure-PVA hydrogel concentrated/rejected them in the solution. Control sample (PVA hydrogel) and CNC heterostructure-PVA hydrogel were studied for concentrating L-histidine and histidine-tagged GFP. In addition, it was demonstrated that a dye molecule (model molecule: methyl orange), not having any affinity for CNC heterostructure-PVA hydrogel, could be easily separated from a solution containing L-histidine and methyl orange. All these molecules have comparable size ($\sim 0.8\text{-}1\text{ nm}$)^{87,88} and can be characterized using UV-vis spectroscopy with distinct absorbance at 263 nm (GFP), 465 nm (methyl orange), and 210 nm (L-histidine).

It was observed that methyl orange concentration (Figure 3.24A) decreased in the solution with PVA hydrogel or CNC heterostructure-PVA hydrogel immersed in it. This indicates that both hydrogels easily absorb methyl orange and do not show any selectivity toward

it. Also consistent with the EWC results, the methyl orange absorption was lower in CNC heterostructure-PVA hydrogel as compared to the PVA hydrogel. In addition, the curve is steep for the first 20 min (Figure 3.24A) of methyl orange absorption in the hydrogels, which is due to the swelling of hydrogel leading to the initial burst. A series of similar experiments were performed for solutions containing histidine-tagged GFP (Figure 3.24B), L-histidine (Figure 3.24C), and mixture of L-histidine and methyl orange (Figure 3.24D). It was observed that L-histidine could be concentrated in solution by immersing PVA hydrogel, which is obvious, as the hydrogel tends to absorb more water. However, this concentrating effect was enhanced when the CNC heterostructure-PVA hydrogel was immersed in the solution (Figure 3.24C). The trend in this curve shows that there was an initial burst (due to the swelling of the hydrogel) in the water absorption inside both the hydrogels (until 20 min). After 60 min, PVA hydrogel started absorbing L-histidine as indicated by the decreasing concentration of the molecules in the solution (Figure 3.24C). On the other hand, concentration of L-histidine in the solution containing CNC heterostructure-PVA hydrogel increases further. Similar trends were observed in histidine-tagged GFP solution containing PVA hydrogel or CNC heterostructure-PVA hydrogel (Figure 3.24B). The initial burst of water absorption still existed in these samples. GFP, due to its larger size as well as charge characteristics, could block the pores of the hydrogel and reduce the water absorbing capability of either hydrogel samples as compared to solution containing L-histidine. Overall, it was observed that histidine-based molecule concentrated to a greater extent for solution containing CNC heterostructure-PVA hydrogel than pure PVA hydrogel. Such a reversal of functionality of CNC heterostructures has not been observed earlier and can be very useful for separating one kind of molecule while simultaneously concentrating another molecule in a solution containing mixture of molecules. In this regard, the mixture of L-

histidine and methyl orange was studied. As observed for L-histidine (Figure 3.24C) or methyl orange (Figure 3.24A), similar trends were observed with the PVA hydrogel or CNC heterostructure-PVA hydrogel when either of these were immersed in solution containing both the molecules. CNC heterostructure-PVA hydrogel tend to absorb methyl orange but significantly concentrated L-histidine in the solution. However, the mechanism of reversal in the functionality of Ni/NiO core/shell nanoparticles, in CNC heterostructure-PVA hydrogel, for histidine-based molecules is still under investigation. This can be attributed to charge characteristics of hydrogel and boundary layers formed around incorporated CNC heterostructures when immersed in the solution containing histidine-tagged species.

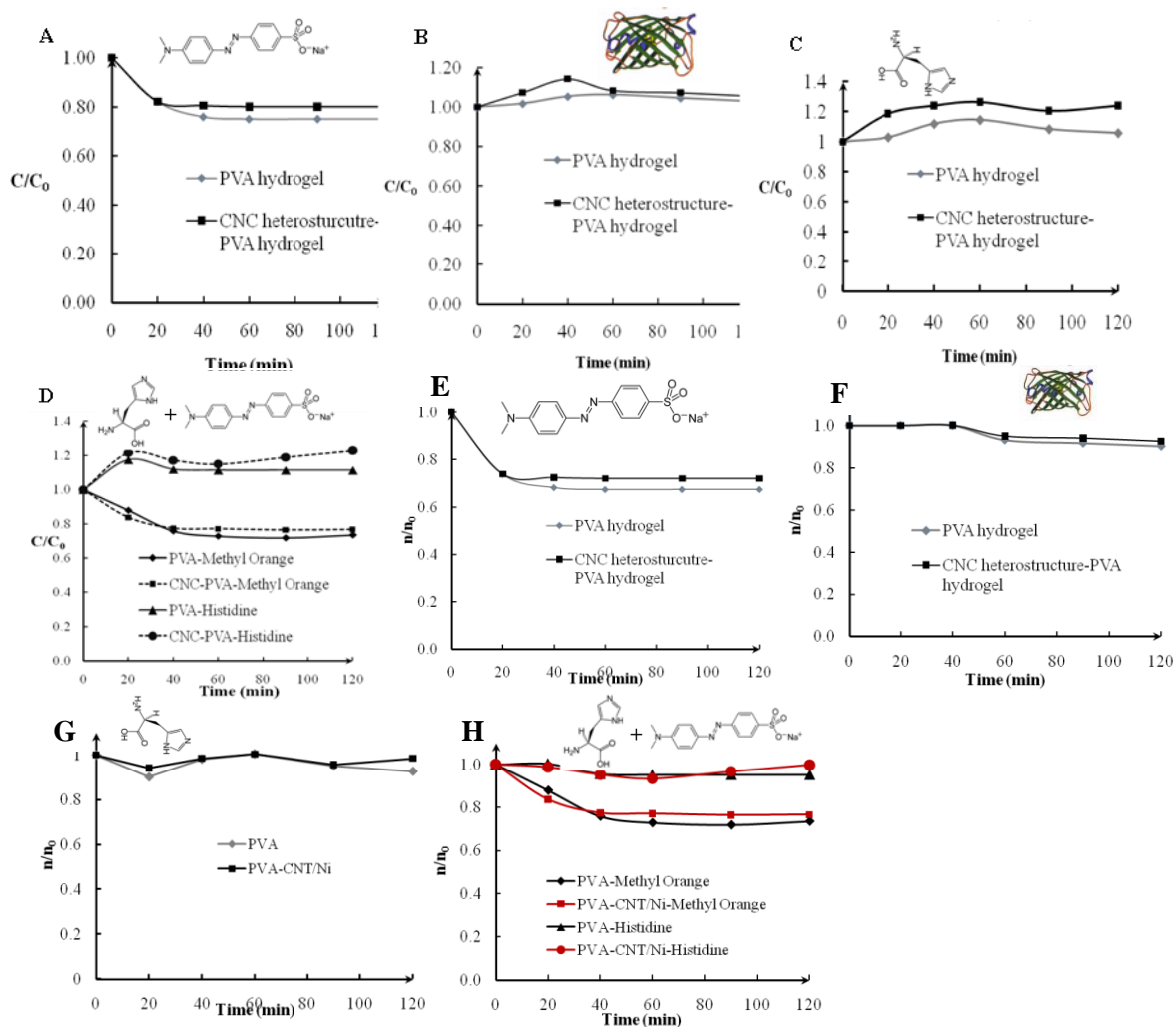


Figure 3.24 Behavior of hydrogels in different chemical environments was indicated by concentration and amount of species in solution as a function of time. (A) Absorption of methyl orange in hydrogels. (B) and (C) Concentrating histidine-tagged GFP and L-histidine. (D) Selectively concentrating L-histidine from a mixture of methyl orange and L-histidine. (E), (F), (G) and (H) Changes of total amount plotted against time.

3.6 Controlled Release with External Magnetic Field

In order to understand the properties of as-prepared CNC heterostructures, multifunctional hydrogel based on CNC and PVA was prepared. There are several advantages for this system: (1) Bio-active Nickel nanoparticles were dispersed on high surface area CNTs, which effectively avoid the aggregation problems; (2) PVA hydrogel was bio-compatible and was commonly used; (3) As-prepared CNC hydrogel is magnetic active, by rational design of the material scheme, multifunctionality could be demonstrated and efficiently utilized; (4) By dispersing CNTs inside the hydrogel, the mechanical properties of as prepared hydrogel can be also greatly enhanced.

CNC hydrogel was then tested with external magnetic field. Shrunken composite hydrogel was immersed inside DI water for ~ 30 min and then secured one-side with tape on glass slide. Then a magnet (0.2T) was placed near the hydrogel. Because of magnetic response of hydrogel, by slowly removing magnet away from hydrogel, there will be an actuated angle. It was found out that bending angle as high as 60° caused by magnetic field could be achieved by a magnet (Figure 3.25). In order to determine the effect of magnetic field for molecules releasing, hydrogels loaded with L-histidine was immersed into water to release histidine. Interestingly, external magnetic field can affect the release rate of L-histidine. With magnetic field, the final absorbance of L-histidine was 0.35, which is higher than without magnetic field (0.31, Figure 3.26B). Based on the elastic properties from hydrogel itself and incorporated CNC inside hydrogel, magnetic field with different duty cycles were also applied and the effects were showed in Figure 3.26C. By adjusting magnetic duty cycle, release rate can be further increased and the faster the change of magnetic field, the high the release rate. The possible reason is by

repeatedly varying magnetic field, the hydrogel was shrunken and swollen with certain period, and at the same time, water was absorbed and released accordingly, which can effectively accelerate the release process.

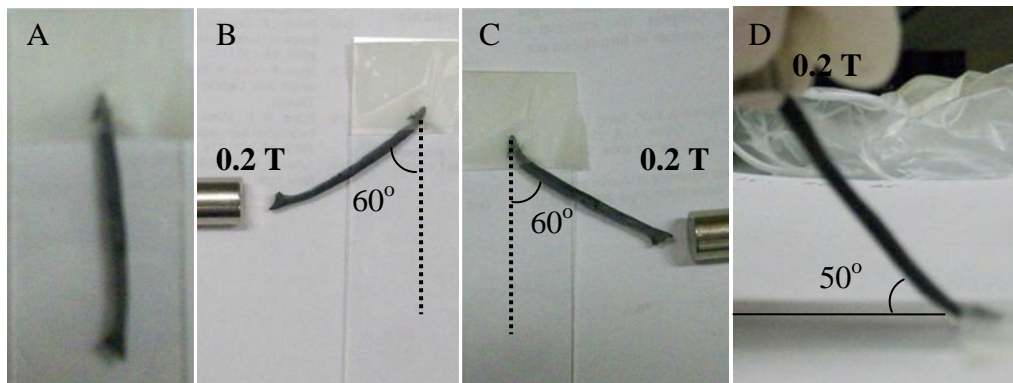


Figure 3.25 Actuation of composite hydrogel by magnet.

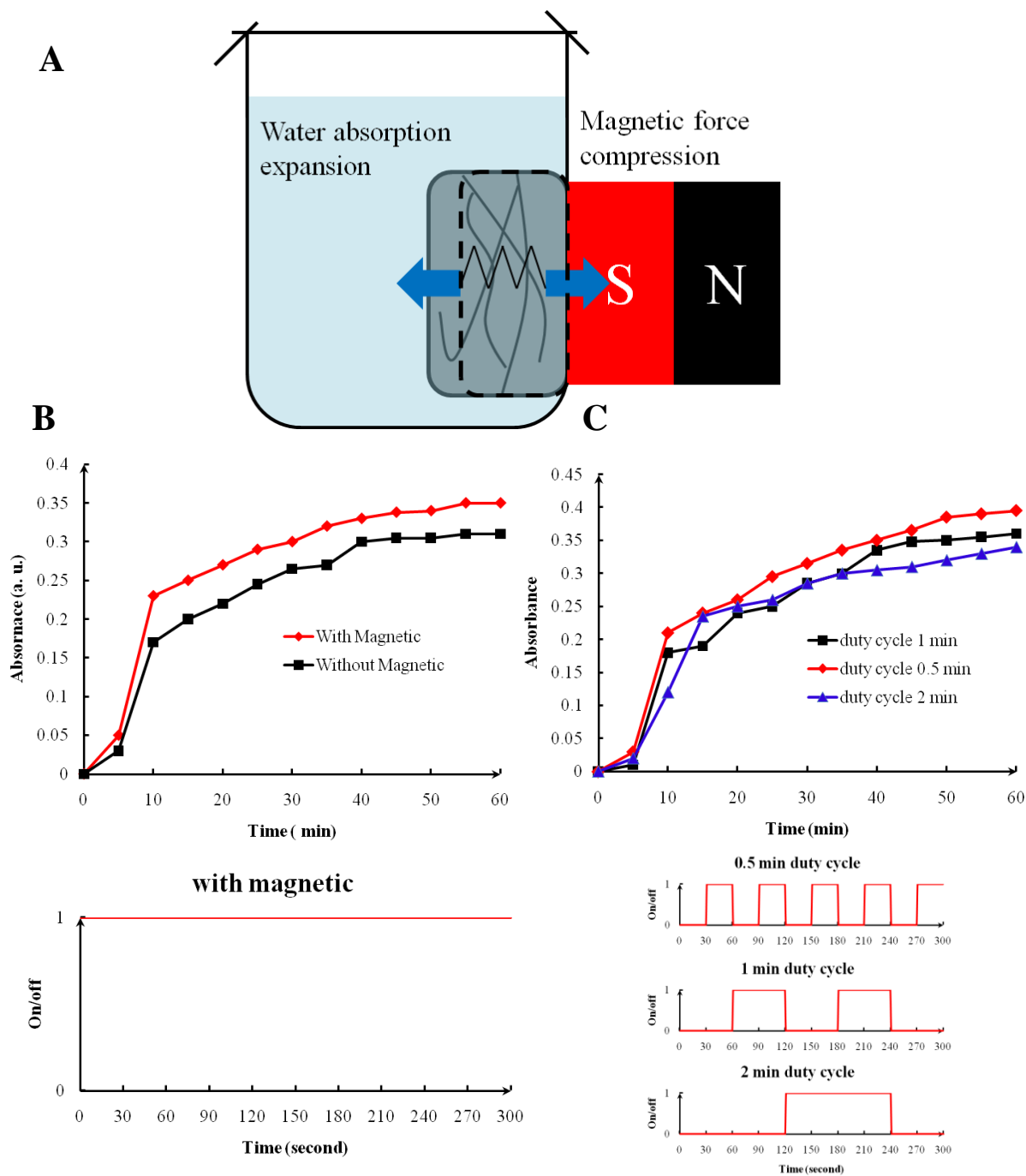


Figure 3.26 Controlled releasing of molecules with (B) constant and (C) cycled magnetic field stimulation.

3.7 Thermal Stability of CNC Heterostructures and Carbon Nanotubes

Ability to tailor morphologies of Ni/NiO core/shell nanoparticles on the CNTs surface as a function of growth duration is unique. However, it is also important to understand the stability of these heterostructures. One of the important aspects of these heterostructures and the synthetic approach presented here is the strong binding of nanoparticles with CNTs and yet not involving covalent bonding or a linker molecule. Thus, it becomes critical to study the thermal and chemical stability of these heterostructures. Our previous report demonstrated that high-power ultrasonication^{89,90} could result in controlled detachment of nanoparticles from the surface of CNTs in these heterostructures and that too in a long sonication time (> 30 min). In addition, this extremely valuable post-synthetic step allowed for the tailoring of spatial density and spacing between the coated nanoparticles. On the other hand, of particular interest for high temperature applications (e.g., catalysis, chemical sensors) of CNC heterostructures is their thermal stability. Thus, in this report, we selected the most optimized CNC heterostructure condition (30 min growth) that resulted in uniform nanoparticle coating on CNTs with majority being spherical nanoparticles. Thermal stability was analyzed by annealing CNC heterostructures at 125 °C, 200 °C, 400 °C, 600 °C, and 750 °C in a N₂-rich atmosphere. The N₂-rich atmosphere implies that the box furnace was not leak proof and a small amount of O₂ (from ambient) was inevitable in the annealing process. In contrast to high percentage O₂ environments or air, such an annealing atmosphere was deliberately established in order to evaluate the effects of relatively low amounts of O₂. This also aided in understanding the damage to CNTs during the annealing process at a slow and noticeable rate. These studies were performed after dispersing CNC heterostructures on a cleaned silicon wafer. As the annealing temperature was increased, five main effects were observed: (1) nanoparticles on CNTs started migrating on the flat silicon wafer;

(2) these migrating nanoparticles aggregated around the CNTs but on the silicon wafer; (3) CNTs were damaged beyond 600 °C and eventually decomposed while some reacted with Fe catalyst nanoparticles as well as Ni/NiO core/shell nanoparticles to form carbides; (4) Ni/NiO core/shell nanoparticles as well as Fe catalyst nanoparticles oxidized at high temperature and a few hollow NiO nanoparticles resulted beyond 200 °C; (5) CNTs in CNC heterostructures decomposed at 750 °C. These results were also compared with the as-produced CNTs that were annealed under similar conditions. The as-produced CNTs, without any nanoparticles, survived only till 400 °C, and completely disappeared beyond this temperature, and the damage to these CNTs was initiated at 125 °C.

Figure 3.27 and Figure 3.29 show SEM and TEM images of the CNC heterostructures annealed at different temperatures. As observed, when annealed at 125 °C (Figure 3.27A and Figure 3.29A), a few CNTs with minor graphene layer straining were observed (inset in Figure 3.29A) and a very low extent of nanoparticle migration was observed. There was no CNTs wall damage observed at this temperature. After annealing at 200 °C, majority of the nanoparticles that were coating CNTs, surface migrated onto the silicon wafer (Figure 3.27B) and a few hollow nanoparticles evolved (Figure 3.29B, indicated by arrows). The migrated nanoparticles were spreading out around CNTs on the silicon wafer as shown in Figure 3.27B. In addition, CNTs walls were not yet damaged or broken as observed in Figure 3.29B. As the temperature increased to 400 °C (Figure 3.27C), the CNTs started being damaged, the walls got strained (Figure 3.29C, inset), and the majority of nanoparticles migrated to silicon wafer and aggregated on it. However, this nanoparticle aggregation was more obvious along the interfaces of the CNTs and silicon wafer and was not dispersed as compared to that at 200 °C annealing temperature (Figure 3.27B). Figure 3.29D (annealing temperature ~ 600 °C) shows that the CNTs were

damaged more with some amorphous carbon on the outer surface and some of them broke into smaller pieces while larger-sized aggregates of particles were also observed (Figure 3.29D). It must be noted here that as the interface between graphitic CNTs walls and silicon wafer is disrupted, several particle aggregates are also formed away from damaged CNTs on the silicon wafer. This indicates the role of surface curvature in nanoparticle migration at higher temperatures. In addition, CNTs tips were damaged resulting in tapered geometry (Figure 3.29E). The authors have previously reported migration of nanoparticles on nanowire surface, where the migration behavior was explained based on the chemical potential of the nanowire surface.⁹¹ This can help understand surface migration of Ni/NiO core/shell nanoparticles on silicon wafer from CNTs surface because chemical potential is much lower for a flat surface as compared to the high curvature CNTs. Finally, annealing of CNC heterostructures at 750 °C led to complete decomposition of CNTs (Figure 3.27E and Figure 3.29F) and irregular aggregated particles formed on the silicon wafer. Large-sized aggregates were also observed in TEM images as shown in Figure 3.29F. Another theory for the migration of nanoparticles is due to the force imbalance at interface between NiO and SiO₂ as showed in Figure 3.28. From previous data analysis (Figure 3.16), diameter of nanoparticles, distance between nanoparticles, and diameter of nanotubes could be calculated. The angle was calculated as 65.6 °. When $\gamma_1 > \gamma_2 \times \sin 65^\circ$, there is a tendency for nanoparticles to migrate from CNTs to silicon wafer surface.

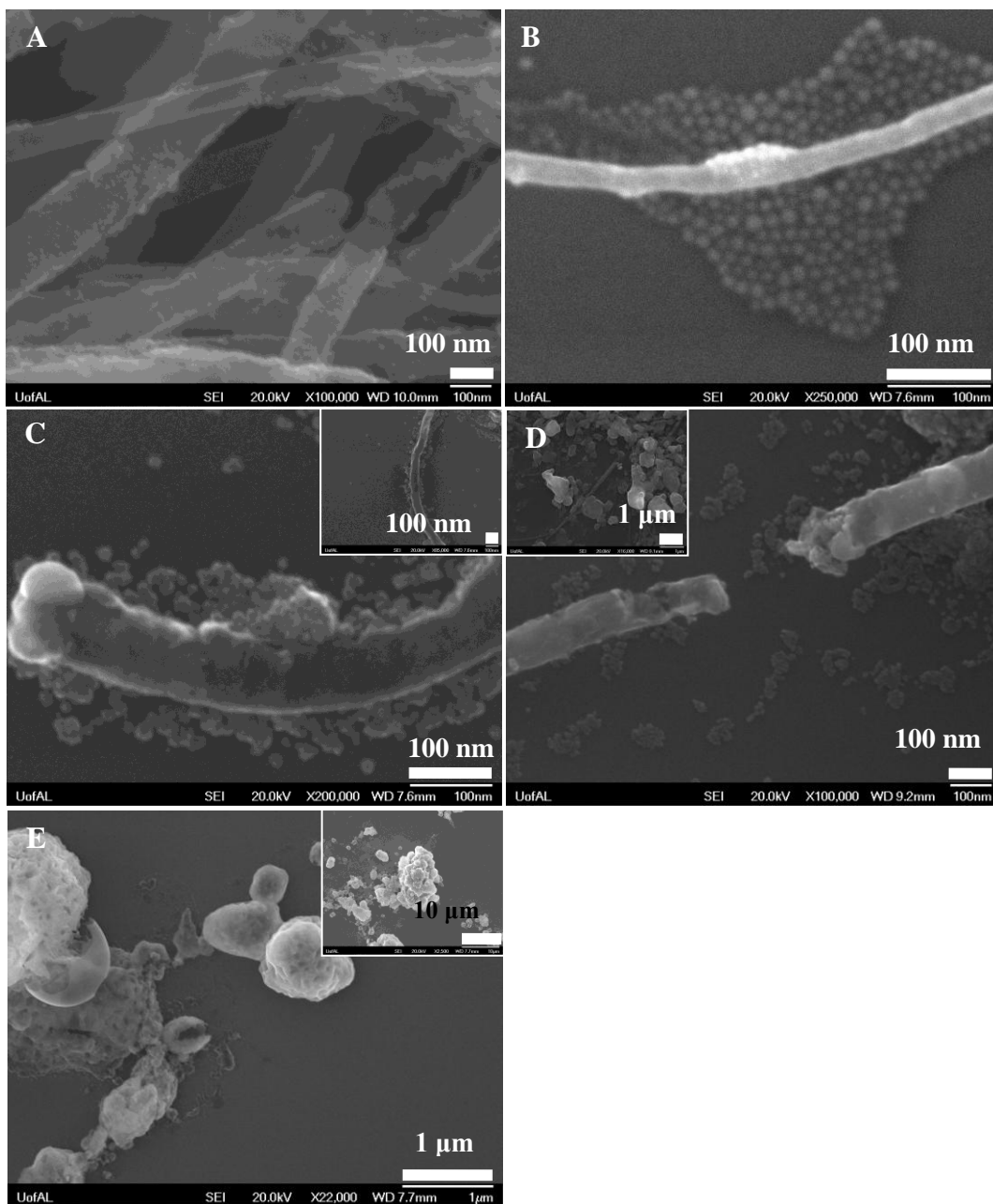


Figure 3.27 SEM images of CNC heterostructures dispersed on silicon wafer after annealing for 1 hr at (A) 125 °C, (B) 200 °C, (C) 400 °C, (D) 600 °C, and (E) 750 °C. Note: The CNC heterostructures were synthesized for 30 min growth duration. Inset images are showing a detailed view of the annealed CNC heterostructures.

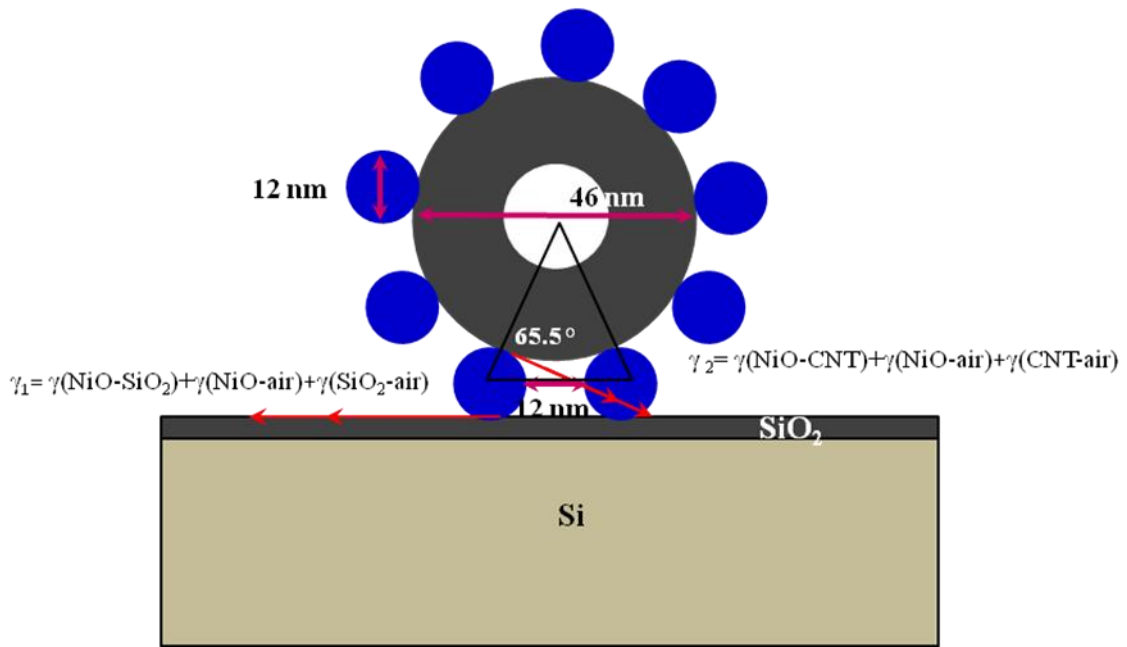


Figure 3.28 Schematic shows nanoparticle migration due to surface energy imbalance.

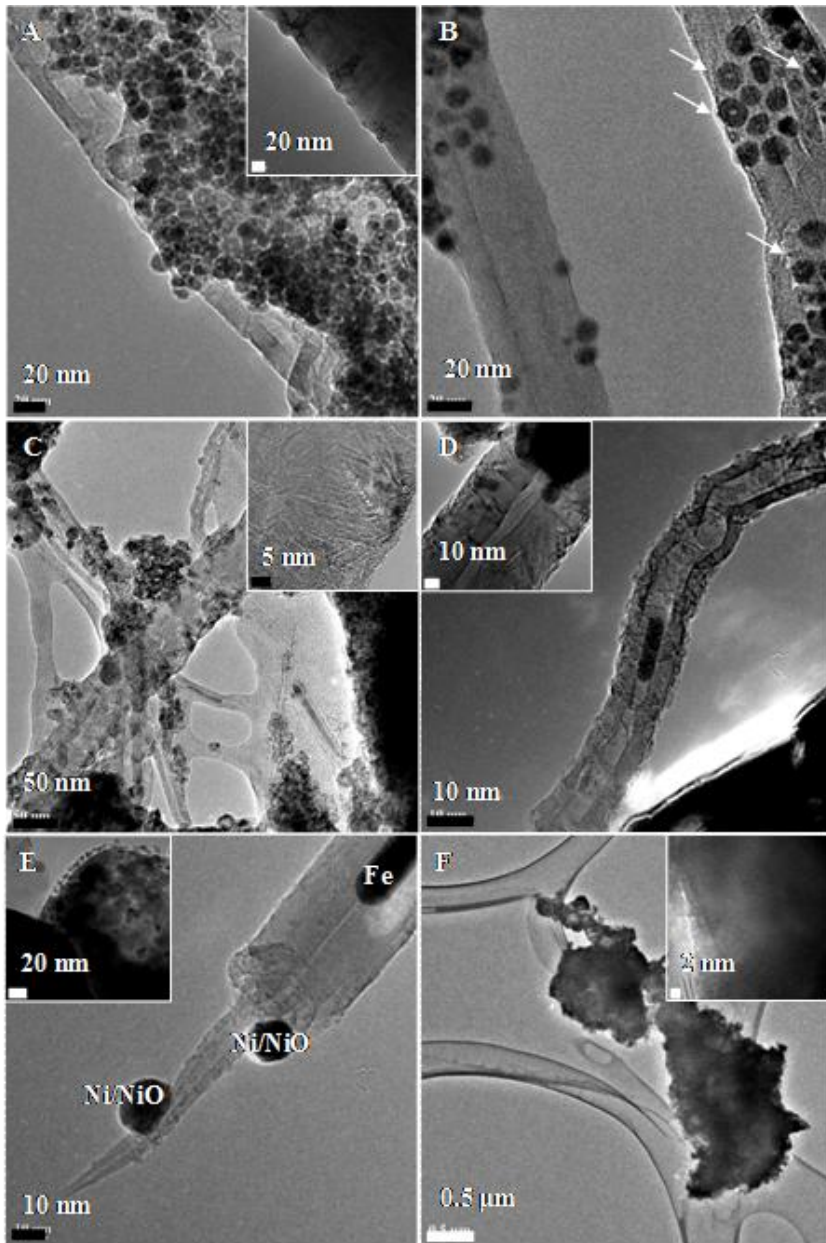


Figure 3.29 TEM images of CNC heterostructures after annealing for 1 hr at (A) 125 °C, (B) 200 °C (arrows indicate hollow nanoparticles), (C) 400 °C, (D) and (E) 600 °C, and (F) 750 °C. Note: CNC heterostructures were synthesized for 30 min reaction duration. These TEM images are taken for the samples observed in the SEM shown in Figure 3.26. The TEM samples were prepared by scratching the samples from the silicon wafer.

In order to understand the chemical compositions and phases of the individual component in CNC heterostructures as well as to quantify them as a function of annealing temperature, individual element XPS scans were conducted from high binding energy to low binding energy (Figure 3.30 and Figure 3.31, Table 4). Detailed peak deconvolution and data fitting was conducted. Ni 2p, Fe 2p, O 1s, and C 1s peaks were analyzed to gain information about Ni/NiO core/shell nanoparticles, Fe catalyst nanoparticle trapped inside the CNTs cores and CNTs itself. However, due to sample preparation limitations, it was not possible to maintain consistency in the sample amount on the substrate as heterostructures were randomly dispersed on the silicon wafer. In addition, the left-over surfactants (oleylamine, TOPO, and TOP) acted as a mask layer reducing the peak intensity as well as introducing minor binding energy shifts (< 0.1 eV). Thus, intensity of the XPS spectra were not comparable for different annealing samples and only the relative peak intensity, peak area, and peak location were analyzed.

For Ni 2p, there are overall six deconvoluted peaks for CNC heterostructures annealed below $400\text{ }^{\circ}\text{C}$ (Region 1, Table 4), that were assigned to Ni^{2+} 2p_{1/2} satellite, Ni^{2+} 2p_{1/2}, Ni^0 2p_{1/2}, Ni^{2+} 2p_{3/2} satellite, Ni^{2+} 2p_{3/2}, and Ni^0 2p_{3/2}, respectively (Table 4, Region 1).⁵⁸ In regard to Auger peaks (Table 4, Region 3), CNC heterostructures, irrespective of annealing process, showed a peak at 712.8 eV, which was consistent with Ni L₃M₂₃M₄₅(¹P).⁷⁴ For samples annealed above $400\text{ }^{\circ}\text{C}$, disappearance of metallic Ni peaks (Table 4, Region 1, Ni^0 2p_{1/2} and Ni^0 2p_{3/2}) were clearly observed, implying the oxidation of Ni core into NiO nanoparticles as shown in Figure 3.32. Due to the distinct chemical shifts for Ni^{2+} and Ni^0 , atomic percentages of Ni^{2+} and Ni^0 were also calculated. From the ratio between corresponding peak, it was concluded that with the increase in annealing temperatures, percentage of metallic nickel (Ni^0) decreased while oxidized nickel (Ni^{2+}) increased resulting in NiO nanoparticles (Figure 3.32A) with the threshold

temperature being 400 °C. The percentage of Ni⁰ (Figure 3.32A) at lower annealing temperatures or for non-annealed samples was much smaller than Ni²⁺ and this could be attributed to the nature of XPS characterization as the technique is only for surface analysis and encountered significant amount of NiO as compared to the metallic core. Previous studies on core/shell nanoparticle characterization using XPS have reported similar observations for other material systems, where signal from the core was suppressed by the shell.⁹²

Since CNTs were grown from catalytic Fe nanoparticles in CVD process, it was expected that Fe would be present in these heterostructures and this is evidenced by a peak at 706.91 eV corresponding to Fe 2p_{3/2} line.⁷⁴ This peak is slightly shifted (Table 4, Region 3) for CNC heterostructures before and after annealing and that could be an additional contribution from Ni L₃M₂₃M₄₅(³P) Auger peak.⁷⁴ However, overlapping of the peak for Fe 2p_{3/2} and/or Ni L₃M₂₃M₄₅(³P) made it difficult to resolve it further. For the as-produced CNTs, there were clearly two peaks (Table 4, Region 2) at 719 eV and 706.91 eV from Fe 2p_{1/2} and Fe 2p_{3/2},⁷⁴ respectively and these peaks were observed for CNC heterostructures without annealing as well as for heterostructures annealed below or at 400 °C. A new peak (~ 710 eV) emerged when the annealing temperature was above 400 °C and corresponded to the oxidized form of iron (e.g., FeO, Fe₂O₃, and Fe₃O₄, denoted as Fe^{x+} in Figure 3.32B, where x can be 2 or 3).⁷⁴ The oxidation of Fe is also indicative of CNTs damage, opening, and cutting at these annealing temperatures as the Fe catalyst nanoparticle is slowly exposed to the annealing environment. Based on XPS analysis, percentage of Fe^{x+} was plotted as a function of annealing temperature (Figure 3.32B) and shows the presence of Fe^{x+} species beyond 200 °C. The percentage of Fe^{x+} was observed to increase from 0% (at 200 °C) to ~ 65% (above 600 °C). This indicates some CNTs were damaged above 200 °C and these CNTs could have been the ones that were not having good

Ni/NiO core/shell nanoparticle coverage as the process of heterostructure formation is not 100% efficient.

Usually interpretation of O 1s peak is difficult because of complexity of oxides peaks and co-existence of oxygen in CNC heterostructures (e.g., TOP, TOPO, -COOH, -OH, NiO, Fe_xO).⁷⁴ There are several conclusions from this set of XPS spectra (Table 4, Region 4). For the as-produced CNTs, O 1s peak located at 532.37 eV is due to surface adsorbed carboxylic acid (-COOH) species or hydroxyl (-OH) on CNTs.⁹³ The O 1s peak shift to 531.79 eV (non-annealed CNC heterostructures) and to 531.96 eV, 531.97 eV for heterostructures annealed at 125 °C, 200 °C, respectively. These can be attributed to oxygen from TOPO and TOP.⁹⁴ However, when the temperature was much above the boiling point of TOP (~ 291 °C) and TOPO (~ 202 °C), (MSDS, Sigamaldrich) these stabilizers evaporated away. Thus, for samples annealed at 400 °C and 600 °C, O 1s main peaks shifted back to 532.4 eV and 532.17 eV, respectively. There was another O 1s shoulder peak at ~ 529 eV beyond 400 °C annealing temperature, which could be assigned to metal oxides from Ni and Fe.^{74,93}

Since C 1s peaks were used to correct all the spectra and the presence of carbon species was not only from CNTs but also from surfactants and XPS contamination, detailed deconvolution is not performed here. However, there are several important observations (Table 4, Region 5). First, for C 1s from the as-produced CNTs, there was a peak at ~ 290.65 eV due to π - π^* transition and adsorbed oxygen species.⁹³ However, for samples loaded with Ni, this peak disappeared and the authors believe that it is because of a strong interaction between CNTs surface and nanoparticles as well as remaining stabilizer molecules. CNTs were more exposed as nanoparticles migrated to the silicon substrate (Figure 3.27), but XPS results do not show π - π^*

transition for these samples. This could be due to amorphous carbon coating on CNTs at high temperatures (also indicated in Figure 3.29). Second, for samples annealed above 400 °C, there was a low-intensity shoulder close to C 1s (Figure 3.31), which was assigned to carbides of Fe and Ni.⁷⁴ Thus, as the annealing temperature was increased, more CNTs damage occurred and to some extent, the metals present, reacted with this carbon resulting in carbides.

Although TEM and SEM showed presence of CNTs at high temperature, small sampling area might cause some inaccuracy. Thus, Raman spectra (Figure 3.33) were collected for samples annealed above 400 °C. It was found that D and G bands existed as high as 600 °C while disappeared at 750 °C. Thus CNTs must decompose at temperature range from 600 °C to 750 °C. Another interesting thing is the decreasing of G/D band ratio, which directly demonstrates formation of defects at high temperature annealing.

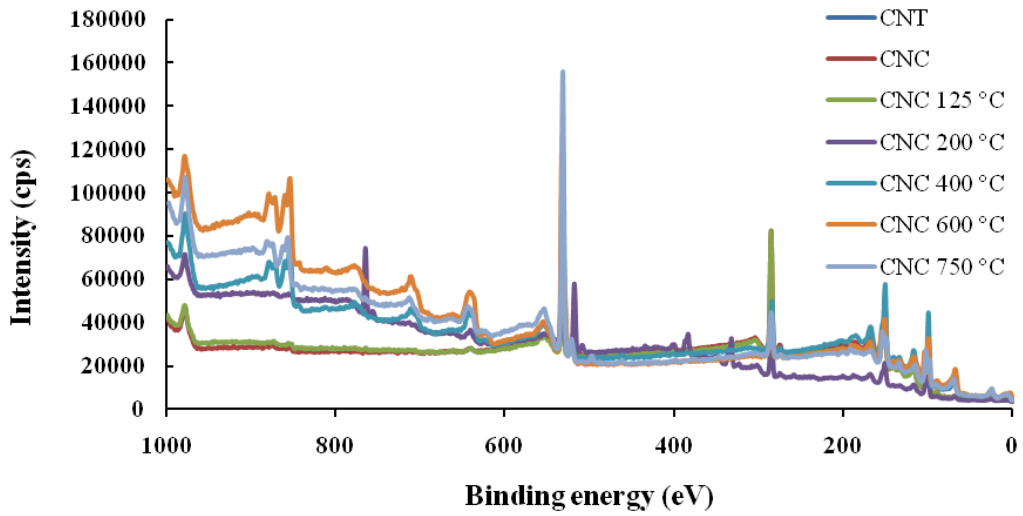


Figure 3.30 XPS spectra of CNTs and CNC heterostructures before and after annealing at different temperatures. Table 4 shows the precise peak locations for each constituent present. ‘CNT’ represents as-produced CNTs.

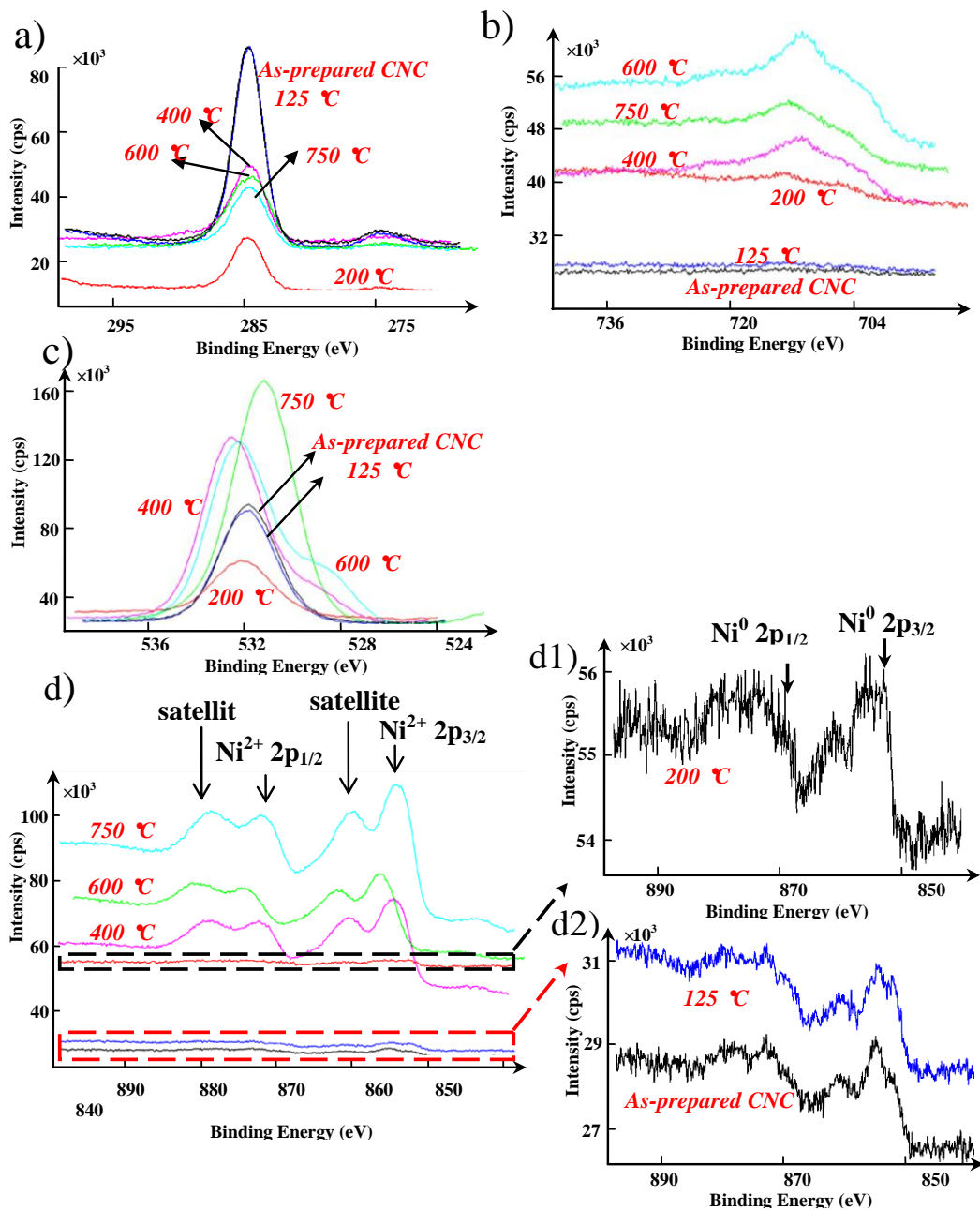


Figure 3.31 XPS spectra of (a) C 1s, (b) Fe 2p, (c) O 1s, (d) Ni 2p for different annealing temperatures. The dotted lines in (d) for the spectra at 125 °C and 200 °C are shown as d1 and d2. Note: Spectra for as-prepared CNC heterostructures and those annealed at 125 °C are nearly overlapping. Thus, indicating minimal changes in chemical composition at low temperatures.

Table 4 Binding energy (eV) chart derived from XPS study for as-produced CNTs, CNC heterostructures, and CNC heterostructures after annealing.

Region	Peak Assignment	Binding Energy (eV)						
		CNT	CNC	CNC (125 °C)	CNC (200 °C)	CNC (400 °C)	CNC (600 °C)	CNC (750 °C)
Ni								
1	Ni ²⁺ 2p _{1/2} satellite	/	879.25	879.87	880.995	879.01	878.654	880.711
	Ni ²⁺ 2p _{1/2}	/	873.35	873.56	874.668	872.411	872.106	874.578
	Ni ⁰ 2p _{1/2}	/	870.37	870.3	870.366	/	/	/
	Ni ²⁺ 2p _{3/2} satellite	/	861.17	860.97	861.15	860.713	860.172	862.066
	Ni ²⁺ 2p _{3/2}	/	855.38	854.98	855.794	854.624	854.144	856.358
	Ni ⁰ 2p _{3/2}	/	852.7	852.45	852.678	/	/	/
Fe								
2	Fe 2p _{1/2}	719	719.34	720.95	720.5	721.22	721.3	722.62
	Fe ^{x+}	/	/	/	/	710.05	709.62	710.17
Ni and Fe Auger peaks								
3	Ni L ₃ M ₂₃ M ₄₅ (¹ P)	/	712.8	712.95	712.94	713.28	712.06	712.85
	Fe 2p _{3/2} or Ni L ₃ M ₂₃ M ₄₅ (³ P)	706.91	706.42	706.34	706.75	705.07	703.63	705.27
O								
4	O 1s	532.37	531.79	531.96	531.97	532.4	532.17	531.24
	O shoulder	/	/	/	/	529.35	528.72	
C								
5	π-π*	290.65	/	/	/	/	/	/
	C shoulder	/	/	/	/	288.27	288.15	287.89
	C 1s	284.8	284.8	284.8	284.8	284.8	284.8	284.8

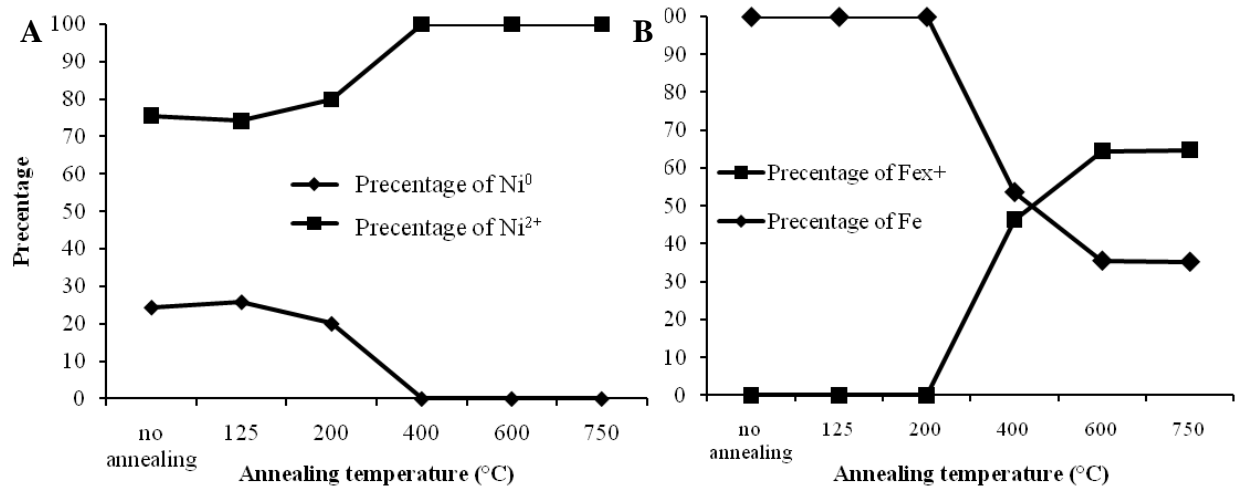


Figure 3.32 Phase change of Ni⁰ (present in Ni/NiO core/shell nanoparticles) and Fe⁰ (catalyst present in the CNTs inner core) observed as a function of annealing temperature for CNC heterostructures. (A) Conversion of Ni to Ni²⁺ (NiO) and (B) conversion of Fe to Fe^{x+} (various oxides of Fe such as FeO, Fe₂O₃, and Fe₃O₄).

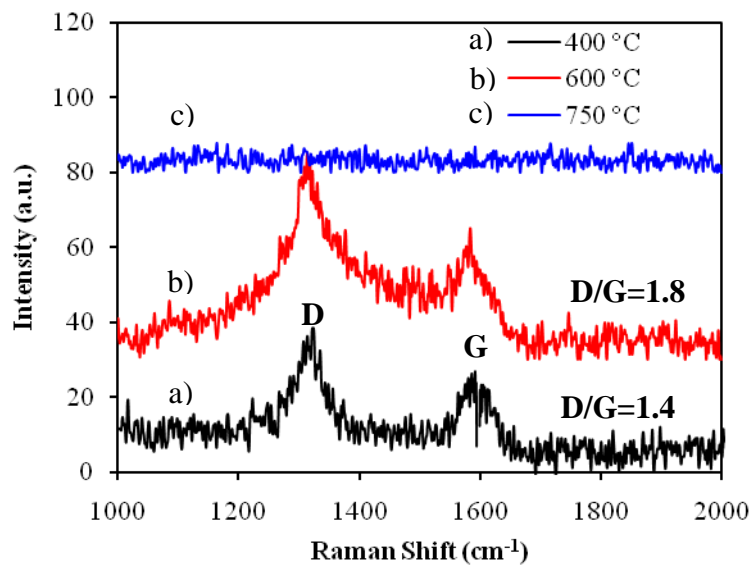


Figure 3.33 Raman spectra of CNC heterostructures showing D and G bands of CNTs after heat treatment at a) 400 °C, b) 600 °C, and c) 750 °C.

Kinetics of nickel nanoparticles oxidation was also analyzed. For the XPS analysis, the analyzing depth is usually at 1-10 nm. Thickness of NiO shell could be calculated from TEM images and ratio of Ni⁰ and Ni²⁺ at room temperature could be calculated from XPS. Thus, it is possible to estimate the analyzing depth of the coated nanoparticles on CNTs in XPS. Since the volume for a spherical cap could be calculated using

$$V = \frac{\pi h^2}{3}(3r - h) \quad (3-15)$$

where r is the radii of sphere and h is the height of the cap.

Since the diameter of nanoparticle is ~ 11.9 nm and thickness of shell is ~ 2 nm (Figure 3.8), when the XPS analyzing depth is h nm, the volume of Ni core is

$$V_{Ni} = \frac{\pi(h - 1.8)^2}{3} \left(3 \times \frac{(11.9 - 1.8 \times 2)}{2} - (h - 1.8) \right) \quad (3-16)$$

and the volume of NiO shell is

$$V_{NiO} = \frac{\pi h^2}{3} \left(3 \times \frac{11.9}{2} - h \right) - \frac{\pi(h - 1.8)h^2}{3} \left(3 \times \frac{(11.9 - 1.8 \times 2)}{2} - h \right) \quad (3-17)$$

From XPS spectrum

$$Ni^0\% = \frac{V_{Ni}}{V_{Ni} + V_{NiO}} = 24.45\% \quad (3-18)$$

Analyzing depth could be calculated.

$$h = 6.36 \text{ nm}$$

Assuming that oxidation of nanoparticles is isotropic, thus, thickness of oxide shell (a) at different temperature could be calculated through Ni% from XPS (Figure 3.31).

$$Ni^{0\%} = \frac{V_{Ni}}{V_{Ni} + V_{NiO}} = \frac{\frac{\pi(6.36 - a)^2}{3} (3 \times \frac{(11.9 - a \times 2)}{2} - (6.36 - a))}{\frac{\pi \times 6.36^2}{3} (3 \times \frac{11.9}{2} - 6.36)} \quad (3-19)$$

In general, it was assumed that the rate of oxidation, $d\alpha/dt$, is a linear function of a temperature-dependant rate constant, $k(T)$, and a temperature-independent function of the oxidation ratio, $f(\alpha)$,⁹⁵

$$\frac{d\alpha}{dt} = k(T)f(\alpha) \quad (3-20)$$

where α is the oxidation ratio and the rate constant $k(T)$ is typically expressed by the Arrhenius relation:

$$K(T) = k_0 \exp[-E_a/k_B T] \quad (3-21)$$

Thus,

$$\frac{d\alpha}{dt} = k(T)f(\alpha) = k_0 \exp[-E_a/k_B T] \quad (3-22)$$

where k_0 , the pre-exponential factor, is assumed to be independent of temperature, E_a is the activation energy, T is the absolute temperature, and k_B is the Boltzmann constant. Since in our experiment, time is kept as constant. After integration at both side,

$$\alpha = tk_0 \exp[-E_a/k_B T] \quad (3-23)$$

$$\ln \alpha - \ln \alpha_0 = \ln (tk_0) - E_a/k_B T \quad (3-24)$$

Therefore, the natural logarithm of oxidation ratio should be linearly proportional to inverse of temperature as showed in Figure 3.34. From the linear function and the fixed time, pre-exponential factor (k_0) and activation energy (E_a) could be calculated.

$$\ln(tk_0)=0.0084$$

$$k_0= 0.0168 \text{ min}^{-1}$$

$$E_a/k_B=0.0167 \text{ K}$$

$$E_a=2.3 \times 10^{-25} \text{ J}$$

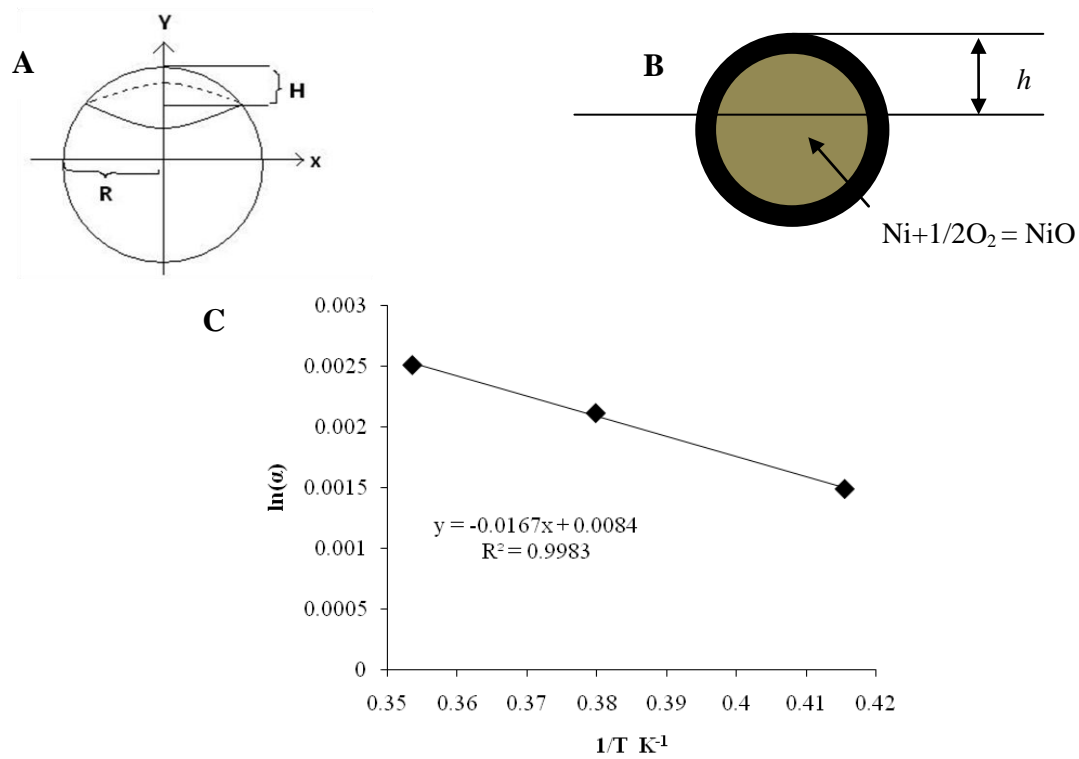


Figure 3.34 (A) Volume of spherical cap. (B) Oxidation of Ni core into NiO shell, (C) Kinetic fitting of oxidation.

Table 5 Shell thickness and conversion percentage at different temperatures

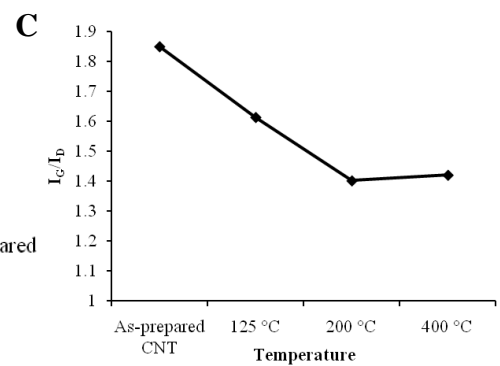
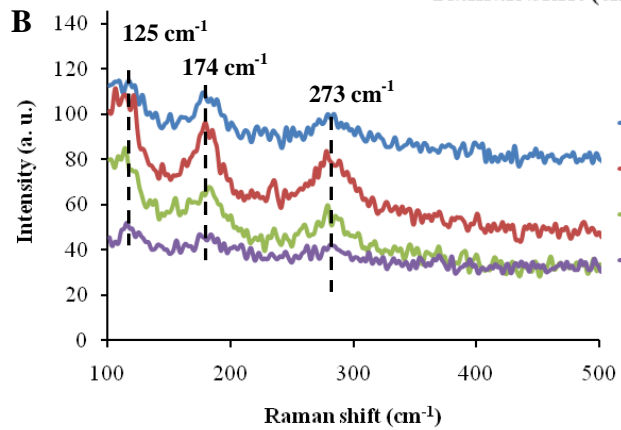
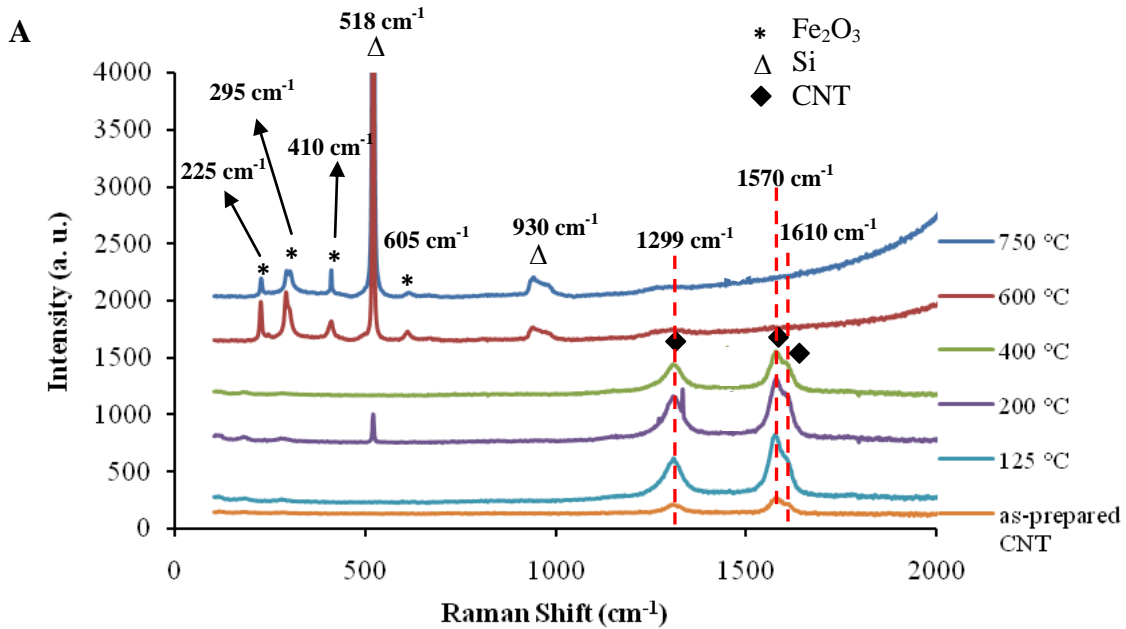
Temperature (°C)	Shell thickness (nm)	Oxidation Percentage (%)
25	1.8	66
125	3.69	94
200	4	96.5
400	6.63	100

To compare the thermal (or oxidative) stability of CNC heterostructures with the as-produced CNTs, similar annealing experiments were conducted for the latter and studied using Raman spectroscopy and electron microscopy. Figure 3.35 shows Raman spectra for the as-produced CNTs and the effect of annealing temperatures. Two principal bands (Figure 3.35A) corresponding to the disordered sp^2 carbon (maximum at $\sim 1299\text{ cm}^{-1}$, also referred as D-band) and well-ordered graphitic band (maximum at $\sim 1570\text{ cm}^{-1}$, also referred as G-band or E_{2g} band) were observed.⁶⁶ It is well known that the D bands originate due to defects present in CNTs and as shown in Figure 3.35A, the intensity of D-band slightly increased with annealing temperature (for $125\text{ }^\circ\text{C}$ and $200\text{ }^\circ\text{C}$). This increase in intensity indicates the formation of defects in CNTs and similar trends have been observed in high temperature treatment of CNTs.⁹⁶ A shoulder is also observed (Figure 3.35A) at $\sim 1610\text{ cm}^{-1}$, that corresponded to D' band consistent with end planes of graphene layers.⁹³ With increasing annealing temperature, it was observed that these peaks and the shoulder disappear beyond $400\text{ }^\circ\text{C}$ indicating complete decomposition of CNTs at this temperature. Thus, as compared to CNC heterostructures where CNTs were still present but damaged at $600\text{ }^\circ\text{C}$ (Figure 3.27D, Figure 3.28D, and Figure 3.28E), the as-produced CNTs decomposed completely at a lower temperature (beyond $400\text{ }^\circ\text{C}$). In addition, the damage to CNTs walls in case of the annealed as-produced CNTs can be further understood by the emergence of breathing-like modes (BLMs)⁹⁷ as shown in Figure 3.35B. These Raman modes are similar to radial breathing modes for SWCNTs and were recently reported for low diameter ($< 5\text{ nm}$) MWCNTs. BLMs majorly arise due to coupling between the shells of such MWCNTs.⁹⁴ This could indicate that as the annealing temperature was increased from $125\text{ }^\circ\text{C}$ to $400\text{ }^\circ\text{C}$ (Figure 3.35B), the CNTs were decreasing in wall thickness and as a result, several CNTs with very low diameters emerged. Finally, beyond $400\text{ }^\circ\text{C}$, the remaining CNTs reacted with the

surrounding oxygen present in the N₂-rich atmosphere and decomposed. Figure 3.35C clearly shows the intensity ratio between the G-band and D-band (I_G/I_D) from the Raman spectra as a function of annealing temperature. It shows that the graphitic content of the CNTs significantly lowered with increasing temperature. However, slight increment in the ratio beyond 200 °C indicates that the CNTs just below their decomposition temperature corresponded to relatively low diameter and graphitic CNTs.

On the other hand, it can be clearly seen that a few peaks below 1000 cm⁻¹ (Figure 3.35A) emerged as the annealing temperature was raised beyond 400 °C and these peaks (225 cm⁻¹, 295 cm⁻¹, 410 cm⁻¹, and 605 cm⁻¹) correspond to the oxidized form of Fe catalyst (mostly Fe₂O₃),⁹⁸ which is present in the as-produced CNTs. The optical images (Figure 3.35D a-e) show the regions that were evaluated in the Raman spectroscopy for the as-produced CNTs after the treatment at various annealing temperature. It can be seen that beyond 400 °C, a reddish brown precipitate was left over the substrate demonstrating the formation of oxides of Fe catalyst and decomposition of CNTs. To further validate our spectroscopic and optical imaging results, SEM and TEM characterization studies revealed more interesting information on the thermal stability of the as-produced CNTs, which was noticeably different from CNC heterostructures. Although not evident from the SEM images, (Figure 3.36) TEM images clearly show thinning of CNTs walls and tips at 125 °C annealing temperature. Stress marks on CNTs, graphene layer cutting, disappearance of CNTs core, and coalescence of Fe catalyst nanoparticles could be easily seen in the TEM images (inset, Figure 3.36B and C) corresponding to 200 °C and 400 °C. Furthermore, beyond 400 °C (i.e., 600 °C and 750 °C), CNTs completely decomposed and only aggregated Fe₂O₃ nanoparticles were observed on the substrate (Figure 3.36D and E). This aggregation significantly increased at 750 °C. The lattice spacing of Fe₂O₃ (0.415±0.005 nm for (101),

JCPDS No. 13-534) nanoparticles is showed in Figure 3.36E (inset). Overall, it can be stated that the CNTs when loaded with Ni/NiO core/shell nanoparticles showed a higher decomposition temperature and greater thermal stability (or oxidative resistance) as compared to the as-produced CNTs in similar annealing conditions. This unique observation is very useful for high temperature applications of CNC heterostructures.



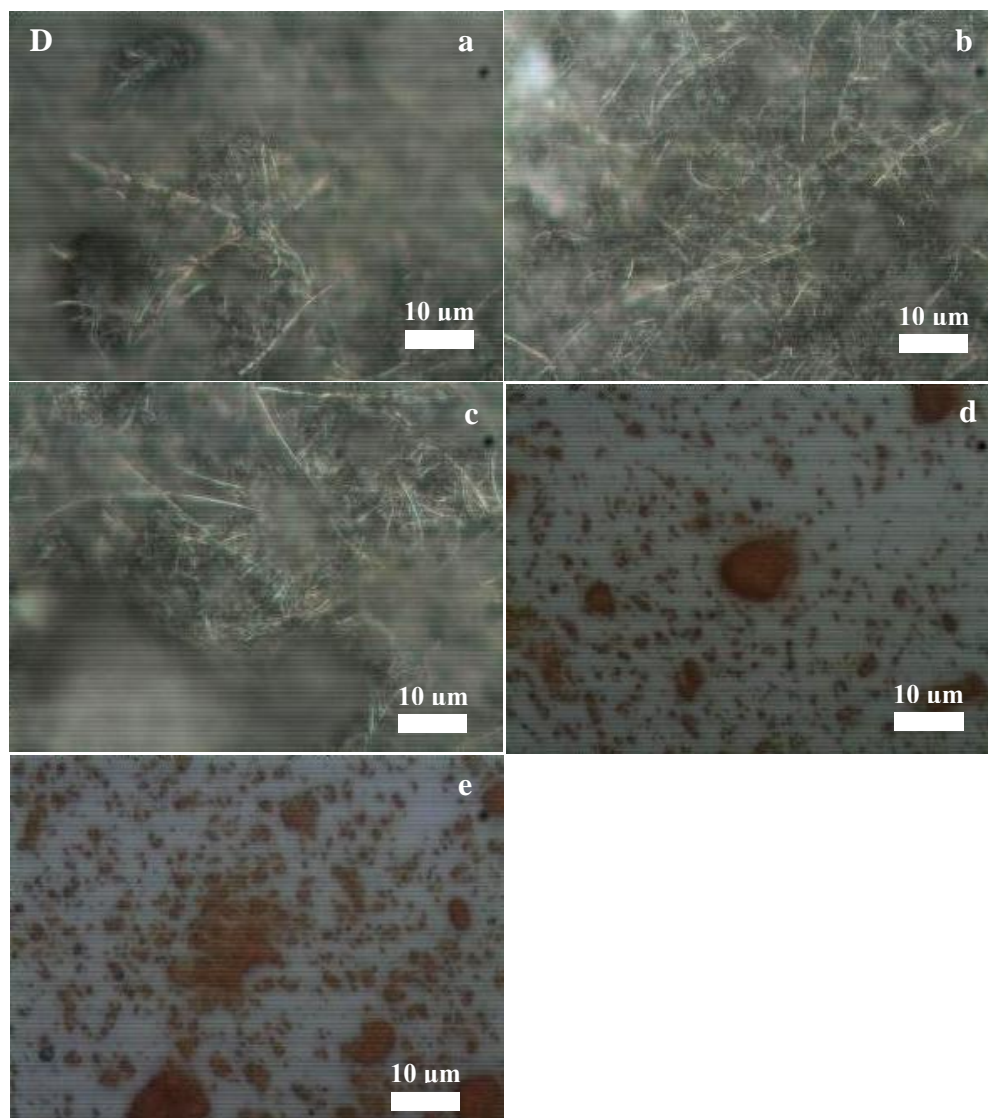


Figure 3.35 (A) Raman spectra of as-prepared CNTs and CNTs annealed at various temperatures (125 – 750 °C). (B) Breathing-like modes (BLMs) of MWCNTs up to 400 °C annealing temperature. (C) The I_G/I_D ratio for CNTs as a function of annealing temperature. (D)a-e The optical images of CNTs before and after annealing corresponding to the region considered for Raman spectra acquisition. Note: Since CNTs were dispersed on silicon wafer, two silicon peaks (518 cm^{-1} and 930 cm^{-1}) were observed at higher annealing temperatures.

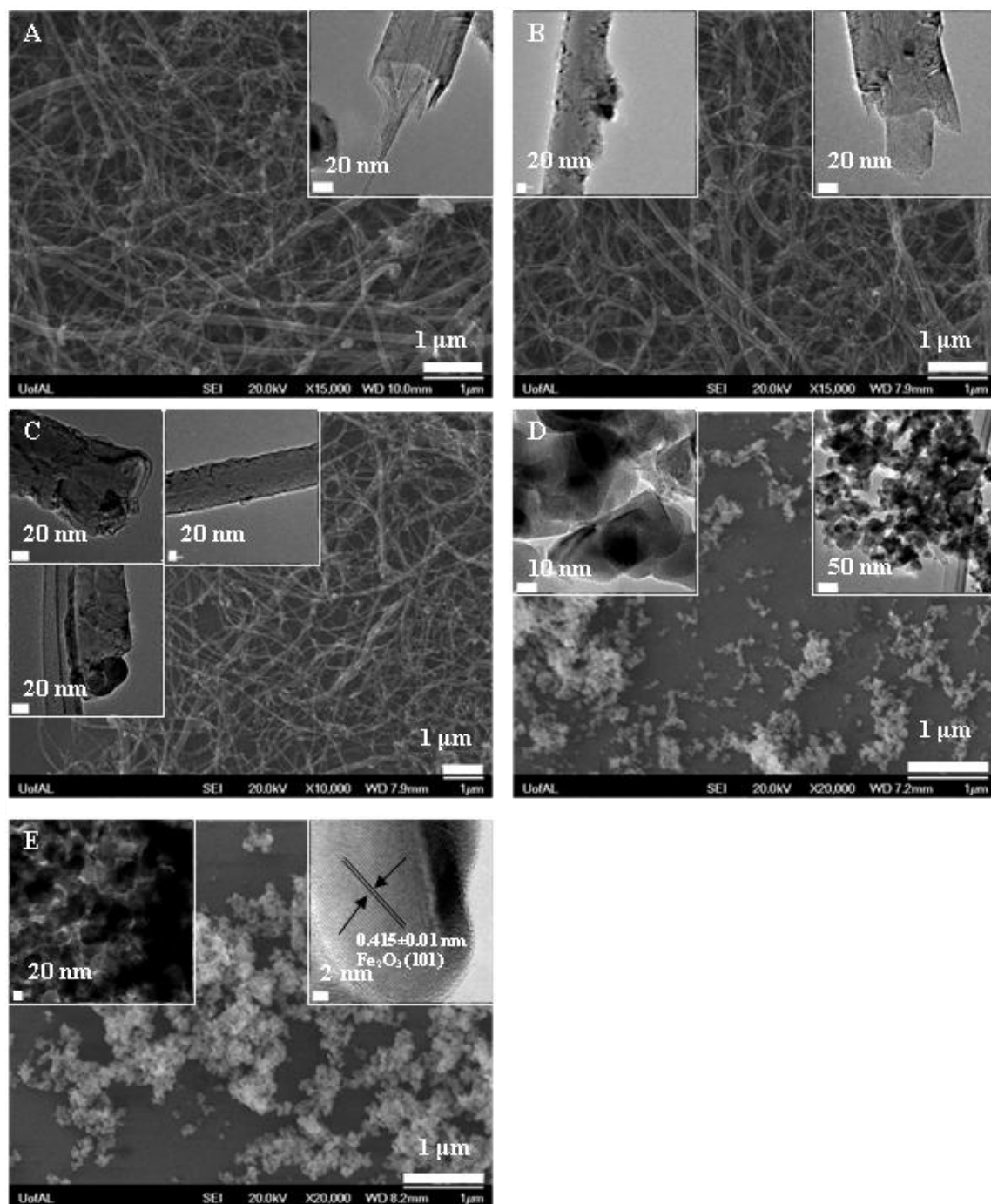


Figure 3.36 SEM and TEM (inset) images for the as-produced CNTs after annealing for 1 hr at (A) 125 °C, (B) 200 °C, (C) 400 °C, (D) 600 °C, and (F) 750 °C. The images demonstrate the various outcomes of the annealing process on the as-produced CNTs and show that these CNTs are damaged at as low as 125 °C.

Chapter 4

CONCLUSION AND FUTURE WORK

CNC heterostructures were fabricated in a single-step, simple synthetic approach by directly nucleating narrow-sized Ni/NiO core/shell nanoparticles (average diameter $\sim 12 \pm 2$ nm) on the surface of CNTs. High surface area CNTs allowed for uniform dispersion and ideal packing of core/shell nanoparticles. These heterostructures were thoroughly characterized for their crystal structure, morphology, phase, and interface using microscopic and diffraction techniques. The structural control of Ni/NiO core/shell nanoparticles on the CNTs surface was achieved in a single-step synthesis by only varying the duration of the nanoparticle growth reaction after the addition of stabilizer molecules to the solution. This resulted in well-controlled shapes, sizes, spatial densities, and inter-particle spacing of Ni/NiO nanoparticles on CNTs surface as observed in SEM, TEM, and XRD. As the growth time was increased from 15 min to 10 hrs, average size of the nanoparticles increased from $\sim 12.5 \pm 2.1$ nm to $\sim 51.8 \pm 9.8$ nm, the spatial density of nanoparticles on the surface of CNTs decreased by 97.1%, inter-particle spacing increased by ~ 9 folds, and different shapes (circular, pentagonal, quadrilateral, and triangular) of nanoparticles evolved beyond 2 hrs. A detailed morphological evolution mechanism was also derived based on stabilizer micelle rupturing coupled with surface tension forces and nickel content on the CNTs surface. Another interesting observation for CNC heterostructures, irrespective of the growth time, was the bending of graphene layers or defective CNTs walls in the space between two adjacent nanoparticles. In addition, for much prolonged growth time (15 hrs), the growing Ni nanoparticles on the CNTs surface reacted with the phosphine-based stabilizer to result in CNTs- Ni_{12}P_5 nanoparticle heterostructures. These phosphide nanoparticles (diameter $\sim 11.1 \pm 1.8$ nm)

exhibited different shapes as well as ~ 26.6% of the nanoparticles were hollow with average shell thickness of $\sim 2.9 \pm 0.4$ nm.

CNC heterostructure were then uniformly incorporated into a PVA hydrogel resulting in novel hybrid materials (CNC heterostructure-PVA hydrogel), which showed ~ 73% of water absorbing capacity comparable to pure PVA hydrogel (~ 75%). This indicated that CNC heterostructures had negligible effect on the porosity/pore volume of the hybrid material. FTIR spectroscopy was utilized to understand chemical functionalities in CNC heterostructure-PVA hydrogel. These hybrid materials were studied for their use as selective chemical and biological separation or concentrating media. It was also demonstrated in a series of chemical separation experiments that the functionality of Ni/NiO core/shell nanoparticles, present in CNC heterostructure-PVA hydrogel, was reversed for histidine and histidine-tagged proteins. Interestingly, CNC heterostructure-PVA hydrogel showed no affinity for histidine or histidine-tagged protein and assisted in concentrating these molecules in solution. Chemical separation of methyl orange from a mixture of methyl orange and L-histidine was also achieved using CNC heterostructure-PVA hydrogel immersed in the solution. Such selective and reversed-functionality hydrogels can be very useful for developing advanced chemical and biological sensors, protein concentrating and chemical separation media, drug delivery, and smart analytical platform that incorporates multiple components in one system.

The ability of as-prepared composite hydrogel in drug delivery was also tested. It was found that hydrogel could slowly release pre-loaded molecules. Interestingly, it was found that external cycled magnetic field could be used to control the release rate due to the magnetic behavior of CNC heterostructures.

Finally, thermal stability of CNC heterostructures and the influence of annealing temperatures on their morphology, phase, crystallinity, and chemical composition were studied. It was observed that CNTs in the CNC heterostructures decomposed at higher temperatures (beyond 600 °C) as compared to the as-produced CNTs (beyond 400 °C). Structural and chemical changes in CNTs were fully evaluated for the given annealing conditions using SEM, TEM, XPS, and Raman Spectroscopy.

Future of this thesis will involve developing multifunctional and multicomponent CNTs-nanoparticle heterostructures for developing selectively chemical and biological sensors, as well as high temperature catalysts. The proposal is to selectively load two different nanoparticles onto CNTs, and then utilize the diverse surface chemistry of the heterostructures to derive complex devices and nanocomposites. This whole approach will involve through fundamental understand via characterization method and growth studies. The knowledge of structures and properties of these heterostructures will lead to realization of the real life prototype analytical devices.

REFERENCES

- 1 Roduner, E. Size matters: Why nanomaterials are different. *Chemical Society Reviews*, **35**, 583-592 (2006).
- 2 Rioux R. M., Song H., Hoefelmeyer J. D., Yang P., Somorjai G. A.. High-Surface-Area Catalyst Design: Synthesis, Characterization, and Reaction Studies of Platinum Nanoparticles in Mesoporous SBA-15 Silica. *Journal of Physical Chemistry B* **109**(6), 2192-2202 (2005).
- 3 Chen W., Tao X., Xue P., Cheng X.. Enhanced mechanical properties and morphological characterizations of poly(vinyl alcohol)-carbon nanotube composite films. *Applied Surface Science* **252**, 1404-1409 (2005).
- 4 Che M, Liu J.P., Sun, S. H.. One-Step Synthesis of FePt Nanoparticles with Tunable Size. *Journal of American Chemical Society* **126**(27), 8394-8395 (2004).
- 5 Huang Y., Duan X., Cui Y., Lauhon L. J., Kim K. H., Lieber C. M.. Logic Gates and Computation from Assembled Nanowire Building Blocks, *Science* **294**, 1313-1317 (2001).
- 6 Liu M., Yin X., Ulin-Avila E., Geng B., Zentgraf T., Ju L., Wang F., Zhang X.. A graphene-based broadband optical modulator, *Nature* **474**, 64-67 (2011).
- 7 Hu J., Odom T. W., Lieber C. M.. Chemistry and Physics in One Dimension: Synthesis and Properties of Nanowires and Nanotubes. *Account of Chemical Research* **32**(5), 435-445 (1999).
- 8 Meyyappan M.. Carbon nanotubes: Science and applications, 2005, Boca Raton, Florida, CRC Press LLC.
- 9 Lauhon L. J., Gudixsen M. S., Lieber C. M.. Semiconductor Nanowire Heterostructure, *Philosophical Transactions of the Royal Society A* **362**, 1247-1260 (2004).
- 10 Chopra N., Claypoole L., Bachas L. G.. Formation of Ni/NiO Core/shell Nanostructures and Their Attachment on Carbon Nanotubes. *NSTI Nanotech 2009 Proceedings* **1**, 187-189 (2009).
- 11 Chopra N., Majumder M., Hinds B. J.. Bi-functional Carbon Nanotubes by Sidewall Protection. *Advanced Functional Material* **15**(5), 858-864 (2005).
- 12 Shen G., Chen D., Bando Y., Goldberg D.. One Dimensional Nanoscale Heterostructures. *Journal of Materials Science Technology* **24**, 541-549 (2008).

- 13 Li X. L., Liu Y. Q., Fu L., Cao L. C., Wei D. C., Wang Y.. Efficient Synthesis of Carbon Nanotube-Nanoparticle Hybrids. *Advanced Functional Material* **16**(18), 2431-2437 (2006).
- 14 Kongkanand A., Dom ínguez R. M., Kamat P. V.. Single Wall Carbon Nanotube Scaffolds for Photoelectrochemical Solar Cells. Capture and Transport of Photogenerated Electrons. *Nano Letters* **7**(3), 676-680 (2007).
- 15 Gao B., Peng C., Chen G. Z., Puma G. L.. Photo-electro-catalysis Enhancement on Carbon Nanotubes/titanium Dioxide (CNTs/TiO₂) Composite Prepared by a Novel Surfactant Wrapping Sol-gel Method. *Applied Catalyst B: Environmental* **85**(1-2), 17-23 (2008).
- 16 Peng X., Chen J., Misewich J. A., Wong S.S.. Carbon Nanotube-Nanocrystal Heterostructures. *Chemical Society Reviews* **38**(4), 1076-1098 (2009).
- 17 Quinn B. M., Dekker C., Lemay S. G.. Electrodeposition of Noble Metal Nanoparticles on Carbon Nanotubes. *Journal of American Chemical Society* **127**, 6146-6147 (2005).
- 18 Tzitzios V., Georgakilas V., Oikonomou E., Karakassides M., Petridis D.. Synthesis and Characterization of Carbon Nanotube/metal Nanoparticle Composites Well Dispersed in Organic Media. *Carbon* **44**(5), 848-853 (2006).
- 19 Iijima S., Helical microtubules of graphitic carbon. *Nature* **354**, 56-58 (1991).
- 20 Gabor N. M, Zhong Z., Bosnick K., Park J., McEuen P. L.. Extremely Efficient Multiple Electron-Hole Pair Generation in Carbon Nanotube Photodiodes. *Science* **325**, 1367-1371 (2009).
- 21 Cheng H. M., Yang Q. H., Liu C.. Hydrogen storage in carbon nanotubes. *Carbon* **39**(10), 1447-1454 (2001).
- 22 An K. Y., Kim W. S., Park Y. S., Moon J. M., Bae D. J., Lim S. C., Lee Y. S., Lee Y. H.. Electrochemical Properties of High-Power Supercapacitors Using Single-Walled Carbon Nanotube Electrodes. *Advanced Functional Materials* **11**(5), 387-392 (2001).
- 23 RodrÃ uez-Manzo J. A., Wang M. S., Banhart F., Bando Y., Golberg D. Multibranched Junctions of Carbon Nanotubes via Cobalt Particles. *Advanced Materials* **21**(44), 4477-4482 (2009).
- 24 Li X., Jia Y., Cao A. Tailored Single-Walled Carbon Nanotube CdS Nanoparticle Hybrids for Tunable Optoelectronic Devices. *ACS Nano* **1**(4), 506-512 (2009).

- 25 Andrews R., Jacques D., Rao A.M., Derbyshire F., Qian D., Fan X., Dickey E.C., Chen J.. Continuous Production of Aligned Carbon Nanotubes: a Step Closer to Commercial Realization:. *Chemical Physics Letters* **303**(5-6), 467-474 (1999).
- 26 Chopra N., Kichambare P. D., Andrews R., Hinds B. J.. Control of Multiwalled Carbon Nanotube Diameter by Selective Growth on the Exposed Edge of a Thin Film Multilayer Structure. *Nano Letters* **2**(10), 1177-1181 (2002).
- 27 Bhaviripudi S., Mile E., Steiner .s A., Zare A. T., Dresselhaus M. S., Belcher A. M., Kong J.. CVD Synthesis of Single-Walled Carbon Nanotubes from Gold Nanoparticle Catalysts. *Journal of American Chemical Society* **129**(6), 1516-1517 (2007).
- 28 Zhou W., Han Z., Wang J., Zhang Y., Jin Z., Sun X., Zhang Y., Yan C., Li Y.. Copper Catalyzing Growth of Single-Walled Carbon Nanotubes on Substrates. *Nano Letters* **6**(12), 2987-2990 (2006).
- 29 Huang S., Cai Q., Chen J., Qian Y., Zhang L.. Metal-Catalyst-Free Growth of Single-Walled Carbon Nanotubes on Substrates. *Journal of American Chemical Society* **131**(6), 2094–2095 (2009).
- 30 Liu B., Ren W, Gao L., Li S., Pei S., Liu C., Jiang C., Cheng H. M.. Metal-Catalyst-Free Growth of Single-Walled Carbon Nanotubes. *Journal of American Chemical Society* **131**(6), 2082–2083 (2009).
- 31 Sun Y. P., Fu F., Lin Y., Huang W.. Functionalized Carbon Nanotubes: Properties and Applications. *Accounts of Chemical Research* **35**, 1096-1104 (2002).
- 32 Jian Che J., Hamon M. A., Hu H., Chen Y. S., Rao A. M., Eklund P. C., Haddon R. C.. Solution Properties of Single-Walled carbon nanotubes. *Science* **282**, 95-98 (1998).
- 33 Bottini M., Cerignoli F., Dawson M. I., Magrini A., Rosato N., Mustelin T.. Full-Length Single-Walled Carbon Nanotubes Decorated with Streptavidin-Conjugated Quantum Dots as Multivalent Intracellular Fluorescent Nanoprobes. *Biomacromolecules* **7**, 2259-2263 (2006).
- 34 Smorodin T., Beierlein U. Kotthaus J. P.. Contacting gold nanoparticles with carbon nanotubes by self-assembly. *Nanotechnology* **16**, 1123–1125 (2005).
- 35 Li S., He P., Dong J., Guo Z, Dai L.. DNA-Directed Self-Assembling of Carbon Nanotubes, *Journal of American Chemical Society* **127**(1), 14-15 (2005).
- 36 Ou Y. Y., Huang M. H.. High-Density Assembly of Gold Nanoparticles on Multiwalled Carbon Nanotubes Using 1-Pyrenemethylamine as Interlinker. *Journal of Physical Chemistry B* **110**, 2031-2036 (2006).

- 37 Jiang K., Eitan A., Schadler L. S., Ajayan P. M., Siegel R. W.. Selective Attachment of Gold Nanoparticles to Nitrogen-Doped Carbon Nanotubes. *Nano Letters* **3**(3), 275-277 (2003).
- 38 Choi H. C., Shim M., Bangsaruntip S., Dai H.. Spontaneous Reduction of Metal Ions on the Sidewalls of Carbon Nanotubes. *Journal of American Chemical Society* **124**, 9058-9059 (2002).
- 39 Qu L, Dai L. Substrate-Enhanced Electroless Deposition of Metal Nanoparticles on Carbon Nanotubes. *Journal of American Chemical Society* **127**, 10806-10807 (2005).
- 40 Lee Y., Song H. J., Shin H. S., Shin H. J., Choi H. C.. Spontaneous Formation of Transition-Metal Nanoparticles on Single-Walled Carbon Nanotubes Anchored with Conjugated Molecules. *Small* **1**(10), 975-979 (2005).
- 41 Zhang R., Wang X. One Step Synthesis of Multiwalled Carbon Nanotube/Gold Nanocomposites for Enhancing Electrochemical Response. *Chemistry of Materials* **19**, 976-978 (2007).
- 42 Lin Y., Baggett D. W., Kim J. W., Siochi E. J., Connell J. W.. Instantaneous Formation of Metal and Metal Oxide Nanoparticles on Carbon Nanotubes and Graphene via Solvent-Free Microwave Heating. *ACS Applied Materials and Interface* **3**, 1652–1664 (2011).
- 43 Lin Y., Watson K. A., Fallbach M. J., Ghose S., Smith, J. G., Delozier D. M., Cao W., Crooks R. E., Connell J. W.. Rapid, Solventless, Bulk Preparation of Metal Nanoparticle-Decorated Carbon Nanotubes. *ACS Nano* **3**(4), 871-884 (2009).
- 44 Lin Y., Watson K. A., Ghose S., Smith J. G., Williams T. V., Crooks R. E., Cao W., Connell J. W.. Direct Mechanochemical Formation of Metal Nanoparticles on Carbon Nanotubes, *Journal of Physical Chemistry C* **33**(113), 14858-14862 (2009).
- 45 Zhang R., Wang Q., Zhang L., Yang S., Yang Z., Ding B.. The growth of uncoated gold nanoparticles on multiwalled carbon nanotubes. *Colloids and Surfaces A: Physicochemical and Engineering Aspects* **312**, 136-142 (2008).
- 46 Wang Q., Geng B., Tao B.. A facile room temperature chemical route to Pt nanocube/carbon nanotube heterostructures with enhanced electrocatalysis. *Journal of Power Source* **196**(1), 191-195 (2011).
- 47 Chergui S. M., Ledebt A., Mammeri F., Herbst F., Carbonnier B., Romdhane H. B., Delamar M., Chehimi M. M.. Hairy Carbon Nanotube@Nano-Pd Heterostructures: Design, Characterization, and Application in Suzuki C–C Coupling Reaction. *Langmuir* **26**(20), 16115-16121 (2010).

- 48 Schexnaider P., Schmidt G., Nanocomposite polymer hydrogels, *Colloid Polymer Science* **287**, 1-11 (2009).
- 49 Hennink W. E., Nostrum C. F.. Novel crosslinking methods to design hydrogels, *Advanced Drug Delivery Reviews* **54**, 13-36 (2005).
- 50 Yuan Q., Venkatasubramanian R., Hein S., Misra R. D. K.. A stimulus-responsive magnetic nanoparticle drug carrier: Magnetite encapsulated by chitosan-grafted-copolymer. *Acta Biomaterialia* **4**, 1024–1037 (2008).
- 51 Zhao X., Ding X., Deng Z., Zheng Z., Peng Y., Long X.. Thermoswitchable Electronic Properties of a Gold Nanoparticle/Hydrogel Composite. *Macromolecules Rapid Communication* **26**, 1784–1787 (2005).
- 52 Kim D. J., Kang S. M., Kong B., Kim W. J., Paik H. J., Choi H., Choi I. S.. Formation of Thermoresponsive Gold Nanoparticle/PNIPAAmHybrids by Surface-Initiated, Atom Transfer Radical Polymerization in Aqueous Media. *Macromolecular Chemistry and Physics* **206**, 1941–1946 (2005).
- 53 Wang C., Flynn N. T., Langer R.. Controlled Structure and Properties of Thermoresponsive Nanoparticles-Hydrogel Composites. *Advanced Materials* **16**(13), 1074-1079 (2004).
- 54 Yavuz M. S., Cheng Y., Chen J., Cobley C. M., Zhang Q., Rycenga M., Xie J., Kim C., Song K. H., Schwartz A. G., Wang L. V., Xia Y. Gold nanocages covered by smart polymers for controlled release with near-infrared light. *Nature Materials* **8**, 935 - 939 (2009).
- 55 Satarkar N. S., Hilt Z. J.. Magnetic hydrogel nanocomposites for remote controlled pulsatile drug release. *Journal of Controlled Release* **130**, 246-251 (2008).
- 56 Satarkar N. S., Zhang W., Eitel R. E., Hilt J. Z.. Magnetic hydrogel nanocomposites as remote controlled microfluidic valves. *Lab on a Chip* **9**, 1773–1779 (2009).
- 57 Gupta M. K., Chang S., Singamaneni S., Drummy L. F., Gunawidjaja R., Naik R. R., Tsukruk V. V.. pH-Triggered SERS via Modulated Plasmonic Coupling in Individual Bimetallic Nanocobs. *Small* **7**(9), 1192-1198 (2011).
- 58 Shi W, Crews K, Chopra N, Synthesis and Characterization of Carbon Nanotube-Nickel/Nickel Oxide Core/shell Nanoparticle Heterostructures Incorporated in Polyvinyl Alcohol Hydrogel. *Material Research. Society Symposium Proceeding* **1272**, PP06-20 (2010).
- 59 Hassan C. M., Peppas N. A.. Cellular PVA Hydrogels Produced by Freez/thawing. *Journal of Applied Polymer Science* **76**(14), 2075-2079 (2000).

- 60 Ingle J. D. J., Crouch S. R.. Spectrochemical Analysis, Prentice Hall, New Jersey (1988)
- 61 Kwok RWM. XPS Peak Fitting Program for WIN95/98 XPSPEAK Version 4.1, Department of Chemistry, The Chinese University of Hong Kong.
- 62 Carvell J., Ayieta E., Johnson M., Cheng R., Characterization of iron nanoparticles synthesized by high pressure sputtering. *Material Letters* **63**(8), 715-717 (2009).
- 63 Peng F., Luo T., Qiu L., Yuan Y.. Influence of the crystallinity of the iron catalysts on the formation of carbon nanotubes. *Material Research Bulletin* **46**(6), 884-887 (2011).
- 64 Lucas A. A., Bruyninckx V., Lambin P., Bernaerts D., Amelinckx S., Landuyt J. V., Tendeloo G. V.. Electron diffraction by carbon nanotubes. *Scanning Microscopy* **12**(3), 415-436 (1998).
- 65 Zhang X. F., Zhang X. B., Tendeloo G. V., Amelinckx G. V., Beeck M. O., Landuyt J. V.. Carbon nano-tubes; their formation process and observation by electron microscopy. *Journal of Crystal Growth* **130** (3-4), 368-382 (1993).
- 66 Souza Filho A.G., Jorio A., Samsonidze G.G., Dresselhaus G., Saito R., Dresselhaus M. S.. Raman spectroscopy for probing chemically/physically induced phenomena in carbon nanotubes. *Nanotechnology* **14**, 1130-1139 (2003).
- 67 Park J., Kang E., Son S. U., Park H. M., Lee M. K., Kim J., Kim K. W., Noh H. J., Park J. H., Bae C. J., Park J. G., Hyeon T.. Monodisperse Nanoparticles of Ni and NiO: Synthesis, Characterization, Self-Assembled Superlattices, and Catalytic Applications in the Suzuki Coupling Reaction. *Advanced Material* **17**(4), 429-434 (2005).
- 68 Lee I. S., Lee N., Park J., Kim B. H., Yi Y.W., Kim T., Kim T. K., Lee I. H., Paik S. R., Hyeon T., Ni/NiO Core/Shell Nanoparticles for Selective Binding and Magnetic Separation of Histidine-Tagged Proteins. *Journal of American Chemical Society* **128**(33), 10658-10659 (2006).
- 69 Zhang Z., Gao M.. Uniformly Distributed Nickel Nanoparticles Created by Heating the Carbon Nanotube, *Journal of Material Research* **18**(3), 604-608 (2003).
- 70 Cao A., Xu C., Liang J., Wu D., Wei B.. X-ray Diffraction Characterization on the Alignment Degree of Carbon Nanotubes. *Chemical Physics Letter* **344**(1-2), 13-17 (2001).
- 71 Dietz R. E., Parisot G.I., Meixner A.E., Infrared absorption and Raman scattering by two-magnon processes in NiO. *Physics Review B* **4**, 2302-2309 (1971).

- 72 Wang W., Liu Y., Xu C., Zheng C., Wang G.. Synthesis of NiO nanorods by a novel simple precursor thermal decomposition approach. *Chemical Physics Letters* **362**, 119–122 (2002).
- 73 Tzitzios V., Georgakilas V., Oikonomou E., Karakassides M., Petridis D.. Synthesis and characterization of carbon nanotube/metal nanoparticle composites well dispersed in organic media. *Carbon* **44**, 848-853 (2006).
- 74 Wagner CD. Handbook of XPS. Physical Electronics, Inc. 1979.
- 75 Chopra N., Claypoole L., Bachas L. G.. Morphological control of Ni/NiO core/shell nanoparticles and production of hollow NiO nanostructures. *Journal of Nanoparticle Research* **12**(8), 2883-2893 (2010).
- 76 Bratlie K. M., Lee H., Komvopoulos K., Yang P., Somorjai G. A.. Platinum nanoparticle shape effects on benzene hydrogenation selectivity. *Nano Letter* **7**(10), 3097–3101 (2007).
- 77 C. N. R. Rao, A. Muller, A. K. Cheetham. Nanomaterials Chemistry. Wiley-VCH. 2007.
- 78 Feng Huang, Hengzhong Zhang, Jillian F. Banfield. Two-Stage Crystal-Growth Kinetics Observed during Hydrothermal Coarsening of Nanocrystalline ZnS. *Nano Letters* **3**(3), 373-378 (2003).
- 79 Despres J. F., Daguerre E., Lafdi K.. Flexibility of graphene layers in carbon nanotubes. *Carbon* **33**(1), 87-89 (1995).
- 80 Kwok Y. S., Zhang X. X., Qin B., Fung K. K.. Epitaxial NiO hillocks on truncated octahedral nanoparticles of passivated Ni. *Journal of Applied Physics* **89**(5), 3061-3063 (2001).
- 81 Li J., Ni Y., Liao K., Hong J.. Hydrothermal synthesis of Ni₁₂P₅ hollow microspheres, characterization and photocatalytic degradation property. *Journal of Colloid and Interface Science* **332**(1), 231-236 (2009).
- 82 Chiang R. K., Chiang R. T.. Formation of Hollow Ni₂P Nanoparticles Based on the Nanoscale Kirkendall Effect. *Inorganic Chemistry* **46**(2), 369-371 (2007).
- 83 Bao Y., An W., Turner C. H., Krishnan K. M.. The critical role of surfactants in the growth of cobalt nanoparticles. *Langmuir* **26**(1), 478-483 (2010).
- 84 Qi M., Gu Y., Sakata N., Kim D., Shirouzu Y., Yamamoto C., Hiura A., Sumi S., Inoue K.. PVA Hydrogel Sheet Macro-encapsulation for the Bioartificial Pancreas, *Biomaterials* **25**(27), 5885-5892 (2004).

- 85 Hoffman A. S.. Hydrogels for Biomedical Applications. *Advanced Drug Delivery Review* **54**(1) 3-12 (2002).
- 86 Kozlovskaya V., Kharlampieva E., Khanal B. P., Manna P., Zubarev E. R., Tsukruk V. V.. Ultrathin Layer-by-Layer Hydrogels with Incorporated Gold Nanorods as pH-Sensitive Optical Materials, *Chemistry of Materials* **20**(24), 7474-7485 (2008).
- 87 Lepak L. A., Richards T., Guillen N., Caggana M., Turner J. N., Spencer M. G.. Preparation and Characterization of Porous Collagen Membranes on Silicon, *Materials Research Society Symposium Proceeding* **752**, AA8.17 (2003).
- 88 Yang F., Moss L.G., Phillips G.N.. The Molecular Structure of Green Fluorescent Protein. *Nature Biotechnology* **14**(10), 1246-1251 (1996).
- 89 Suslick K. S., Sonochemistry, *Science* **247**, 1439-1445 (1990).
- 90 Majumdar D., Saha S. K.. Poly(3-hexylthiophene) nanotubes with superior electronic and optical properties. *Chemical Physics Letters* **489**(4-6), 219-224 (2010).
- 91 Shi W., Chopra N.. Surfactant-free synthesis of novel copper oxide (CuO) nanowire–cobalt oxide (Co₃O₄) nanoparticle heterostructures and their morphological control. *Journal of Nanoparticle Research* **13**(2), 851-856 (2011).
- 92 Hota G., Idage S. B., Khilar K. C.. Characterization of nano-sized CdS-Ag₂S core-shell nanoparticle using XPS technique. *Colloid Surface A* **293**(1-3), 5-12 (2007).
- 93 Datsyuk V., Kalyva M., Papagelis K., Parthenios J., Tasis D., Siokou A., Kallitsis I., Galiotis C.. Chemical oxidation of multiwalled carbon nanotubes. *Carbon* **46**(6), 833-840 (2008).
- 94 Himani S., Shailesh N. S., Sukhvir S., Ram K., Gurmeet S., Shivaprasad S. M.. Surface sensitive probe of the morphological and structural aspects of CdSe core–shell nanoparticles. *Applied Surface Science* **253**(12), 5325–5333 (2007).
- 95 Pengxiang Song, Dongsheng Wen, Z. X. Guo, Theodosios Korakianitis. Oxidation investigation of nickel nanoparticles. *Physical Chemistry Chemical Physics*. **10**, 5057-5065 (2008).
- 96 Lee Y. T., Kim N. S., Park G., Han J. B., Chop Y. S., Ryu H.. Temperature-dependent growth of carbon nanotubes by pyrolysis of ferrocene and acetylene in the range between 700 and 1000 °C. *Chemical Physics Letter* **372**(5-6), 853-859 (2003).
- 97 Spudat C., Muller M., Houben L., Maultzsch J., Goss K., Thomsen C.. Observation of Breathing-like Modes in an Individual Multiwalled Carbon Nanotube. *Nano Letters* **10**(11), 4470–4474 (2010).

- 98 Shim S. H., Duffy T.. Raman spectroscopy of Fe₂O₃ to 62 GPa. *American Mineralogist* **87**(2-3), 318–326 (2001).

APPENDIX

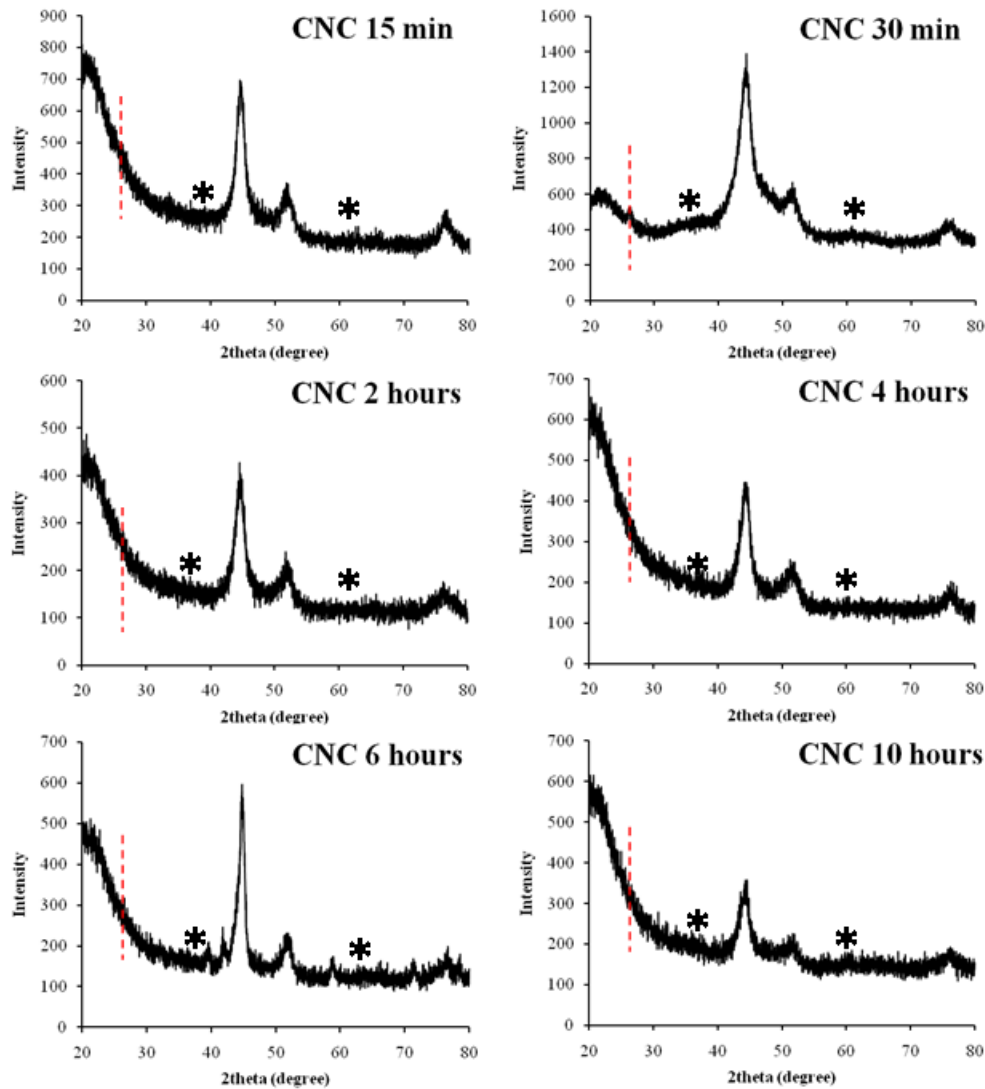
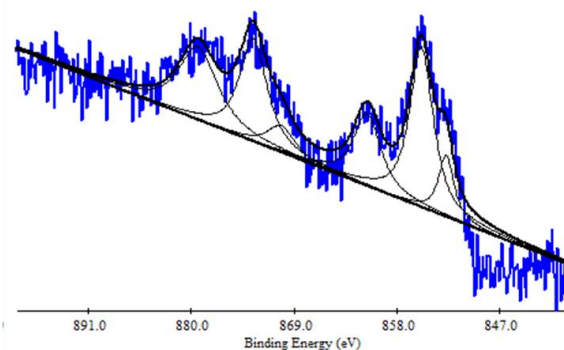


Figure A1 Detailed XRD peaks for CNC heterostructures as a function of reaction duration (15 min – 10 hrs). Red dotted line indicates location of CNTs peak and (*) represents peaks for NiO. Note: The duration indicated represents the nanoparticle growth reaction duration.

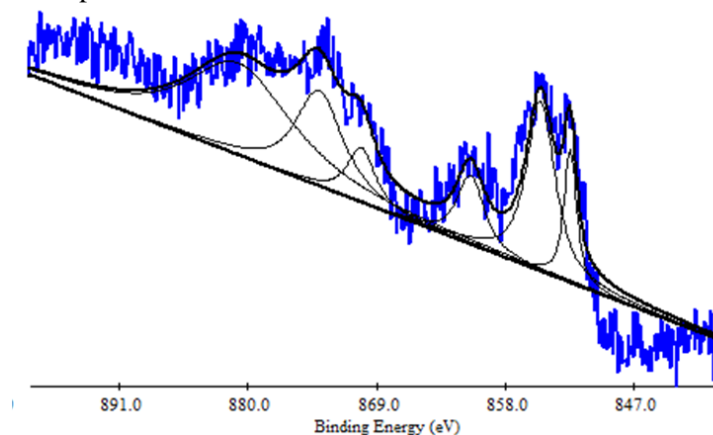
Ni 2p scan from as-prepared CNC heterostructures

A



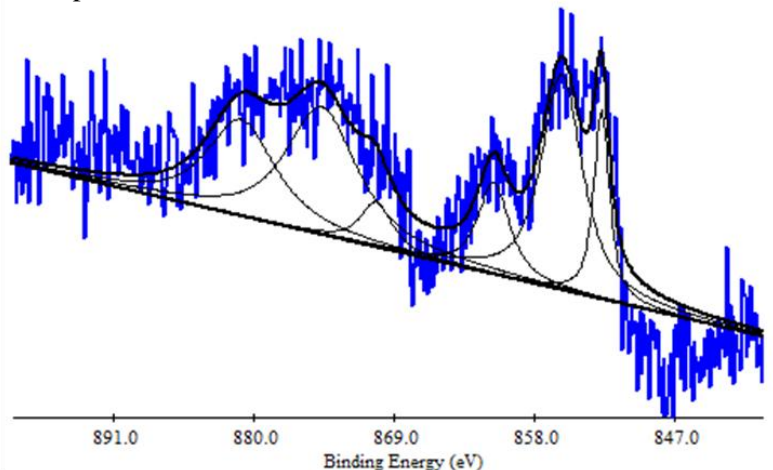
Peak location	Peak area	Assignment
852.7	1898.18	Ni ⁰ 2p _{3/2}
855.38	7402.9	Ni ²⁺ 2p _{3/2}
861.17	3882.64	Satellite
870.37	1438.02	Ni ⁰ 2p _{1/2}
873.35	5551.792	Ni ²⁺ 2p _{1/2}
879.25	568.26	Satellite

Ni 2p scan from CNC heterostructures annealed at 125 °C



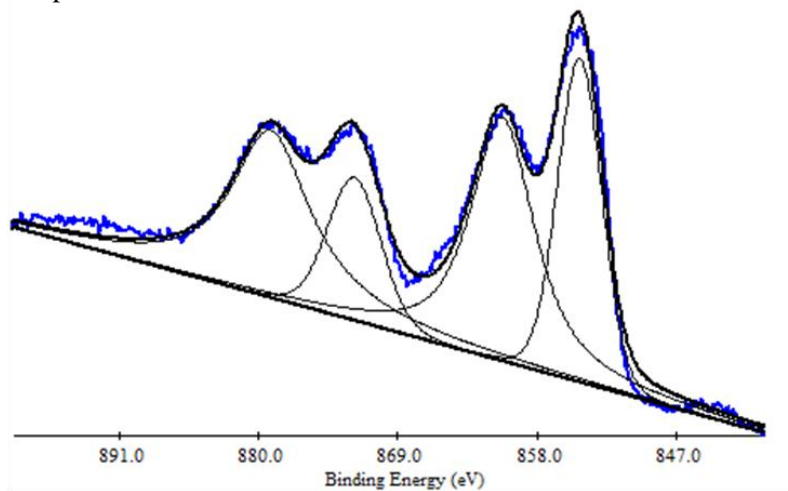
Peak location	Peak area	Assignment
852.45	2400.7	Ni ⁰ 2p _{3/2}
854.98	7466.75	Ni ²⁺ 2p _{3/2}
860.97	2619.83	Satellite
870.3	2175.8	Ni ⁰ 2p _{1/2}
873.56	5766.98	Ni ²⁺ 2p _{1/2}
879.87	12471.65	Satellite

Ni 2p scan from CNC heterostructures annealed at 200 °C



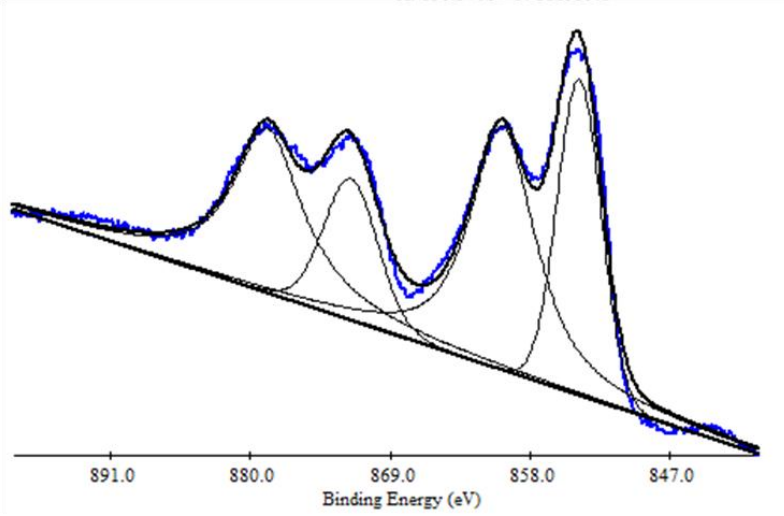
Peak location	Peak area	Assignment
852.678	2229	Ni ⁰ 2p _{3/2}
855.794	6518.694	Ni ²⁺ 2p _{3/2}
861.150	2153.536	Satellite
870.366	1080.604	Ni ⁰ 2p _{1/2}
874.668	6749.650	Ni ²⁺ 2p _{1/2}
880.995	4918.598	Satellite

Ni 2p scan from CNC heterostructures annealed at 400 °C



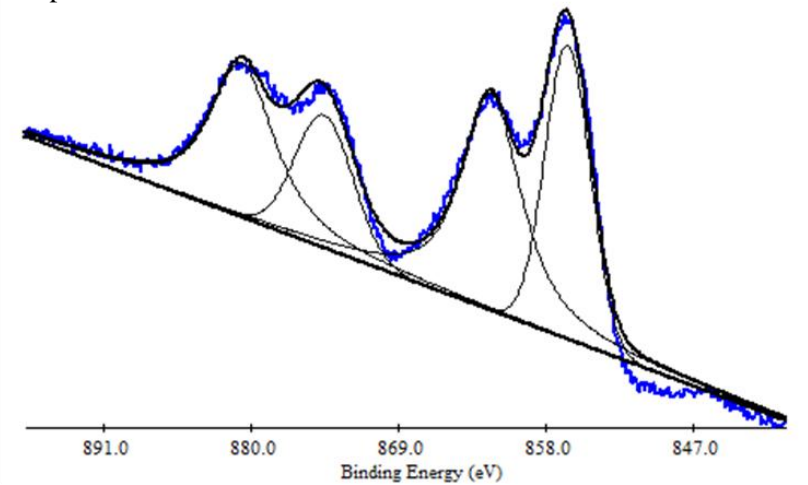
Peak location	Peak area	Assignment
854.624	106204.7	Ni ²⁺ 2p _{3/2}
860.713	152899.2	Satellite
872.411	57754.97	Ni ²⁺ 2p _{1/2}
879.010	141979.3	Satellite

Ni 2p scan from CNC heterostructures annealed at 600 °C



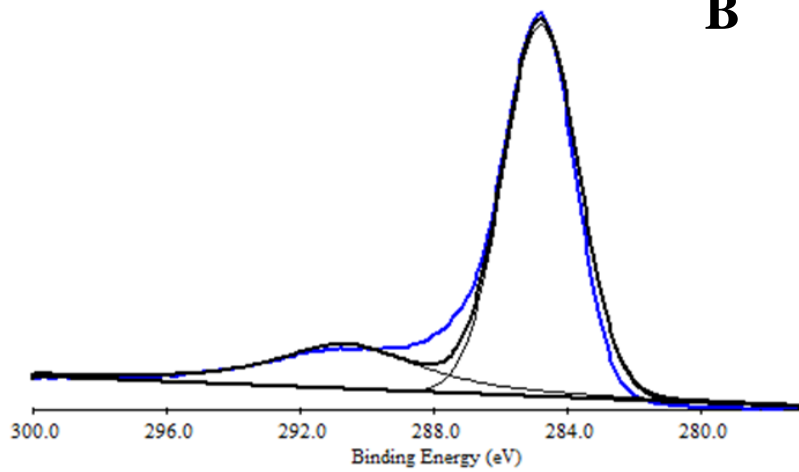
Peak location	Peak area	Assignment
854.144	148436.2	Ni ²⁺ 2p _{3/2}
860.172	239066.5	Satellite
872.106	86837.44	Ni ²⁺ 2p _{1/2}
878.654	185790.7	Satellite

Ni 2p scan from CNC heterostructures annealed at 750 °C

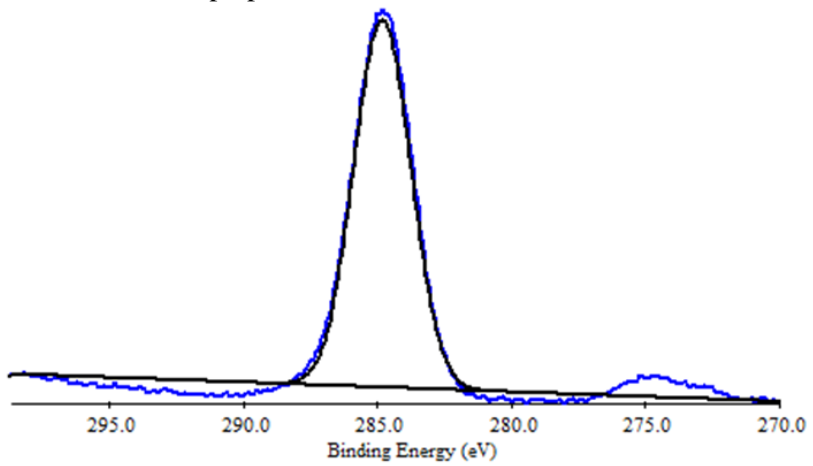


Peak location	Peak area	Assignment
856.358	79777.83	Ni ²⁺ 2p _{3/2} (could be 3+ too)
862.066	107139.6	Satellite
874.578	46010.92	Ni ²⁺ 2p _{1/2}
880.711	82724.91	Satellite

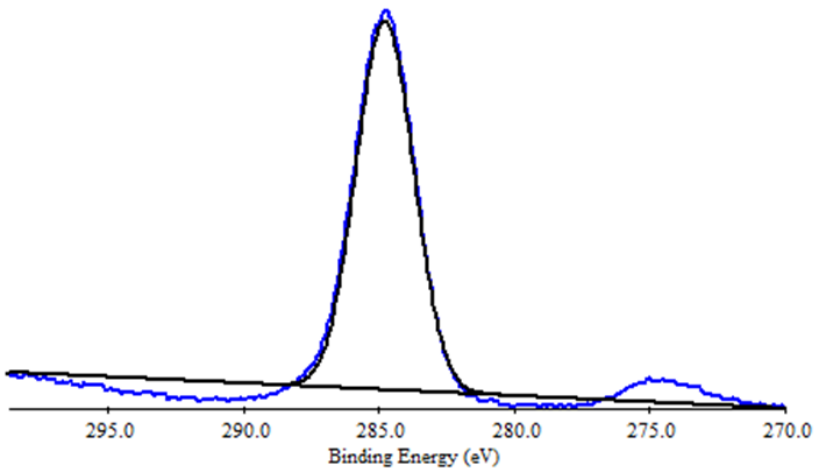
C 1s scan for as-produced CNT



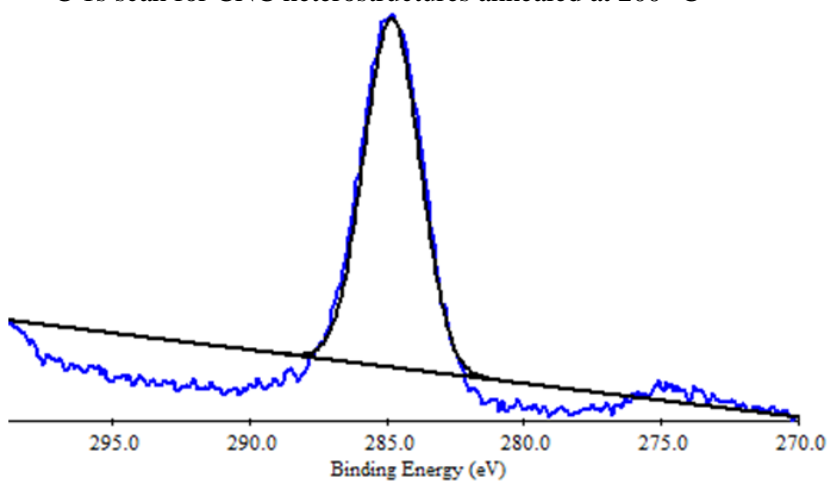
C 1s scan for as-prepared CNC heterostructures



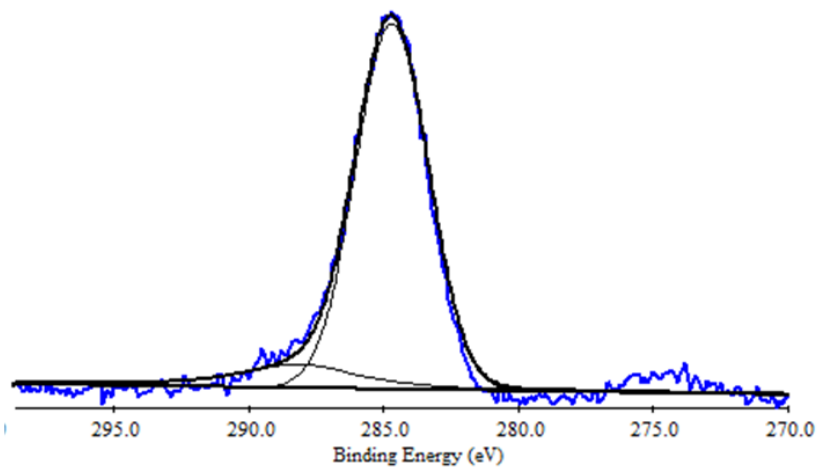
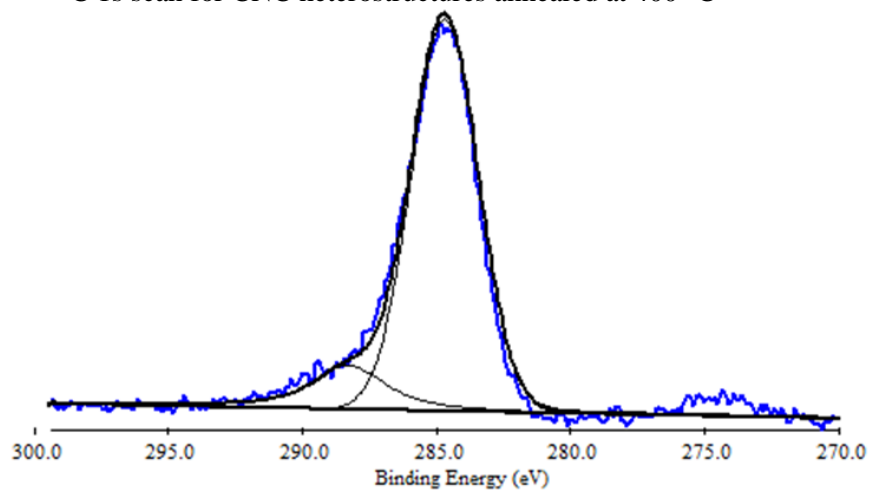
C 1s scan for CNC heterostructures annealed at 125 °C



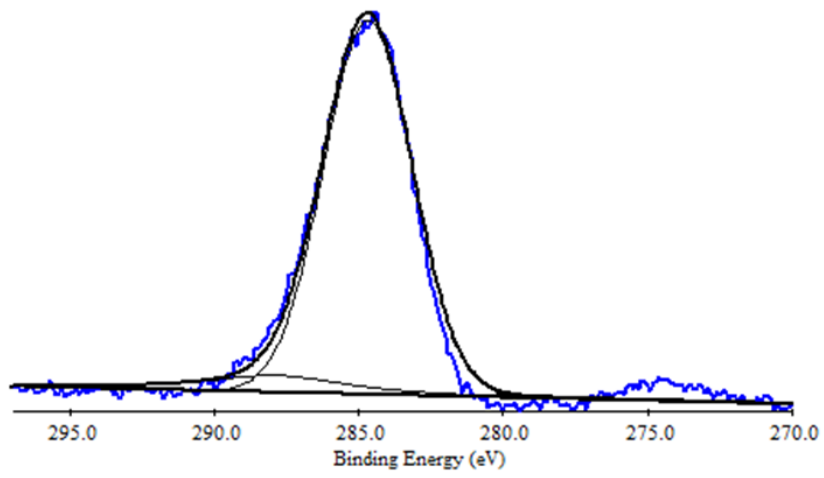
C 1s scan for CNC heterostructures annealed at 200 °C



C 1s scan for CNC heterostructures annealed at 400 °C

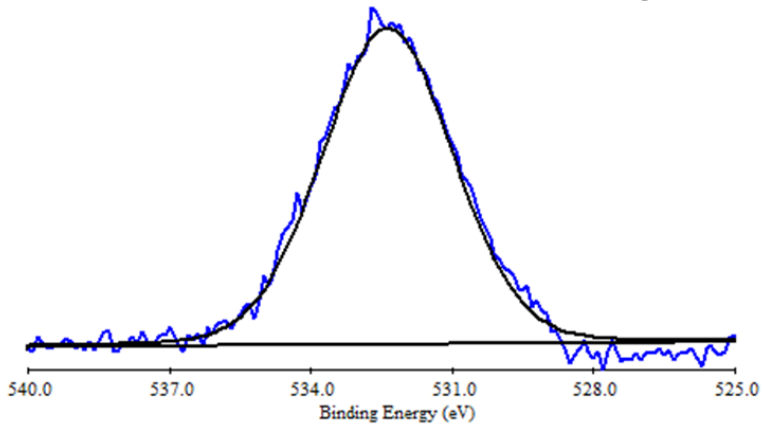


C 1s scan for CNC heterostructures annealed at 750 °C

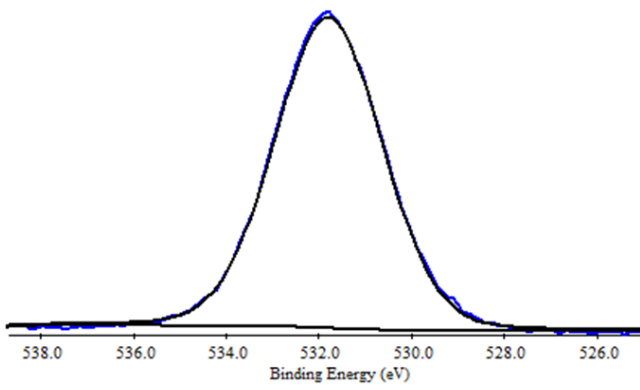


O 1s scan for as-produced CNTs

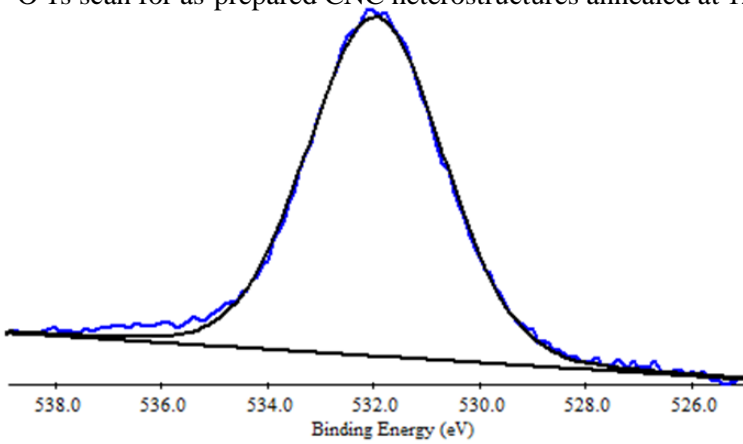
C



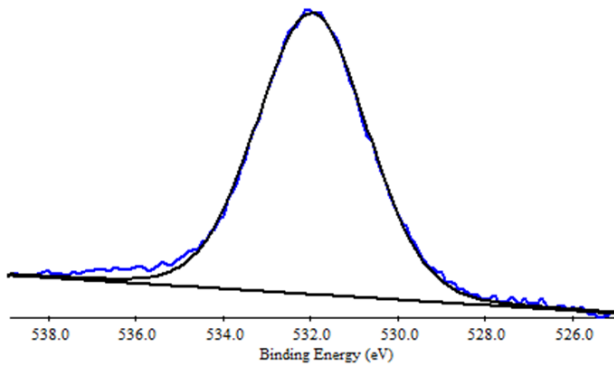
O 1s scan for as-prepared CNC heterostructures



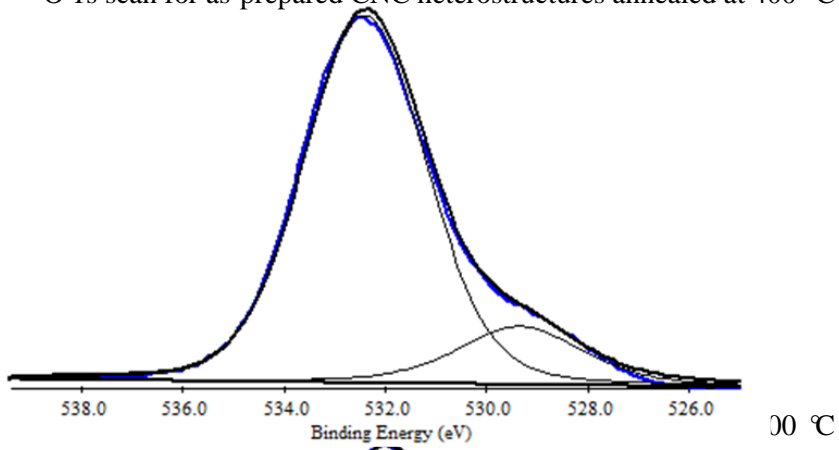
O 1s scan for as-prepared CNC heterostructures annealed at 125 °C



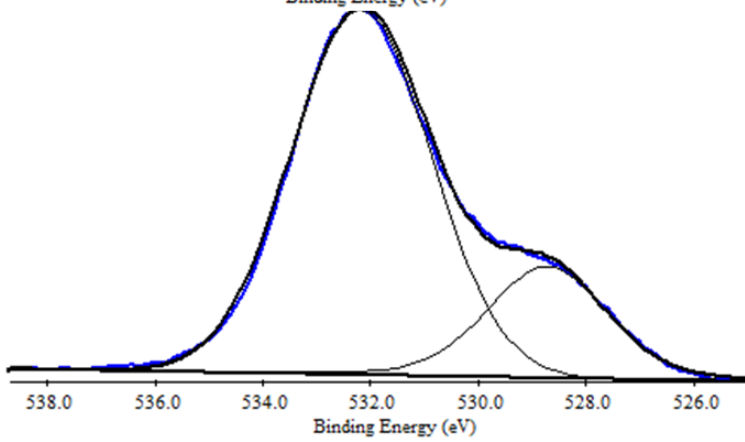
O 1s scan for as-prepared CNC heterostructures annealed at 200 °C



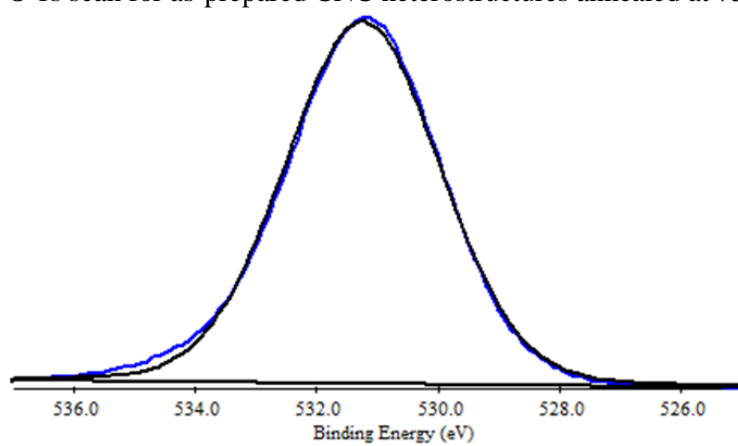
O 1s scan for as-prepared CNC heterostructures annealed at 400 °C



00 °C

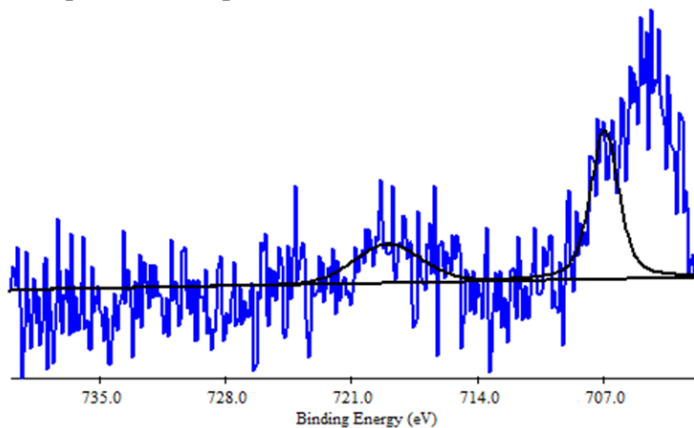


O 1s scan for as-prepared CNC heterostructures annealed at 750 °C



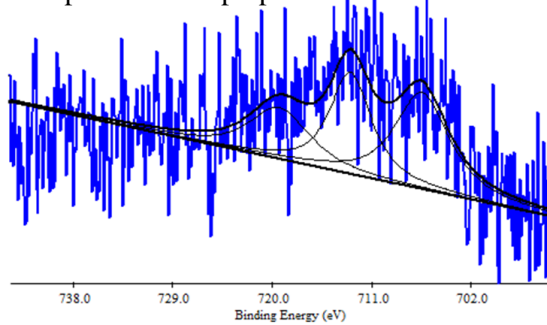
Fe 2p scan for as-produced CNTs

D



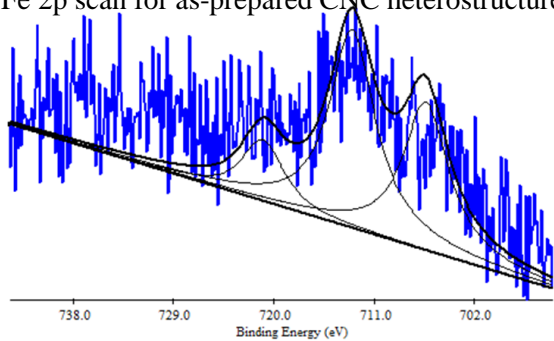
Peak location	Peak area	Assignment
706.91	2009	Fe 2p _{3/2}
719.00	1019.44	Fe 2p _{1/2}

Fe 2p scan for as-prepared CNC heterostructures



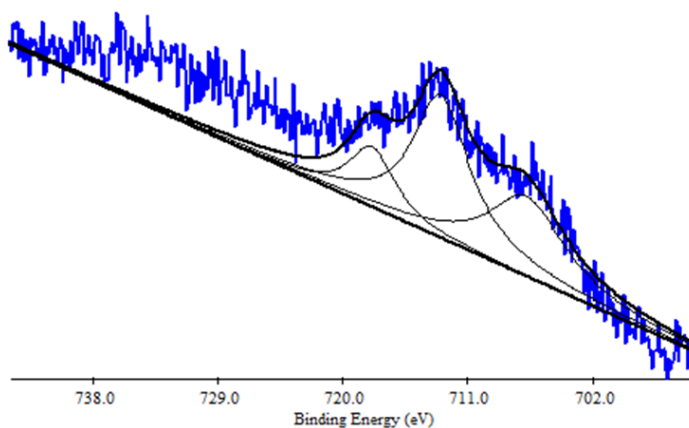
Peak location	Peak area	Assignment
706.42	4037.10	Fe 2p _{3/2} / Ni L ₃ M ₂₃ M ₄₅ (³ P)
712.8	3219.33	Ni L ₃ M ₂₃ M ₄₅ (¹ P)
719.34	2310	Fe 2p _{1/2}

Fe 2p scan for as-prepared CNC heterostructures annealed at 125 °C



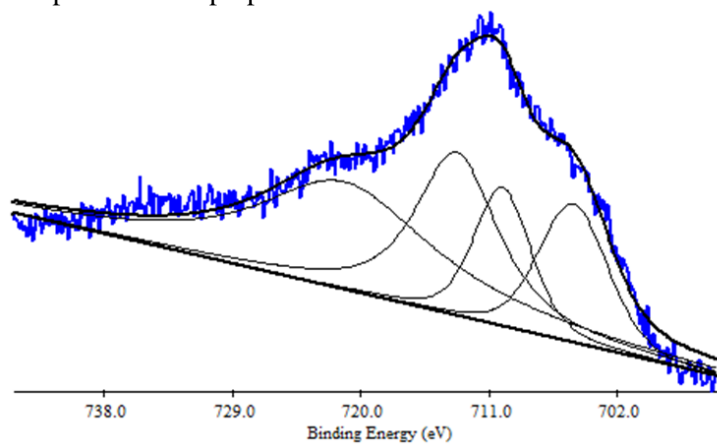
Peak location	Peak area	Assignment
706.34	7037.47	Fe 2p _{3/2} / Ni L ₃ M ₂₃ M ₄₅ (³ P)
712.95	9423.47	Ni L ₃ M ₂₃ M ₄₅ (¹ P)
720.95	2454.2	Fe 2p _{1/2}

Fe 2p scan for as-prepared CNC heterostructures annealed at 200 °C



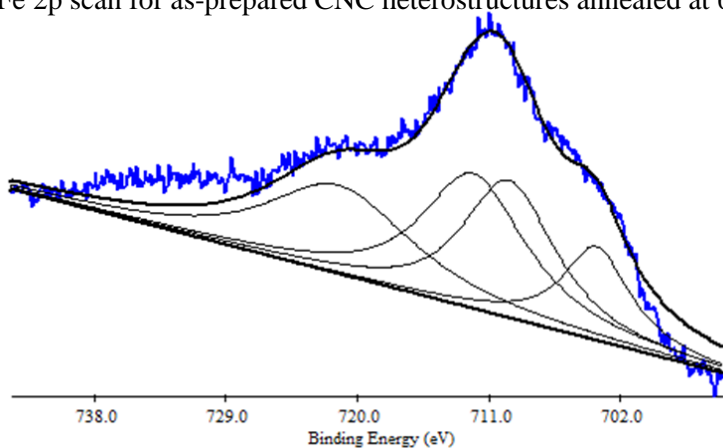
Peak location	Peak area	Assignment
706.75	13528.1	Fe 2p _{3/2} / Ni L ₃ M ₂₃ M ₄₅ (³ P)
712.94	18346.8	Ni L ₃ M ₂₃ M ₄₅ (¹ P)
720.5	8769.4	Fe 2p _{1/2}

Fe 2p scan for as-prepared CNC heterostructures annealed at 400 °C



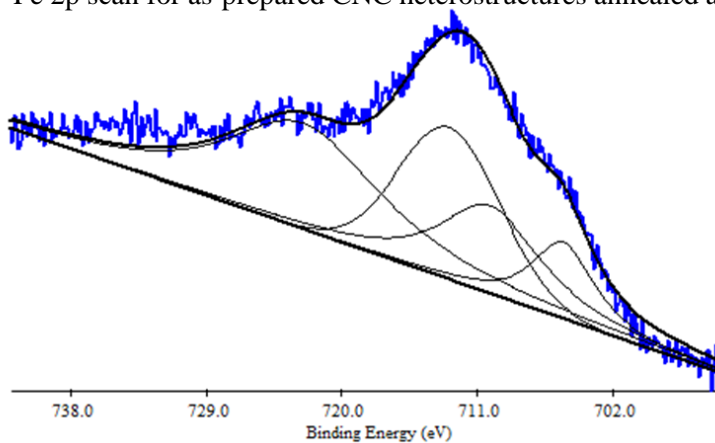
Peak location	Peak area	Assignment
705.07	26137	Fe 2p _{3/2} / Ni L ₃ M ₂₃ M ₄₅ (³ P)
710.05	22586.5	Fe ^{x+}
713.28	45300	Ni L ₃ M ₂₃ M ₄₅ (¹ P)
721.22	68261	Fe 2p _{1/2}

Fe 2p scan for as-prepared CNC heterostructures annealed at 600 °C



Peak location	Peak area	Assignment
703.63	38502.1	Fe 2p _{3/2} / Ni L ₃ M ₂₃ M ₄₅ (³ P)
709.62	70433.1	Fe ^{x+}
712.06	80931.2	Ni L ₃ M ₂₃ M ₄₅ (¹ P)
721.3	71177.4	Fe 2p _{1/2}

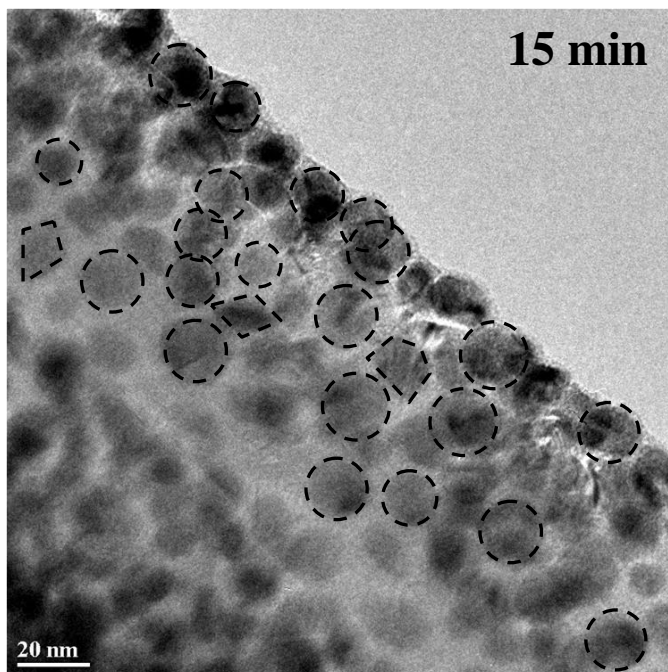
Fe 2p scan for as-prepared CNC heterostructures annealed at 750 °C



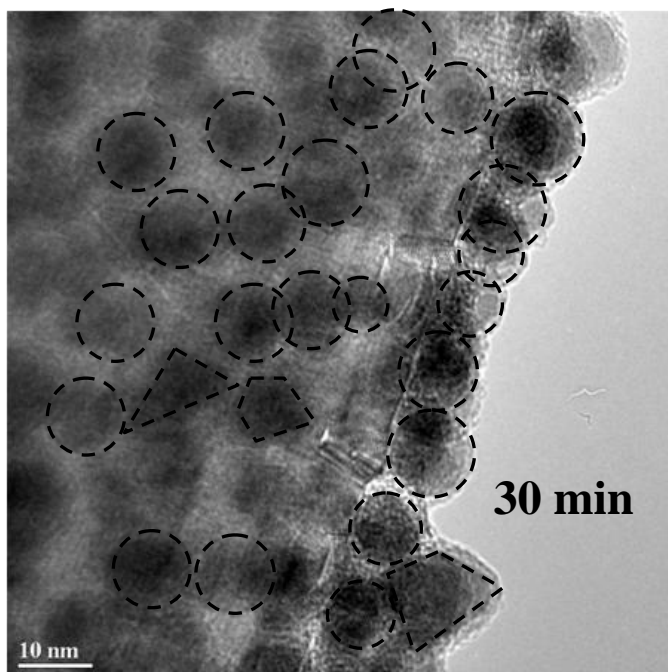
Peak location	Peak area	Assignment
705.27	16045.3	Fe 2p _{3/2} / Ni L ₃ M ₂₃ M ₄₅ (³ P)
710.17	29491.3	Fe ^{x+}
712.85	37022.2	Ni L ₃ M ₂₃ M ₄₅ (¹ P)
722.62	54814.2	Fe 2p _{1/2}

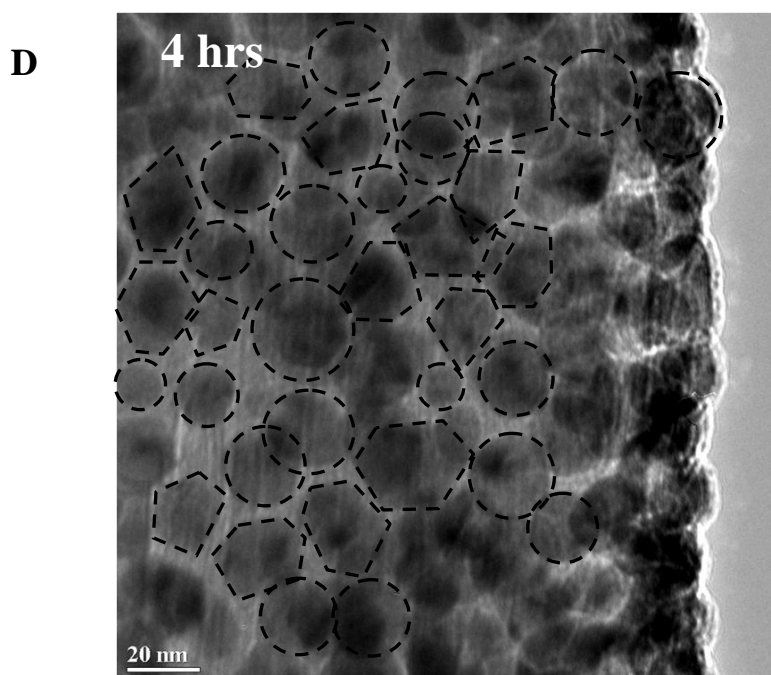
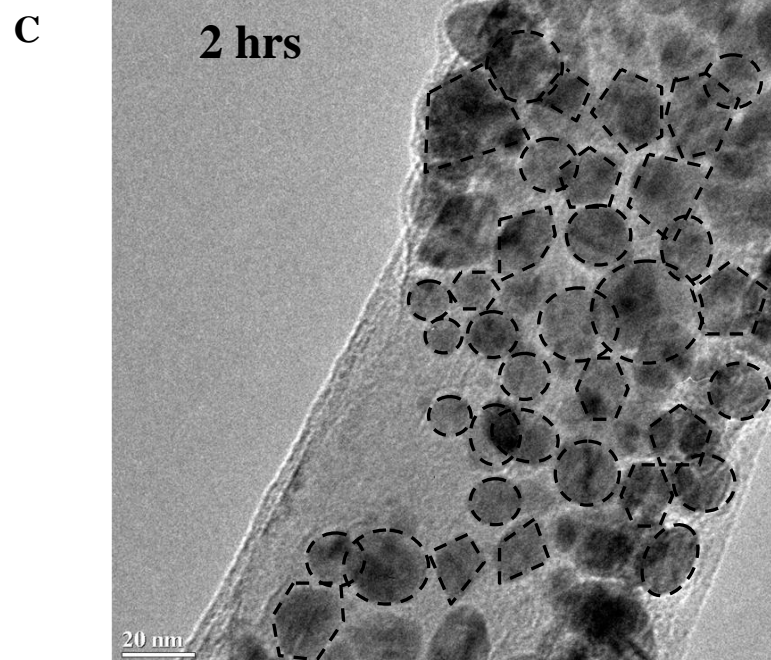
Figure A2. Detailed deconvoluted XPS peaks for A) nickel, B) carbon, C) oxygen, and D) iron

A

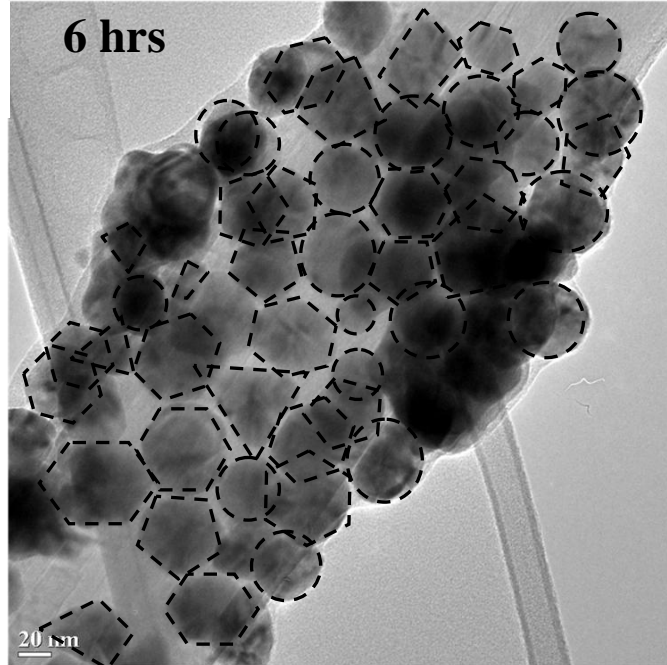


B

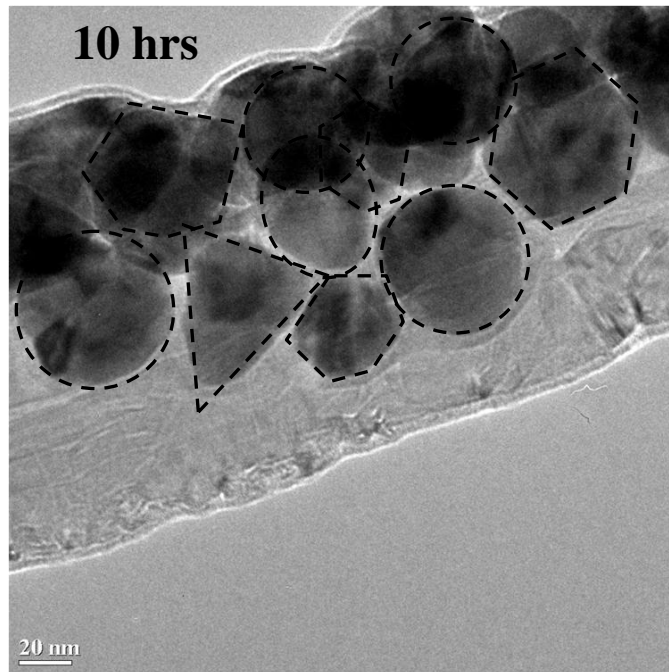




E



F



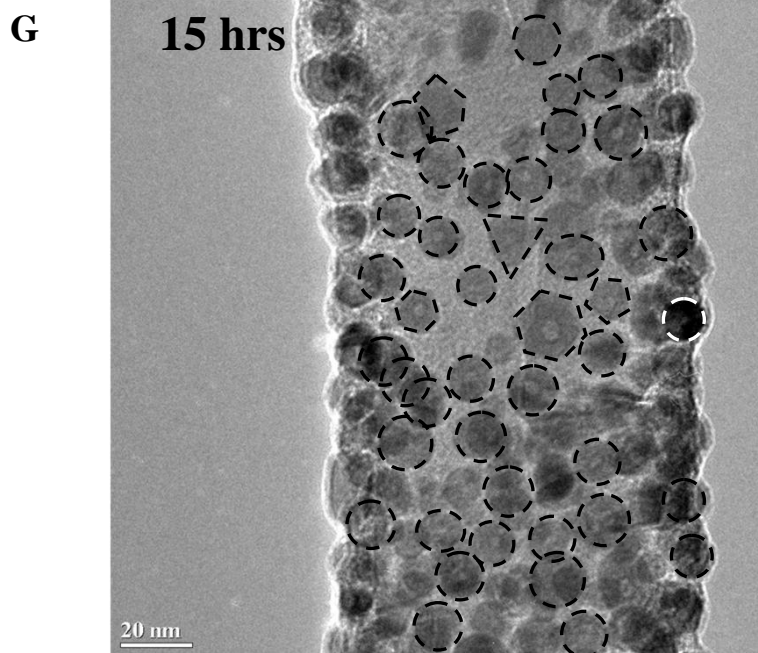


Figure A3 High resolution TEM images of CNC heterostructures grown for different durations. (A) 15 min, (B) 30 min, (C) 2 hrs, (D) 4 hrs, (E) 6 hrs, (F) 10 hrs, and (G) CNT-nickel phosphide nanoparticle heterostructures formed at 15 hrs growth duration. Note: Different shapes are showed with dotted outlines.